PONTIFÍCIA UNIVERSIDADE CATÓLICA
DO RIO DE JANEIRO

Alessandro Cirone

Theory and implementation of constitutive models for geomaterials

Tese de Doutorado

Thesis presented to the Programa de Pós–graduação em Engenharia Civil e Ambiental of PUC-Rio in partial fulfillment of the requirements for the degree of Doutor em Ciências - Engenharia Civil.

Advisor : Prof. Eurípedes do Amaral Vargas Jr.
Co-advisor: Prof. Tácio Mauro Pereira de Campos

Rio de Janeiro
July 2020

Pontifícia Universidade Católica
do Rio de Janeiro

Alessandro Cirone

Theory and implementation of constitutive models for geomaterials

Thesis presented to the Programa de Pós–graduação em Engenharia Civil e Ambiental of PUC-Rio in partial fulfillment of the requirements for the degree of Doutor em Ciências - Engenharia Civil. Approved by the Examination Comittee:

Prof. Eurípedes do Amaral Vargas Jr.
Advisor
Departamento de Engenharia Civil e Ambiental – PUC-Rio

Prof. Tácio Mauro Pereira de Campos
Co-advisor
Departamento de Engenharia Civil e Ambiental – PUC-Rio

Prof. Deane de Mesquita Rohel
Departamento de Engenharia Civil e Ambiental – PUC-Rio

Prof. Marcio de Souza Soares de Almeida
Universidade Federal do Rio de Janeiro – UFRJ

Prof. Antonio Gens
Universitat Politècnica de Catalunya – UPC

Prof. Marcos Massao Futai
Universidade de São Paulo – USP

Rio de Janeiro, July the 10th, 2020

Alessandro Cirone

Possui graduação em Engenharia Civil (2012) e mestrado em Geotecnia (2016) pela Politécnica de Milão (Milão, Itália). Entre 2014 e 2016 fez intercâmbio de Dupla Diplomação em Engenharia Civil na PUC-Rio. Tem experiência na área de melhoramento de solos, grouting, análise numérica, investigação geotécnica, geofísica e modelos constitutivos.

Bibliographic data

Cirone, Alessandro

Theory and implementation of constitutive models for geomaterials / Alessandro Cirone; advisor: Eurípedes do Amaral Vargas Jr.; co-advisor: Tácio Mauro Pereira de Campos. – Rio de janeiro: PUC-Rio, Departamento de Engenharia Civil e Ambiental, 2020.

v., 164 f: il. color. ; 30 cm

Tese (doutorado) - Pontifícia Universidade Católica do Rio de Janeiro, Departamento de Engenharia Civil e Ambiental.

Inclui bibliografia

1. Engenharia Civil – Teses. 2. Engenharia Geotécnica – Teses. 3. Modelagem numérica;. 4. Modelagem constitutiva;. 5. Grandes deformações;. 6. Geomateriais cimentados;. 7. Viscoplasticidade;. I. Vargas, Eurípedes. II. de Campos, Tácio. III. Pontifícia Universidade Católica do Rio de Janeiro. Departamento de Engenharia Civil e Ambiental. IV. Título.

CDD: 620.11

Acknowledgments

Em primeiro lugar, gostaria de agradecer especialmente a meu orientador Prof. Eurípedes Vargas e coorientador Prof. Tácio de Campos por me incentivar nessa jornada.

Também sou grato aos membros da minha banca examinadora, Prof. Marcio Almeida, Prof.a Deane Rohel, Prof. Antonio Gens e Prof. Massao Futai, que comprometeram muito generosamente seu tempo e conhecimento para avaliar a minha tese.

Quero agradecer à minha esposa e meus pais pelo apoio sincero, que tem sido essencial para perseguir meus objetivos.

Por último, gostaria de agradecer à CAPES pelo apoio financeiro e à PUC-Rio pela bolsa de isenção de mensalidades do doutorado.

This study was financed in part by the Coordenação de Aperfeiçoamento de Pessoal de Nível Superior – Brasil (CAPES) – Finance Code 001.

Abstract

Cirone, Alessandro; Vargas, Eurípedes (Advisor); de Campos, Tácio (Co-Advisor). **Theory and implementation of constitutive models for geomaterials**. Rio de Janeiro, 2020. 164p. Tese de doutorado – Departamento de Engenharia Civil e Ambiental, Pontifícia Universidade Católica do Rio de Janeiro.

A theoretical and numerical study was developed to simulate the stress-strain behavior of soils and rocks, formulating constitutive models able to catch the peculiarities inherent to the behavior of these materials under large strains and structure degradation. Within the Brazilian geotechnical context, the objective of the research was also to investigate constitutive approaches to model the behavior of soft soils, residual soils and sedimentary rocks. The work is divided into the following topics: literature review; study of strain measurements and objective stress rates; definition and development of the constitutive models to be tested; definition of the return mapping algorithms for integrating the constitutive equations; finite element implementation; and simulation of the behavior observed in laboratory tests. Results indicate that the viscous behavior of the Sarapuí soft clay can be correctly reproduced by adopting a viscoplastic constitutive model. The structured soil approach appears to be consistent with the behavior of Vila Velha sandstone. Finally, a decomposition of irreversible strains was proposed to model the behavior of residual soils within a novel constitutive framework.

Keywords

Numerical modeling; Constitutive modeling; Large Strains; Bonded Geomaterials; Viscoplasticity;

Resumo

Cirone, Alessandro; Vargas, Eurípedes; de Campos, Tácio. **Teoria e implementação de modelos constitutivos para geomateriais**. Rio de Janeiro, 2020. 164p. Tese de Doutorado – Departamento de Engenharia Civil e Ambiental, Pontifícia Universidade Católica do Rio de Janeiro.

Desenvolveu-se estudo teórico e numérico para simular o comportamento tensão-deformação de solos e rochas. Procurou-se estabelecer modelagem constitutiva apta a representar as peculiaridades inerentes ao comportamento destes materiais sob grandes deformações e degradação da estrutura. Dentro do contexto geotécnico brasileiro, o objetivo da pesquisa foi, também, investigar uma nova abordagem constitutiva para modelar o comportamento de solos moles, solos residuais e rochas sedimentares. O trabalho está dividido nos seguintes tópicos: revisão bibliográfica; estudo de medidas de deformações e taxas objetivas de tensões; definição e desenvolvimento dos modelos constitutivos a serem testados; definição dos algoritmos de retorno para integração das equações constitutivas; implementação em elementos finitos; simulação do comportamento observado em ensaios de laboratório. Os resultados da pesquisa indicam que o comportamento viscoso da argila mole do Sarapuí pode ser reproduzido corretamente adotando-se modelo constitutivo viscoplástico. A abordagem de solo estruturado está condizente com o comportamento do arenito de Vila Velha. Por fim, para modelar o comportamento de solos residuais dentro de um novo quadro constitutivo, foi proposta uma separação das deformações irreversíveis.

Palavras-chave

Modelagem numérica; Modelagem constitutiva; Grandes deformações; Geomateriais cimentados; Viscoplasticidade;

Table of contents

List of figures

List of tables

List of Symbols

x_i	Current position of a point
a_i , X_i	Reference (initial) configuration
$u_i = x_i - X_i$	Displacement
$v_i = \dfrac{du_i}{dt} = \dfrac{dx_i}{dt}$	Velocity vector

σ_{ij}	Cauchy stress
τ_{ij}	Kirchhoff stress
P_{ij}	First Piola-Kirchhoff stress
S_{ij}	Second Piola-Kirchhoff stress
$\hat{\sigma}_{ij}$	Co-rotational stress

ϵ_{ij}	Small strain tensor
E_{ij}	Green-Lagrange strain tensor
e_{ij}	Euler-Almansi strain tensor
H_{ij}	Hencky, logarithmic or natural strain tensor

$\mathbf{F}$	Deformation gradient
R	Rotation tensor
U	Right stretch tensor
V	Left stretch tensor
B	Right Cauchy-Green tensor
C	Left Cauchy-Green tensor
$J = \det F$	Jacobian determinant
$L = \dot{F}F^{-1}$	Velocity gradient
$D = \operatorname{sym} L$	Rate of deformation tensor
$W = \operatorname{asym} L$	Spin tensor or vorticity
$\Omega = \dot{R}R^T$	polar spin

p	Mean pressure
q	Deviatoric stress
I_1, I_2, I_3	Invariants of stress
$\eta = q/p$	Stress ratio
M	Stress ratio at failure/slope of the critical state line
ϵ_v^p	Plastic volumetric strain
ϵ_s^p	Plastic deviatoric strain
$d = d\epsilon_v^p/d\epsilon_s^p$	Dilatancy
g	Plastic potential
f	Yield surface
λ	Plastic multiplier

1
Introduction

Constitutive modeling is a keystone of successful engineering analysis. The description of material response under certain loading conditions and natural phenomena is mathematically formulated by means of the constitutive equations. Soils and rocks are characterized by strongly non-linear and time-dependent mechanical behavior, including the presence of pore water, micro and macro structure. There are no apparent limitations to the use of standard or commercially available constitutive models for the solution of special engineering problems, if one recognizes that the reliability of the result will depend on the essential material features involved. Clearly, no model can account for all natural phenomena without sophistication. Multiple natural processes may occur simultaneously and the use of advanced constitutive model is, in this case, necessary for reliable calculation results.

It is appropriate, at this point, to put this topic in the specific context of soils and soft rocks existing in Brazil. As a matter of fact, residual soils cover large parts of the Brazilian territory, while soft clay dominates along the coast. These soils, which have been object of research and interest during the last four decades in the Brazilian geotechnical community, need the development of *ad hoc* constitutive models that are capable of reproduce satisfactorily their peculiarities, such as the pronounced creep behavior or the structure degradation typical of soft clay and residual soil, respectively.

This research mainly focused on the idealization, formulation and implementation of new constitutive models ina commercial finite element software (PLAXIS) to make them available to practitioners. Although the developed models do not include all the features of these geomaterials, they involve most of the essential characteristics observed in laboratory testing and engineering experience. The model construction tried to avoid unnecessary sophistication and did not miss the physical meaning of each parameter, as well as the easy obtainment by means of conventional geotechnical tests. For instance, a novel interpretation of the Undrained Hydrostatic Relaxation Test was developed within the context of viscoplastic parameters determination. Moreover, constitutive modeling involved research in the field of continuum mechanics and numerical implementation. Accurate and stable numerical algorithms for the integration of visco-elasto-plastic constitutive relations were also investigated and implemented. In summary, the work consisted of theoretical formulation of constitutive laws, implementation in commercial finite elements code and the final validation against laboratory test data.

The main contributions of the research are the following:

1. A comprehensive literature survey was conducted on the continuum mechanics theory in the context of large strain elastoplasticity.
2. Novel expressions for the yield function and plastic potential were formulated.
3. The Viscous Modified Cam Clay model was formulated, implemented and verified against the laboratory behavior of Sarapuí soft clay, with an unprecedented and consistent interpretation of the Undrained Hydrostatic Relaxation Test in light of Perzyna's classical theory of viscoplasticity (overstress theory).
4. R-Soil, an elastoplastic constitutive model for bonded geomaterials, incorporating the best features of several remarkable literature models, was developed, implemented and validated.
5. A novel approach to constitutive modeling of residual soils based on the decomposition of irreversible strains was proposed.
6. Adopting elementary incremental laws, a family of one-dimensional compression models was theoretically derived for describing the compaction of sediments, capturing the interrelationships between compressibility, porosity and depth of burial and accounting for pore closure under high stress levels.

Chapter 2 presents a review of large deformation theory and elements of continuum mechanics, including definitions of strain measures and details on the multiplicative decomposition. Brief reviews of numerical procedures used in large strain elastoplasticity are presented at the end of this chapter.

Chapter 3 presents general concepts of plasticity theory, constitutive formulations and theoretical assumptions used to model bonded soils and rate-dependent behavior. Several models from literature are also reviewed and trends in yield function and plastic potential are drawn. This chapter includes the experimental determination of the viscous nucleus.

Chapter 4 covers details of elastoplastic integration algorithms. Various return mapping schemes for the integration of constitutive equations are presented, including the integration under mixed control.

Chapter 5 gives detailed descriptions of the constitutive models developed throughout this doctoral research, i.e. the Viscous Modified Cam Clay and the R-Soil model. Their implementation in commercial finite element code is outlined.

Chapter 6 presents the validation of the models against a number of laboratory test results. The behavior of Sarapuí soft clay and Vila Velha sandstone is simulated using finite elements. Determination of model parameters is also discussed.

Two papers are attached in Chapter 7. The former addresses the constitutive modeling of residual soils in triaxial compression, based on the decomposition of irreversible strains. The latter presents the development of several compression models for granular materials derived from elementary incremental laws.

2
Stresses and strains in deforming bodies

Some fundamentals of continuum mechanics are briefly reviewed with particular attention to large deformation theory. The kinematics of motion and the notion of strain are reformulated to account for the distinction between the undeformed and deformed configuration. Different stress measure are also presented. Methods for large strains analysis in elastoplasticity are summarized, allowing for the extension of constitutive models developed in the context of small strains to the large strains regime.

2.1
Description of deformation

Given here is the mathematical description of a deforming continuum body. Consider the motion of a body in a Cartesian coordinate system as shown in Figure 2.1. The deformation can be interpreted as a *geometrical transformation*, in which the equation of transformation is assumed to be a continuous function in the form:

$$x_i = \hat{x}(a_1, a_2, a_3, t) \tag{2-1}$$

where:

$a_i =$ position of point in reference (initial or undeformed) configuration

$x_i =$ position of point in current (deformed) configuration

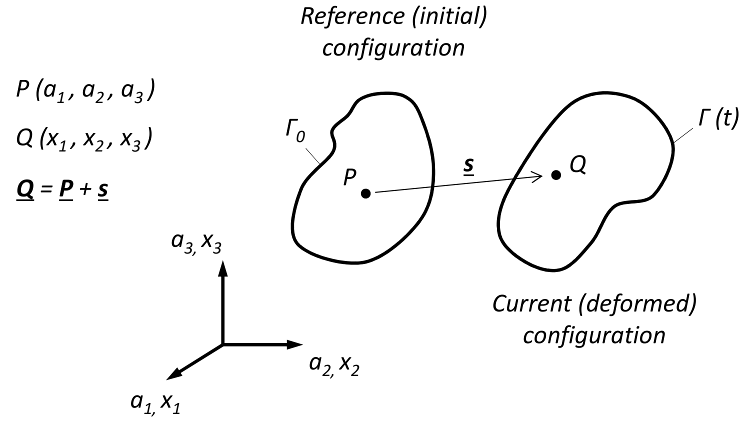

Figure 2.1: Description of deformation in a moving continuum body.

Deformation gradient The Jacobian matrix of the transformation is usually referred as the *deformation gradient tensor*, defined as:

$$F_{ij} = \frac{\partial x_i}{\partial a_j} \quad \text{or} \quad \mathbf{F} = \frac{\partial \mathbf{x}}{\partial \mathbf{a}} \tag{2-2}$$

The deformation gradient can also be expressed as a function of the displacement vector, noting that the position of points in the current (deformed) configuration is given by the initial (reference) position plus the displacement:

$$x_i(a_1, a_2, a_3, t) = a_i + s_i(a_1, a_2, a_3, t)$$

If the vector fields $x_i(a_1, a_2, a_3, t)$ and $s_i(a_1, a_2, a_3, t)$ are assumed to be continuous and differentiable, meaning that no laceration or solid penetration occurs, then the following identity holds:

$$F_{ij} = \frac{\partial x_i}{\partial a_j} = \delta_{ij} + \frac{\partial s_i}{\partial a_j} \quad \text{or} \quad \mathbf{F} = \frac{\partial \mathbf{x}}{\partial \mathbf{a}} = \mathbf{I} + \frac{\partial \mathbf{s}}{\partial \mathbf{a}} \tag{2-3}$$

An important remark is that the displacement vector can be treated as a function either of a_i (undeformed configuration) or x_i (deformed configuration).

Jacobian The determinant of the deformation gradient tensor is usually referred simply as the *Jacobian*:

$$J = \det \mathbf{F} \tag{2-4}$$

It represents the volume ratio of the material element, i.e. $J = V/V_0$. For realistic deformations, it follows that the Jacobian must be always positive; in addition, volume contraction occurs when $0 < J < 1$, whereas $J > 1$ means expansion and $J = 1$ material incompressibility.

Polar decomposition The deformation gradient contains information about both stretch and rotation.

Theorem 2.1 (Truesdell and Noll, 2004) *Any invertible linear transformation* $\mathbf{F}$ *has two unique multiplicative decompositions (see Fig. 2.2):*

$$\mathbf{F} = \mathbf{R}\,\mathbf{U}, \quad \mathbf{F} = \mathbf{V}\,\mathbf{R} \tag{2-5}$$

in which $\mathbf{R}$ *is the rotation tensor (orthogonal),* $\mathbf{U}$ *the right-stretch tensor and* $\mathbf{V}$ *the left-stretch tensor, that are both symmetric and positive-definite. The following relations hold:*

$$\mathbf{U^2} = \mathbf{C} = \mathbf{F}^\mathsf{T}\,\mathbf{F}, \quad \mathbf{V^2} = \mathbf{B} = \mathbf{F}\,\mathbf{F}^\mathsf{T}$$

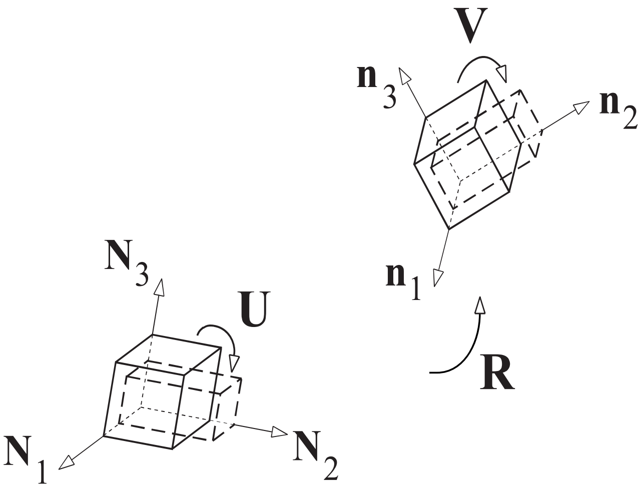

Figure 2.2: Schematic representation of the polar decomposition of deformation gradient. Material element is first stretched by $\mathbf{U}$ and then rotated by $\mathbf{R}$, or first rotated by $\mathbf{R}$ and then stretched by $\mathbf{V}$. The principal directions of $\mathbf{U}$ are $\mathbf{N}_i$, and those of $\mathbf{V}$ are $\mathbf{n}_i = \mathbf{R} \cdot \mathbf{N}_i$. (Lubarda, 2001)

in which $\mathbf{C}$ *and* $\mathbf{B}$ *are called the right and left Cauchy-Green tensors, respectively.*

Principal stretches To determine $\mathbf{U}$, it is necessary to evaluate $\sqrt{\mathbf{C}}$. Algebraic calculations are needed to calculate the square root of a matrix (tensor). A common procedure is to diagonalize $\mathbf{C}$ and take the square roots of the diagonal entries:

$$\mathbf{C} = \mathrm{diag}(\lambda_1^2, \lambda_2^2, \lambda_3^2)$$

where λ_i are the eigenvalues of $\mathbf{U}$, usually referred as *principal stretches* of the deformation. It can be shown that the determinants of the stretch tensors and Cauchy-Green tensors are related to the Jacobian (Truesdell and Noll, 2004):

$$\begin{aligned} J =& \lambda_1 \lambda_2 \lambda_3 = \det \mathbf{U} = \det \mathbf{V} \\ J^2 =& \lambda_1^2 \lambda_2^2 \lambda_3^2 = \det \mathbf{B} = \det \mathbf{C} \end{aligned} \tag{2-6}$$

Velocity gradient According to Fung and Tong (2001), the *velocity field* is the time derivative of the trajectory $\hat{x}(a_1, a_2, a_3, t)$, given in Equation 2-1:

$$\mathbf{v}(\mathbf{x}, t) = \dot{x}_i = \frac{\partial \mathbf{x}(\mathbf{a}, t)}{\partial t} = \frac{d\mathbf{s}}{dt} \tag{2-7}$$

Then the material time derivative of deformation gradient is:

$$\dot{\mathbf{F}} = \frac{D\mathbf{F}}{Dt} = \frac{\partial \dot{\mathbf{x}}}{\partial \mathbf{a}} = \frac{\partial \dot{\mathbf{x}}}{\partial \mathbf{x}} \cdot \frac{\partial \mathbf{x}}{\partial \mathbf{a}} = \mathbf{L}\,\mathbf{F} \tag{2-8}$$

It follows that $\mathbf{L}$ is nothing but the spatial gradient of the velocity field (Truesdell and Noll, 2004):

$$\mathbf{L} = \dot{\mathbf{F}}\,\mathbf{F}^{-1} = \frac{\partial \dot{\mathbf{x}}}{\partial \mathbf{x}} = \frac{\partial \mathbf{v}}{\partial \mathbf{x}} \quad \text{or} \quad L_{ij} = \frac{\partial v_i}{\partial x_j} \tag{2-9}$$

Both velocity field and velocity gradient are Eulerian descriptions of motion.

Rate of deformation and Spin The velocity gradient $\mathbf{L}$ is not necessarily symmetric; it is possible to express it as the sum of its symmetric and antisymmetric parts:

$$\mathbf{L} = \mathbf{D} + \mathbf{W}$$

The symmetric part of $\mathbf{L}$ is the *rate of deformation tensor*, also called as velocity strain tensor or stretching tensor (Bathe, 2006):

$$\mathbf{D} = \frac{1}{2}(\mathbf{L} + \mathbf{L}^{\mathsf{T}}) \tag{2-10}$$

while the *spin tensor*, also called as rate of rotation or vorticity tensor, is the antisymmetric (skew) part:

$$\mathbf{W} = \frac{1}{2}(\mathbf{L} - \mathbf{L}^{\mathsf{T}}) \tag{2-11}$$

According to Truesdell (1966), $\mathbf{W}$ is generally different from $\dot{\mathbf{R}}$ and the stretching $\mathbf{D}$ is entirely different from $\dot{\mathbf{U}}$. As a matter of fact, the following formulae can be derived from the polar decomposition (Eq. 2-5):

$$\begin{aligned} \mathbf{W} =& \dot{\mathbf{R}}\,\mathbf{R}^{\mathsf{T}} + \tfrac{1}{2}\mathbf{R}(\dot{\mathbf{U}}\,\mathbf{U}^{-1} - \mathbf{U}^{-1}\dot{\mathbf{U}})\mathbf{R}^{\mathsf{T}} \\ \mathbf{D} =& \tfrac{1}{2}\mathbf{R}(\dot{\mathbf{U}}\,\mathbf{U}^{-1} + \mathbf{U}^{-1}\dot{\mathbf{U}})\mathbf{R}^{-1} \end{aligned} \tag{2-12}$$

The product $\dot{\mathbf{R}}\,\mathbf{R}^{\mathsf{T}}$ is a skew-symmetric spin, called as *rate of rotation tensor*, polar spin or body spin:

$$\boldsymbol{\Omega} = \dot{\mathbf{R}}\,\mathbf{R}^{\mathsf{T}} \tag{2-13}$$

and represents the angular velocity associated with the local rotation $\mathbf{R}$ (Johnson and Bammann, 1984). From Equations 2-5, 2-9 and 2-13, the following equalities can be derived (Dienes, 1979; Reinhardt and Dubey, 1996):

$$\begin{aligned} &\mathbf{L} = \dot{\mathbf{V}}\,\mathbf{V}^{-1} + \mathbf{V}\boldsymbol{\Omega}\,\mathbf{V}^{-1} \\ &(\mathbf{W} - \boldsymbol{\Omega})\mathbf{V} + \mathbf{V}(\mathbf{W} - \boldsymbol{\Omega}) = \mathbf{V}\mathbf{D} - \mathbf{D}\mathbf{V} \end{aligned} \tag{2-14}$$

2.1.1
Analysis of strain measures

Strain is a measure of deformation. There are various strain measures that can be utilized in order to quantify the amount of deformation suffered by the body. Consider the the deformation shown in Figure 2.3. Following

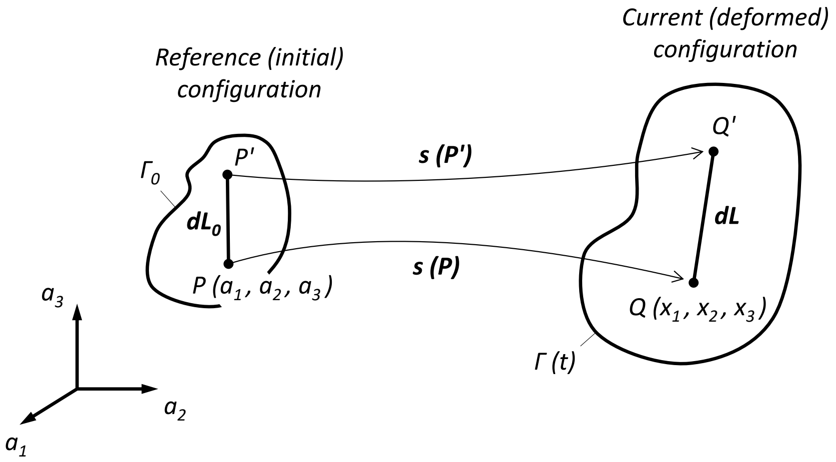

Figure 2.3: Deformation of an element of infinitesimal length.

Fung and Tong (2001), in the initial (reference) configuration, the square of the length of the infinitesimal element, connecting the point $P(a_1, a_2, a_3)$ to $P'(a_1 + da_1, a_2 + da_2, a_3 + da_3)$, is:

$$dl_0^2 = \delta_{ij}\, da_i\, da_j = \delta_{ij}\, \frac{\partial a_i}{\partial x_l}\, \frac{\partial a_j}{\partial x_m}\, dx_l\, dx_m$$

where δ_{ij} is Kronecker delta. In the current (deformed) configuration, the body is described by new coordinates x_1, x_2, x_3; the point P is moved to Q and P' to Q'. Then, the element length becomes:

$$dl^2 = \delta_{ij}\, dx_i\, dx_j = \delta_{ij}\, \frac{\partial x_i}{\partial a_l}\, \frac{\partial x_j}{\partial a_m}\, da_l\, da_m$$

The difference between the squares of the length elements may be written either as:

$$dl^2 - dl_0^2 = \underbrace{\left(\delta_{lm} \frac{\partial x_l}{\partial a_i}\, \frac{\partial x_m}{\partial a_j} - \delta_{ij}\right)}_{2E_{ij}\,:\,\text{Green strain}}\, da_i\, da_j$$

or as

$$dl^2 - dl_0^2 = \underbrace{\left(\delta_{ij} - \delta_{lm} \frac{\partial a_l}{\partial x_i}\, \frac{\partial a_m}{\partial x_j}\right)}_{2e_{ij}\,:\,\text{Almansi strain}}\, dx_i\, dx_j$$

The components of the *Green-Lagrange* and *Almansi-Euler* strain tensor can be defined in a number of different but completely equivalent way:

$$\mathbf{E} = \tfrac{1}{2}(\mathbf{F}^{\mathsf{T}}\mathbf{F} - \mathbf{I}) = \tfrac{1}{2}(\mathbf{C} - \mathbf{I}) = \tfrac{1}{2}(\mathbf{U}^2 - \mathbf{I})$$

$$\mathbf{e} = \tfrac{1}{2}(\mathbf{I} - \mathbf{F}^{-\mathsf{T}}\mathbf{F}^{-1}) = \tfrac{1}{2}(\mathbf{I} - \mathbf{B}^{-1}) = \tfrac{1}{2}(\mathbf{I} - \mathbf{V}^{-2})$$

Where the Cauchy-Green left and right tensors, respectively $\mathbf{C}$ and $\mathbf{B}$, have been already introduced. They are both symmetric and positive definite (Fung and Tong, 2001). Strain tensors are more commonly expressed in terms of derivatives of the displacement vector:

$$E_{ij} = \frac{1}{2}\left(\frac{\partial s_j}{\partial a_i} + \frac{\partial s_i}{\partial a_j} + \frac{\partial s_k}{\partial a_i}\frac{\partial s_k}{\partial a_j}\right) \tag{2-15}$$

$$e_{ij} = \frac{1}{2}\left(\frac{\partial s_j}{\partial x_i} + \frac{\partial s_i}{\partial x_j} - \frac{\partial s_k}{\partial x_i}\frac{\partial s_k}{\partial x_j}\right) \tag{2-16}$$

Note that the displacement vector $s_i = (s_1, s_2, s_3)$ can be treated as a function either of a_i or x_i. The position of points in the body in reference (undeformed) configuration is considered when the Green-Lagrange strain tensor is evaluated. Whereas, the position of points in the current (deformed) configuration is considered when the Almansi-Euler strain tensor is evaluated.

If first derivatives of $\mathbf{s}$ are so small that the squares and products are negligible, then one derives the definition of *Cauchy infinitesimal strain* tensor:

$$\epsilon_{ij} = \frac{1}{2}\left(\frac{\partial s_j}{\partial x_i} + \frac{\partial s_i}{\partial x_j}\right) \tag{2-17}$$

It means that in infinitesimal displacement case, since $a_i \simeq x_i$, the distinction between the Lagrangian and Eulerian strain tensors disappears (Fung and Tong, 2001)[p. 102].

Another popular strain measure is the *logarithmic strain*, defined as:

$$\begin{aligned} \mathbf{H} &= \ln \mathbf{U} = \tfrac{1}{2}\ln \mathbf{C} \\ \bar{\mathbf{H}} &= \ln \mathbf{V} = \tfrac{1}{2}\ln \mathbf{B} \end{aligned} \tag{2-18}$$

they are also referred as the logarithmic strain tensors of Hencky (Wang and Truesdell, 1973).

In the interests of completeness of the information, fundamental strain and stress measures are provided in Tables 2.1 and 2.2, to enable the reader to follow the implications and discussions described in the next sections.

2.2
Multiplicative decomposition

The polar decomposition in Eq. 2-5 states that any deformation process can be decomposed in *stretch* and *rotation*. For the case of finite elastoplastic deformation, a product decomposition is applied in a similar fashion, assuming that the deformation gradient ($\mathbf{F}$) can be decomposed as the product of *elastic* ($\mathbf{F}^e$) and *plastic* ($\mathbf{F}^p$) contributions:

$$\mathbf{F} = \mathbf{F}^e\,\mathbf{F}^p = \hat{\mathbf{F}}^e \cdot \hat{\mathbf{F}}^p \tag{2-19}$$

Table 2.1: Strain measures

Strain Measure	Definition	Reference frame
Green-Lagrange	$\mathbf{E} = \frac{1}{2}(\mathbf{C} - \mathbf{I})$	Lagrangian (undeformed)
Almansi-Euler	$\mathbf{e} = \frac{1}{2}(\mathbf{I} - \mathbf{B}^{-1})$	Eulerian (deformed)
Natural (logarithmic)	$\mathbf{H} = \ln \mathbf{U}$ $\bar{\mathbf{H}} = \ln \mathbf{V}$	Lagrangian - Eulerian
Engineering	$\epsilon_{ij} = \frac{1}{2}(\frac{\partial s_i}{\partial a_j} + \frac{\partial s_j}{\partial a_i})$	Lagrangian
Cauchy	$\epsilon_{ij} = \frac{1}{2}(\frac{\partial s_i}{\partial x_j} + \frac{\partial s_j}{\partial x_i})$	Eulerian
Deformation gradient	$F_{ij} = \frac{\partial x_i}{\partial a_j} = \delta_{ij} + \frac{\partial s_i}{\partial a_j}$	Lagrangian-Eulerian "Two-point tensor"

Table 2.2: Summary of relations among stress measures (Nemat-Nasser, 2003).

Name, notation	$\boldsymbol{\sigma}$	$\boldsymbol{\tau}$	$\mathbf{P}$	$\mathbf{S}$
Cauchy, $\boldsymbol{\sigma}$	$\boldsymbol{\sigma}$	$\frac{1}{J}\boldsymbol{\tau}$	$\frac{1}{J}\mathbf{P}\,\mathbf{F}^{\mathsf{T}}$	$\frac{1}{J}\mathbf{F}\,\mathbf{S}\,\mathbf{F}^{\mathsf{T}}$
Kirchhoff, $\boldsymbol{\tau}$	$J\boldsymbol{\sigma}$	$\boldsymbol{\tau}$	$\mathbf{P}\,\mathbf{F}^{\mathsf{T}}$	$\mathbf{F}\,\mathbf{S}\,\mathbf{F}^{\mathsf{T}}$
1st Piola-Kirchhoff, $\mathbf{P}$	$J\boldsymbol{\sigma}\mathbf{F}^{-\mathsf{T}}$	$\boldsymbol{\tau}\mathbf{F}^{-\mathsf{T}}$	$\mathbf{P}$	$\mathbf{F}\,\mathbf{S}$
2nd Piola-Kirchhoff, $\mathbf{S}$	$J\,\mathbf{F}^{-1}\,\boldsymbol{\sigma}\mathbf{F}^{-\mathsf{T}}$	$\mathbf{F}^{-1}\,\boldsymbol{\tau}\mathbf{F}^{-\mathsf{T}}$	$\mathbf{F}^{-1}\,\mathbf{P}$	$\mathbf{S}$

that is the *multiplicative decomposition* of the deformation gradient, introduced by Lee (1969) and Lee and Liu (1967). As shown in Figure 2.4, the plastic deformation gradient $\mathbf{F}^p$ defines a local *unstressed intermediate configuration*, mapping from the initial state to the intermediate configuration, while the elastic deformation gradient $\mathbf{F}^e$ maps from the intermediate state to the final configuration. The order of factors in Eq. 2-19 reflects this particular sequence of deformations: the first deformation is *purely plastic* and the second is *purely elastic*. In this manner, the plastic configuration may be recovered from current configuration by reversing the elastic deformation:

$$\mathbf{F}^p = (\mathbf{F}^e)^{-1}\,\mathbf{F} \tag{2-20}$$

As the elastic strains are removed, in the plastic configuration the stresses acting on the body $\mathcal{B}_p$ are zero. Moreover, $\mathbf{F}^e$ and $\mathbf{F}^p$ are not uniquely defined because the intermediate unstressed configuration is not unique, since arbitrary rotations can be locally superposed preserving it unstressed (Lubarda, 2001). The elastic gradient $\mathbf{F}^e$ can be imagined as the rotation $\mathbf{R}^e$ followed by elastic stretch $\mathbf{V}^e$; and the plastic gradient $\mathbf{F}^p$ as the plastic stretch $\mathbf{U}^p$ followed by the rotation $\mathbf{R}^p$. Therefore, there exists a decomposition:

$$\mathbf{F} = \mathbf{V}^e\,\mathbf{R}^{ep}\,\mathbf{U}^p \tag{2-21}$$

such that $\mathbf{R}^{ep} = \hat{\mathbf{R}}^{ep} = \mathbf{R}^{e} \cdot \mathbf{R}^{p} = \hat{\mathbf{R}}^{e} \cdot \hat{\mathbf{R}}^{p}$ is unique (Lubarda, 2001). In this decomposition the material element is first stretched by $\mathbf{U}^{p}$ and then rotated by $\mathbf{R}^{ep}$ and finally stretched by $\mathbf{V}^{e}$ according to the polar decomposition (see Fig. 2.2). As discussed by Weber and Anand (1990), the definition of intermediate configuration can also be specified by requiring that the elastic unloading takes place without rotation,

$$\bar{\mathbf{F}}^{p} = (\mathbf{V}^{e})^{-1}\,\mathbf{F} \tag{2-22}$$

the configuration determined in this manner has been referred as *favored unstressed configuration*. Then, comparing Eqs. 2-20 and 2-22, it is possible to make the connection that

$$\bar{\mathbf{F}}^{p} = \mathbf{R}^{e}\,\mathbf{F}^{p} \tag{2-23}$$

showing that the favored unstressed configuration $\bar{\mathbf{F}}^{p}$ differs from the pure plastic deformation $\mathbf{F}^{p}$ by the rotation $\mathbf{R}^{e}$.

Alternatively, the intermediate configuration may be specified according to the crystal plasticity theory (Asaro, 1983), assuming that plastic distortion takes place without rotation,

$$\tilde{\mathbf{F}}^{p} = \mathbf{U}^{p} = \mathbf{V}^{p} \tag{2-24}$$

in this case the intermediate configuration is *isoclinic* and the orientation of the lattice is fixed, through a triad of orthogonal vectors attached to the initial configuration.

The velocity gradients $\mathbf{L}$ and $\mathbf{L}^{p}$, corresponding to the fields $\boldsymbol{v}$ and $\boldsymbol{v}^{p}$ shown in Figure 2.4, are related as follows:

$$\mathbf{L} = \dot{\mathbf{F}}\mathbf{F}^{-1} = \dot{\mathbf{F}}^{e}(\mathbf{F}^{e})^{-1} + \mathbf{F}^{e}\mathbf{L}^{p}(\mathbf{F}^{e})^{-1} = \mathbf{L}^{e} + \bar{\mathbf{L}}^{p} \tag{2-25}$$

where $\mathbf{L}^{p}$ represents the plastic velocity gradient of the intermediate configuration:

$$\mathbf{L}^{p} = \dot{\mathbf{F}}^{p}(\mathbf{F}^{p})^{-1} = \partial v_i^p / \partial x_j^p$$

It should not be confused with $\bar{\mathbf{L}}^{p}$, that is the *spatial* plastic velocity gradient additive to $\mathbf{L}^{e}$. It carries the combined effects of elastic and plastic deformations. The *pure* plastic velocity gradient $\mathbf{L}^{p}$ is interconnected to $\bar{\mathbf{L}}^{p}$ by the elastic pull-back transformation:

$$\mathbf{L}^{p} = (\mathbf{F}^{e})^{-1}\bar{\mathbf{L}}^{p}\,\mathbf{F}^{e} \tag{2-26}$$

The multiplicative decomposition does not prevent the additivity of the strains. However, it affects the way any observer - the lagrangian, eulerian and

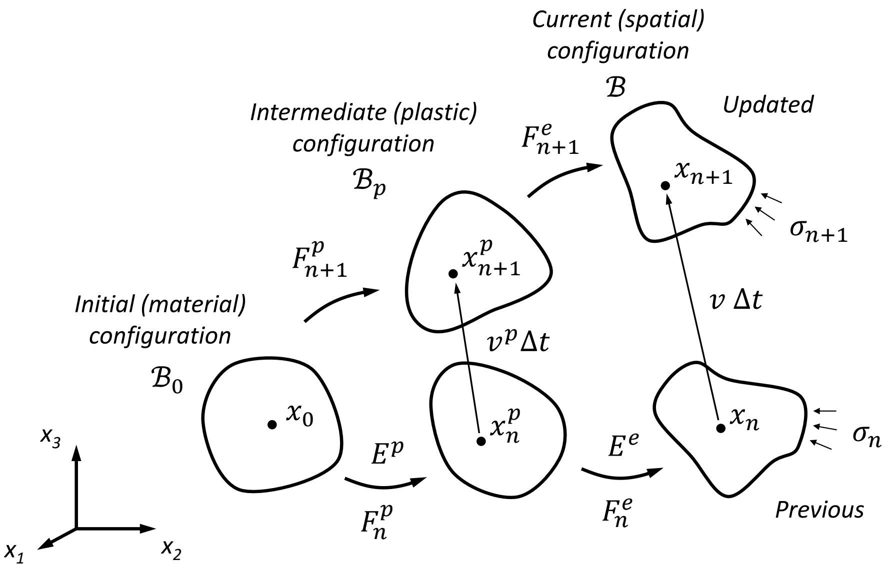

Figure 2.4: Multiplicative decomposition. The previous configuration is known and is described by the deformation gradients $\mathbf{F}_n = \mathbf{F}^e_n\,\mathbf{F}^p_n$. The vector $\boldsymbol{v}\,\Delta t$ gives the displacement of the particle x_n from its previous place to its updated place x_{n+1} in the spatial configuration $\mathcal{B}$. Similarly, the vector $\boldsymbol{v}^p\,\Delta t$ gives the displacement of the intermediate configuration $\mathcal{B}_p$ from previous x^p_n to updated x^p_{n+1} state.

intermediary - measures the total strain and its elastic and plastic parts. The eulerian observer, as instance, measures the *Almansi* strain:

$$\mathbf{e} = \frac{1}{2}(\mathbf{I} - \mathbf{F}_e^{-\mathsf{T}}\mathbf{F}_p^{-\mathsf{T}}\mathbf{F}_p^{-1}\mathbf{F}_e^{-1}) = \frac{1}{2}(\mathbf{I} - \mathbf{F}_e^{-\mathsf{T}}\mathbf{F}_e^{-1}) + \mathbf{F}_e^{-\mathsf{T}}\mathbf{e}_p\mathbf{F}_e^{-1} = \mathbf{e}^e + \bar{\mathbf{e}}^p \qquad (2\text{-}27)$$

in which the *pure* plastic Almansi strain has been introduced according to the definition $\mathbf{F}_p^{-\mathsf{T}}\mathbf{F}_p^{-1} = \mathbf{I} - 2\mathbf{e}_p$. Whereas the lagrangian observer measures the *Green* strain:

$$\mathbf{E} = \frac{1}{2}(\mathbf{F}_p^{\mathsf{T}}\mathbf{F}_e^{\mathsf{T}}\mathbf{F}_e\mathbf{F}_p - \mathbf{I}) = \mathbf{F}_p^{\mathsf{T}}\mathbf{E}_e\mathbf{F}_p + \frac{1}{2}(\mathbf{F}_p^{\mathsf{T}}\mathbf{F}_p - \mathbf{I}) = \bar{\mathbf{E}}^e + \mathbf{E}^p \qquad (2\text{-}28)$$

in which the *pure* elastic Green strain has been introduced according to the definition $\mathbf{F}_e^{\mathsf{T}}\mathbf{F}_e = 2\mathbf{E}_e + \mathbf{I}$. In the intermediate configuration, the observer decomposes additively the strains into a *pure* elastic *Green* tensor and a *pure* plastic *Almansi* tensor. The summation of these two *pure strains* gives the intermediate total strain tensor. This is outlined herein according to Haupt (2000). The strain tensor which acts on the intermediate configuration is:

$$\boldsymbol{\gamma} = (\mathbf{F}^p)^{-\mathsf{T}}\mathbf{E}(\mathbf{F}^p)^{-1} \qquad (2\text{-}29)$$

and decomposes according to the multiplicative decomposition (Eq. 2-19) and the definition of Green strain (Eq. 2-15) as follows:

$$\gamma = \frac{1}{2}\mathbf{F}_p^{-\mathsf{T}}(\mathbf{F}^{\mathsf{T}}\mathbf{F} - \mathbf{I})\mathbf{F}_p^{-1} = \frac{1}{2}(\mathbf{F}_e^{\mathsf{T}}\mathbf{F}_e - \mathbf{F}_p^{-\mathsf{T}}\mathbf{F}_p^{-1}) \tag{2-30}$$

This equation suggests the additive decomposition of the total strain

$$\boldsymbol{\gamma} = \boldsymbol{\gamma}^e + \boldsymbol{\gamma}^p \tag{2-31}$$

into a *pure* elastic *Green* part

$$\boldsymbol{\gamma}^e = \frac{1}{2}(\mathbf{F}_e^{\mathsf{T}}\mathbf{F}_e - \mathbf{I}) = \mathbf{E}^e \tag{2-32}$$

and a *pure* plastic *Almansi* part

$$\boldsymbol{\gamma}^p = \frac{1}{2}(\mathbf{I} - \mathbf{F}_p^{-\mathsf{T}}\mathbf{F}_p^{-1}) = \mathbf{e}^p \tag{2-33}$$

Strain rates As a result, the corresponding rate tensors in the intermediate configuration are obtained by material time differentiation of the Green strain defined in Equation 2-28. For the plastic part, the rate of strain in the *material* configuration is:

$$\dot{\mathbf{E}}^p = \frac{1}{2}(\dot{\mathbf{F}}_p^{\mathsf{T}}\mathbf{F}_p + \mathbf{F}_p^{\mathsf{T}}\dot{\mathbf{F}}_p) \tag{2-34}$$

and recalling the definition of velocity gradient and rate of deformation (provided in Eqs. 2-9 and 2-10), the *pure* plastic rate of deformation tensor is obtained by the same transformation applied to the plastic strain tensor itself:

$$\mathbf{D}_p = \mathbf{F}_p^{-\mathsf{T}}\dot{\mathbf{E}}_p\mathbf{F}_p^{-1} = \dot{\mathbf{e}}_p + \mathbf{L}_p^{\mathsf{T}}\mathbf{e}_p + \mathbf{e}_p\mathbf{L}_p = \overset{\triangledown}{\mathbf{e}}_p \tag{2-35}$$

In other words, the plastic rate of deformation $\mathbf{D}_p = \overset{\triangledown}{\gamma}_p$ corresponds to the objective Oldroyd rate of the plastic *Almansi* tensor. Analogously, the elastic rate of deformation in the intermediate configuration is:

$$\bar{\mathbf{D}}_e = \mathbf{F}_p^{-\mathsf{T}}\dot{\mathbf{E}}_e\mathbf{F}_p^{-1} = \dot{\mathbf{E}}_e + \mathbf{L}_p^{\mathsf{T}}\mathbf{E}_e + \mathbf{E}_e\mathbf{L}_p = \overset{\triangledown}{\mathbf{E}}_e \tag{2-36}$$

And for the strain rate, the following decomposition is obtained (Haupt, 2000):

$$\overset{\triangledown}{\gamma} = \overset{\triangledown}{\gamma}_e + \overset{\triangledown}{\gamma}_p = \bar{\mathbf{D}}_e + \mathbf{D}_p \tag{2-37}$$

Work conjugacy Finally, all that remains is to define the stress tensor $\boldsymbol{\tau}$ acting on the intermediate configuration that is work-conjugate to $\boldsymbol{\gamma}$. According to Hoger (1987), the concept of conjugate stress and strain was introduced by Hill, who first stated that a stress $\mathbf{S}$ and a strain measure $\mathbf{E}$ are said to be a conjugate pair if the product $\ell := \frac{1}{\rho_0}\mathbf{S}\cdot\dot{\mathbf{E}}$ gives the rate of work done per unit mass. The physical scalar product $\frac{1}{\rho_0}\mathbf{S}\cdot\dot{\mathbf{E}}$ remains invariant because the rate of work input per unit mass is the same for every observer:

$$\rho_0\,\ell := \mathbf{S}\cdot\dot{\mathbf{E}} = J\boldsymbol{\sigma}\cdot\mathbf{D} = \boldsymbol{\tau}\cdot\overset{\triangledown}{\gamma} \tag{2-38}$$

where $\mathbf{S}$ and $\dot{\mathbf{E}}$ are, respectively, the 2nd Piola-Kirchhoff stress and the Green strain rate operating on the initial (material) configuration; $J\boldsymbol{\sigma}$ and $\mathbf{D}$ are, respectively, the weighted Cauchy stress - that is equivalent to the Kirchhoff stress - and the rate of deformation acting on the current (spatial) configuration; $\boldsymbol{\tau}$ and $\overset{\triangledown}{\gamma}$ are, respectively, the 2nd Piola-Kirchhoff stress and the objective strain rate acting on the intermediate (plastic) configuration. Between the foregoing stresses, the following relations hold (Haupt, 2000)[p.320]:

$$\begin{aligned} \mathbf{S} &= \mathbf{F}^{-1}J\boldsymbol{\sigma}\mathbf{F}^{-\mathsf{T}} = \mathbf{F}_p^{-1}\boldsymbol{\tau}\mathbf{F}_p^{-\mathsf{T}} \\ \boldsymbol{\tau} &= \mathbf{F}_p\mathbf{S}\mathbf{F}_p^{\mathsf{T}} = \mathbf{F}_e^{-1}J\boldsymbol{\sigma}\mathbf{F}_e^{-\mathsf{T}} \end{aligned} \tag{2-39}$$

Exponential mapping For an implicit backward Euler integration scheme, $\mathbf{L}^p$ can be assumed constant and fixed (evaluated in the updated configuration at the end of the integration step), leading to the following exponential integration of the plastic deformation gradient:

$$\mathbf{F}^p_{n+1} = \exp(\mathbf{L}^p\Delta t)\mathbf{F}^p_n \tag{2-40}$$

The proof of Eq. 2-40 is presented herein according to Pipkin (1972). By definition (see Eq. 2-9), the material derivative of the deformation gradient is:

$$\dot{\mathbf{F}} = \mathbf{L}\,\mathbf{F} \tag{2-41}$$

if $\mathbf{L}$ is a constant matrix, then

$$\int_{t_n}^{t_{n+1}} \frac{\dot{\mathbf{F}}}{\mathbf{F}}\,dt = \int_{t_n}^{t_{n+1}} \mathbf{L}\,dt \quad \rightarrow \mathbf{F}_{n+1} = \exp(\mathbf{L}\,\Delta t)\mathbf{F}_n \tag{2-42}$$

with the exponential matrix defined by

$$\exp(\mathbf{L}\,\Delta t) = \sum_{n=0}^{\infty} \frac{1}{n!}\Delta t^n\,\mathbf{L}^n \tag{2-43}$$

Flow rule The exponential integration of the velocity gradient $\mathbf{L}^p = \dot{\mathbf{F}}^p(\mathbf{F}^p)^{-1}$ (Eq. 2-40) gives the plastic configuration of the body $\mathcal{B}_p$, at any time, by product superposition of $\Delta\mathbf{F}^p = \exp(\mathbf{L}^p\,\Delta t)$ over the previous plastic state $\mathbf{F}^p_n$. The response function for $\mathbf{L}^p$ is taken to be governed by a flow rule (Weber and Anand, 1990), in general derived from a *dissipation function* (Ziegler and Wehrli, 1987). In general, the plastic behavior is assumed to be isotropic, therefore the skew part of the plastic velocity gradient is kept zero. In the infinitesimal theory, the flow rule is formulated in terms of Cauchy stress and plastic rate of strain, but it could be also in terms of Kirchhoff stress and plastic rate of strain if the dissipated energy is taken per unit undeformed (or unstressed) volume. Therefore, a first option is to prescribe the flow rule in the spatial configuration, preserving the structure of the infinitesimal theory:

$$\bar{\mathbf{D}}^p = \operatorname{sym} \bar{\mathbf{L}}^p = \dot{\lambda} \frac{\partial g}{\partial \boldsymbol{\sigma}} \tag{2-44}$$

and exploiting the additivity with $\mathbf{D}^e$. The second option is to specify a flow rule for the intermediate plastic configuration itself:

$$\mathbf{D}^p = \operatorname{sym} \mathbf{L}^p = \dot{\lambda} \frac{\partial g}{\partial \boldsymbol{\tau}} \tag{2-45}$$

where $\boldsymbol{\tau} = (\mathbf{F}^e)^{-1} J \boldsymbol{\sigma} (\mathbf{F}^e)^{-\mathsf{T}}$ is the pull-back of the Kirchhoff stress, i.e. the 2$^{\text{nd}}$ Piola-Kirchhoff stress. As shown previously, this stress is work-conjugated to the objective elastic Green-Strain rate $\bar{\mathbf{D}}^e = (\mathbf{F}^e)^{\mathsf{T}} \mathbf{D}^e \mathbf{F}^e$, that is the pull-back of the elastic rate of deformation tensor. In this case, recall that $\boldsymbol{\tau}$ and $\bar{\mathbf{D}}^e$ operate on the intermediate (unstressed) configuration.

Constitutive model formulation The thermomechanical framework developed by Ziegler and Wehrli (1987) permits to derive the constitutive equations of any material directly from thermodynamic principles (see also Houlsby and Puzrin, 2000a,b; Collins and Houlsby, 1997; for a specific discussion on granular materials refer to Collins and Muhunthan, 2003). The central result of the theory is that in an isothermal process the input rate of work (i.e. the power of deformation) is equal to the sum of the rate of change of free energy and the mechanical dissipation:

$$\dot{W} = \dot{\psi} + \dot{\phi} \tag{2-46}$$

where $\dot{\psi}$ represents the rate of change of recoverable energy and $\dot{\phi}$ is the rate at which energy is dissipated. For an elastoplastic material, the free energy function depends on a set of independent state variables γ_{ij}, γ_{ij}^p, θ - i.e two strain tensors and the temperature - provided that $\gamma_{ij} - \gamma_{ij}^p = \gamma_{ij}^e$ is the elastic strain (Ziegler and Wehrli, 1987). In addition, for rate-independent behavior the dissipation function is homogeneous of the first degree in the plastic strain rates D_{ij}^p and may be a function of the state variables, too. Under these assumptions, the elastic rate of work per unit intial (undeformed) volume is:

$$\tau_{ij} \bar{D}_{ij}^e = \frac{\partial \psi}{\partial \gamma_{ij}} \bar{D}_{ij}^e \tag{2-47}$$

and the plastic rate of work is:

$$\tau_{ij} D_{ij}^p = \left(\frac{\partial \psi}{\partial \gamma_{ij}^p} + \frac{\partial \dot{\phi}}{\partial D_{ij}^p} \right) D_{ij}^p \tag{2-48}$$

Implications of the multiplicative decomposition Simo and Hughes (1998) point out the implications of the multiplicative decomposition (Eq. 2-19):

(i) the stress-strain relationships derive from a stored function formulated relative to the intermediate configuration;

(ii) the exponential integration of the flow rule, in conjunction with the use of logarithmic strain measures (Cuitino and Ortiz, 1992), reduce to the classical return mapping algorithm of the infinitesimal theory (Haupt, 2000):

Strain Decomposition

$$\mathbf{F} = \mathbf{F}^e\mathbf{F}^p \quad \Longleftrightarrow \quad \boldsymbol{\gamma} = \boldsymbol{\gamma}^e + \boldsymbol{\gamma}^p$$

Hyperelastic Relations

$$\boldsymbol{\tau} = \frac{\partial \psi}{\partial \boldsymbol{\gamma}^e} \quad \Longleftrightarrow \quad \overset{\triangledown}{\boldsymbol{\tau}} = \frac{\partial^2 \psi}{\partial \boldsymbol{\gamma}^e \partial \boldsymbol{\gamma}^e} \overset{\triangledown}{\boldsymbol{\gamma}}^e$$

Flow Rule

$$\mathbf{F}^p_{n+1} = \exp(\mathbf{L}^p \Delta t)\mathbf{F}^p_n \quad \Longleftrightarrow \quad \overset{\triangledown}{\boldsymbol{\gamma}}^p = \mathbf{D}^p = \dot{\lambda}\frac{\partial g}{\partial \boldsymbol{\tau}}$$

Yield Function

$$f(\boldsymbol{\tau} - \boldsymbol{\alpha}, k) = 0$$

Kinematic Hardening

$$\overset{\triangledown}{\boldsymbol{\alpha}} = c\mathbf{D}^p - b\dot{s}_p(t)\boldsymbol{\alpha}$$

Isotropic Hardening

$$k = k(s_p)$$

Plastic Arclength

$$\dot{s}_p(t) = \|\mathbf{D}^p\|$$

(iii) the entire algorithmic procedure can be linearized leading to a closed-form expression for the consistent tangent elastoplastic moduli.

2.3
Approaches, numerical implementation and algorithms in large strains and plasticity

This section aims to address some important formulations presented in the literature, providing an overview of the different algorithms that has been implemented especially in the context of finite elements.

(i) Use the total formulation:

$$ {}^{t}_{0}S_{ij} = {}^{t}_{0}C_{ijhk}\,{}^{t}_{0}E_{hk} \tag{2-49} $$

In a Lagrangian description of motion, all static and kinematic variables are referred to the initial configuration. For this reason, the formulation involves the 2$^{\text{nd}}$ Piola-Kirchhoff stress and the Green-Lagrange strain tensor, both referred to the configuration at time 0 (Bathe et al., 1975).

(ii) Use the rate formulation:

$$ {}^{t}\overset{\nabla}{\tau}_{ij} = {}_{t}C_{ijrs}\,{}_{t}D_{rs} \tag{2-50} $$

where ${}^{t}\overset{\nabla}{\tau}_{ij}$ is an objective stress rate, ${}_{t}C_{ijrs}$ is the constitutive tensor and $D_{rs} = \text{sym}(L_{rs})$ is the rate of deformation tensor, i.e. the symmetric part of the velocity gradient. The rate formulation is an Eulerian description of motion. Most solution schemes have followed a formulation similar to that of McMeeking and Rice (1975), whose theoretical development was largely based on the work of Hill (1959). The Jaumann rate of Kirchhoff stress has been used in practice because, unlike Cauchy stress, its use leads to a symmetric tangent stiffness matrix (Lubliner, 2008), although it results in numerical integration errors and a nonphysical "oscillatory" behavior in the elastic range (Bathe, 2006). The rate formulations derive from the time differentiation of the stress field:

$$ \dot{\sigma}_{ij} = \frac{\partial \sigma_{ij}}{\partial x_k}\frac{\partial x_k}{\partial t} + \frac{\partial \sigma_{ij}}{\partial t} = v_k \partial_k \sigma_{ij} + \partial_t \sigma_{ij} \tag{2-51} $$

According to Prager (2004), $\dot{\sigma}_{ij}$ represents the material rate of change of the stress components with respect to a *fixed* coordinate system. The first term on the right side is the "convective part" and the second is the "local part". The tensor $\dot{\sigma}_{ij}$ cannot be used to represent the stress rate in constitutive equation, because the stress components change if the body undergoes a rigid body rotation.

To account for rigid body rotation, several objective stress rates have been proposed in the past such as, among others, the Jaumann rate, Oldroyd rate, Truesdell rate, Green-Naghdi rate (Bruhns et al., 1999). The aforementioned rates cannot be exactly integrated for purely elastic deformation, i.e. $D_{ij} = D^{e}_{ij}$, and fail to represent any elastic behavior in the nonlinear range, resulting in the so-called oscillatory phenomenon and in dissipation of energy in a closed loading cycle (Bruhns et al., 1999, 2004).

The Truesdell rate, as instance, is related to the material derivative of the 2$^{\text{nd}}$ Piola-Kirchhoff stress. Following Crisfield (1997), considering the identity:

$$\boldsymbol{\tau} = J\boldsymbol{\sigma} = \mathbf{F}\,\mathbf{S}\,\mathbf{F}^{\mathsf{T}} \tag{2-52}$$

differentiation

$$\dot{\boldsymbol{\tau}} = \mathbf{F}\dot{\mathbf{S}}\mathbf{F}^{\mathsf{T}} + \dot{\mathbf{F}}\mathbf{S}\mathbf{F}^{\mathsf{T}} + \mathbf{F}\mathbf{S}\dot{\mathbf{F}}^{\mathsf{T}} \tag{2-53}$$

and fast substitution of $\mathbf{S} = \mathbf{F}^{-1}\,\boldsymbol{\tau}\,\mathbf{F}^{-\mathsf{T}}$ lead to:

$$\dot{\boldsymbol{\tau}} = \mathbf{F}\dot{\mathbf{S}}\mathbf{F}^{\mathsf{T}} + \dot{\mathbf{F}}\mathbf{F}^{-1}\boldsymbol{\tau} + \boldsymbol{\tau}\mathbf{F}^{-\mathsf{T}}\dot{\mathbf{F}}^{\mathsf{T}} \tag{2-54}$$

recalling the definition of velocity gradient $\mathbf{L} = \dot{\mathbf{F}}\mathbf{F}^{-1}$ (Eq. 2-9), the relationship can be reexpressed as:

$$\dot{\boldsymbol{\tau}} = \mathbf{F}\dot{\mathbf{S}}\mathbf{F}^{\mathsf{T}} + \mathbf{L}\boldsymbol{\tau} + \boldsymbol{\tau}\mathbf{L}^{\mathsf{T}} = \mathbf{F}(\bar{\mathbf{C}}\dot{\mathbf{E}})\mathbf{F}^{\mathsf{T}} + \mathbf{L}\boldsymbol{\tau} + \boldsymbol{\tau}\mathbf{L}^{\mathsf{T}} \tag{2-55}$$

where $\mathbf{F}\dot{\mathbf{S}}\mathbf{F}^{\mathsf{T}} = \overset{\triangledown}{\tau}_{ij}$ is the Truesdell rate of Kirchhoff stress and may be viewed as the Lie derivative of Kirchhoff stress (Simo and Hughes, 1998); and $\bar{\mathbf{C}}$ is the tangent constitutive matrix to use with the 2nd Piola-Kirchhoff stress rate $\dot{\mathbf{S}}$ (that is *per se* objective) and the Green-Lagrange strain rate $\dot{\mathbf{E}}$. The conclusion is that a constitutive model formulated in terms of the Truesdell rate of Kirchhoff stress $\overset{\triangledown}{\tau}_{ij}$ and the rate of deformation tensor D_{rs} is completely equivalent to a formulation in terms of the 2nd Piola-Kirchhoff stress rate $\dot{S}_{ab}$ and the Green-Lagrange strain rate $\dot{E}_{cd}$, as long as:

$${}_{t}C_{ijrs} = F_{ia}\,F_{jb}\,F_{rc}\,F_{sd}\,{}_{t}\bar{C}_{abcd} \tag{2-56}$$

Obviously, when the strains are small, the two tangent stress-strain matrices are practically equivalent because the gradient of the deformation is approximately $\mathbf{F} \approx \mathbf{I}$. However, when the strains are large, they differ.

Perić (1992) pointed out that the Jaumann rate of Kirchhoff stress approximates within the second order the Green-Nagdhi rate of Kirchhoff with relative error less than 1% as long as the ratios of principal stretches is within $0.80 \leq \lambda_{(j)}/\lambda_{(i)} = 1.20$.

(iii) Use the updated lagrangian formulation:

$${}_{t}\Delta S_{ij} = {}_{t}\bar{C}_{ijhk}\,{}_{t}\Delta E_{hk} \tag{2-57}$$

where ${}_{t}\Delta S_{ij}$ are the Cartesian components of the 2nd Piola-Kirchhoff stress (Truesdell increments) and ${}_{t}\bar{C}_{ijhk}$ is the constitutive tensor. Both are referred to previous configuration. According to Bathe et al. (1975), the incremental stress decomposition used in the U.L. formulation is:

$${}^{t+\Delta t}_{t}S_{ij} = {}^{t}\sigma_{ij} + {}_{t}\Delta S_{ij} \tag{2-58}$$

(iv) Use the updated Hencky formulation (de Souza Neto et al., 2009; de Borst et al., 2012): Assuming the existence of the strain energy function in terms of logarithmic strain measure, the constitutive equation for hyperelastic material takes the form:

$$ {}^{t}\tau_{ij} = \rho_0 \frac{\partial \Psi^e}{\partial \epsilon^e_{ij}} \tag{2-59} $$

where τ_{ij} are the Kirchhoff stresses, which are conjugate to the logarithmic strains for an isotropic material:

$$ \ln \mathbf{V} = \ln \mathbf{V}^e + \phi^e_f \ln \mathbf{V}^p \tag{2-60} $$

where $\phi^e_f \ln \mathbf{V}^p$ is the *push-forward* of the plastic strain over the elastic deformation. Under these assumptions, the principal axes of the Kirchhoff stress tensor coincide with the principal axes of deformation. The result is a return mapping algorithm constructed in the spatial configuration that preserve the format of infinitesimal theory. The flow rule is pulled-back to the intermediate configuration and then exponentially integrated:

$$ \mathbf{F}^p_{n+1} = \exp[\Delta\lambda\, \mathbf{R}^{e\,\mathsf{T}}_{n+1} \frac{\partial G}{\partial \boldsymbol{\tau}}^{n+1} \mathbf{R}^e_{n+1}]\mathbf{F}^p_n \tag{2-61} $$

(v) Use the co-rotational Kirchhoff stress formulation (Eterovic and Bathe, 1990; Weber and Anand, 1990; de Souza Neto and Perić, 1996; Bathe, 2006):

$$ \hat{\boldsymbol{\tau}} = \mathbf{R}^{e\,\mathsf{T}} J \boldsymbol{\sigma} \mathbf{R}^e \tag{2-62} $$

Regarding the stress conjugate to logarithmic strain rate $(\dot{\ln \mathbf{U}})$, the rotated Kirchhoff stress $\hat{\boldsymbol{\tau}}$ represents a good approximation, that is exact for an isotropic response. Crisfield (1997)[Sec.10.8] shows that if a similar procedure is applied to $J\boldsymbol{\sigma} = \mathbf{R}\hat{\boldsymbol{\tau}}\mathbf{R}^\mathsf{T}$, as it was done with $\boldsymbol{\tau} = \mathbf{F}\mathbf{S}\mathbf{F}^\mathsf{T}$, it is obtained:

$$ (\dot{J\boldsymbol{\sigma}}) = \mathbf{R}\dot{\hat{\boldsymbol{\tau}}}\mathbf{R}^\mathsf{T} + \dot{\mathbf{R}}\hat{\boldsymbol{\tau}}\mathbf{R}^\mathsf{T} + \mathbf{R}\hat{\boldsymbol{\tau}}\dot{\mathbf{R}}^\mathsf{T} = \overset{\circ}{\boldsymbol{\tau}}_{\mathsf{GN}} + \boldsymbol{\Omega}\boldsymbol{\tau} - \boldsymbol{\tau}\boldsymbol{\Omega} \tag{2-63} $$

where $\boldsymbol{\Omega} = \dot{\mathbf{R}}\mathbf{R}^\mathsf{T}$ suggests the use of Green-Naghdi rate of the Kirchhoff stress. Logarithmic strains - and their objective rates - are additive:

$$ \phi^e_b \ln \mathbf{V} = \ln \mathbf{U}^e + \ln \mathbf{V}^p \tag{2-64} $$

where $\phi^e_b \ln \mathbf{V}$ stands for the *pull-back* of the total eulerian logarithmic strain obtained by purging the rotation alone. As usual, a backward exponential integrator is employed to update the intermediate configuration:

$$ \mathbf{F}^p_{n+1} = \exp\left[\Delta\lambda \frac{\partial g}{\partial \hat{\boldsymbol{\tau}}}^{n+1}\right]\mathbf{F}^p_n \tag{2-65} $$

3
Constitutive modeling

3.1
Modeling the mechanical and chemical degradation

Experimental observations (Leroueil and Vaughan, 1990) have shown that the behavior of structured materials falls in between soil and rock mechanics. Bonding can have both geological or artificial origin (ex. grouted sands). Main features of these materials are (Gens and Nova, 1993):

- tensile strength and real cohesion provided by bonding;
- structure is responsible for increasing the compressive strength by an amount somewhat proportional to the tensile strength;
- after yielding, bond degradation occurs in a gradual manner;
- gradual transition from brittle/dilatant to ductile/compressive behavior as confining stress increases;
- after a marked yield, virgin compression line tends to converge towards the curve for the unbonded material.

The fundamental hypothesis to model the behavior of structured soils and weak rocks is to make the yield surface dependent on a set of constitutive parameters intended to represent the degree of bonding between solid particles. In this sense, as shown in Figure 3.1, structure is responsible for enlarging the yield locus (Gens and Nova, 1993), increasing the conventional preconsolidation pressure, $p_0 = p_t + p_s + p_c$, resulting from the sum of three contributions: tensile, compressive and intrinsic soil properties. In addition, its evolution is assumed to vary with mechanical degradation (i.e. crushing) or chemical weathering, according to a hardening rule and a disintegration law, each of them describing how the yield surface changes the size in the (q, p) plane.

A particular choice is made when compressive and tensile strength are set proportional to each other, by assuming $p_m = \alpha p_t$, with α a constant usually between 10 and 20 (Nova, 2005). In this case, it is postulated that the size of the yield function is controlled only by two variables, p_s and p_t, whose evolution is assumed to depend on plastic strains and degree of chemical weathering (Castellanza and Nova, 2004):

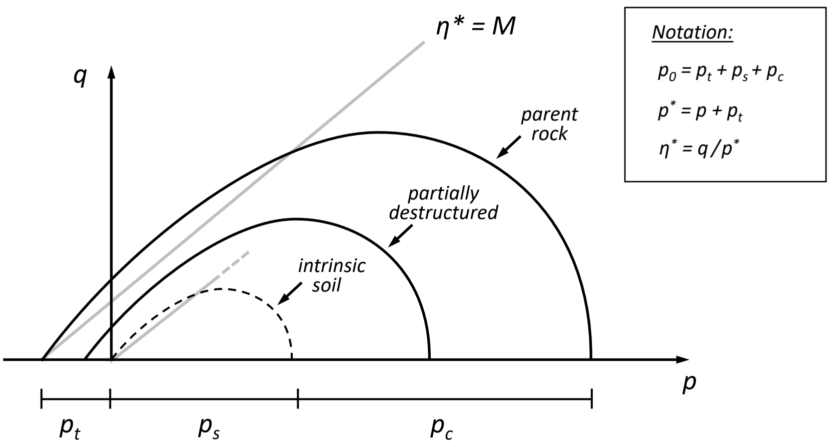

Figure 3.1: Evolution of yield surface during destructuration. After Nova et al. (2003).

$$f = f\Big(\sigma_{ij}, p_s(\epsilon^p_{hk}), p_t(\epsilon^p_{lm}, \chi)\Big) = 0 \tag{3-1}$$

where:

$p_s =$ internal variable related to soil hardening. It acts as common strain hardening parameter for the intrinsic soil matrix and is affected only by plastic strain history (ϵ^p_{hk}).

$p_t =$ internal variable related to the interparticle bonds and cementation, suffering mechanical damage and chemical weathering from combined physical actions (ϵ^p_{lm}) and chemical agents (χ)).

The consistency rule states that plastic strain may occur when $f = 0$, that in differential form becomes:

$$df = \frac{\partial f}{\partial \sigma_{ij}} d\sigma_{ij} + \frac{\partial f}{\partial p_s} dp_s + \frac{\partial f}{\partial p_t} dp_t = 0 \tag{3-2}$$

The *hardening rule* states the relation between p_s and plastic strains:

$$dp_s = \frac{\partial p_s}{\partial \epsilon^p_{hk}} d\epsilon^p_{hk} \tag{3-3}$$

while the *disintegration law* sets the consequences of mechanical damage and chemical weathering on interparticle bonds:

$$dp_t = \frac{\partial p_t}{\partial \epsilon^p_{lm}} d\epsilon^p_{lm} + \frac{\partial p_t}{\partial \chi} d\chi \tag{3-4}$$

where ϵ^p_{lm} are suitable destructuring plastic strains and χ is the degree of chemical weathering, a scalar varying between 0 and 1, that maps the transition from hard rock ($\chi = 0$) to totally weathered soil ($\chi = 1$).

Plastic strain increments are derived from plastic potential according to the flow rule:

$$d\epsilon^p_{rs} = \lambda \frac{\partial g}{\partial \sigma_{rs}} \tag{3-5}$$

combining all the previous equations, it is possible to calculate the plastic multiplier:

$$\lambda = -\frac{\dfrac{\partial f}{\partial \sigma_{ij}} d\sigma_{ij} + \dfrac{\partial f}{\partial p_t}\dfrac{\partial p_t}{\partial \chi} d\chi}{\dfrac{\partial f}{\partial p_s}\dfrac{\partial p_s}{\partial \epsilon^p_{hk}}\dfrac{\partial g}{\partial \sigma_{hk}} + \dfrac{\partial f}{\partial p_t}\dfrac{\partial p_t}{\partial \epsilon^p_{lm}}\dfrac{\partial g}{\partial \sigma_{lm}}} \tag{3-6}$$

and the hardening modulus:

$$H = H_s + H_t = -\frac{\partial f}{\partial p_s}\frac{\partial p_s}{\partial \epsilon^p_{hk}}\frac{\partial g}{\partial \sigma_{hk}} - \frac{\partial f}{\partial p_t}\frac{\partial p_t}{\partial \epsilon^p_{lm}}\frac{\partial g}{\partial \sigma_{lm}} \tag{3-7}$$

The hardening modulus consists of two competing terms expanding or shrinking the elastic domain (Gens and Nova, 1993). The former is related to the intrinsic soil behavior, the latter to the interparticle bonds.

The fundamental concepts stated above, related to the modeling of structured soils, require the choice of mathematical expressions for each of the following aspects.

3.1.1
Yield function

Experimental observations have shown that, at a first approximation, the yield surface is shaped like a teardrop, centered along the hydrostatic axis. A review of mathematical expressions from literature (they are resumed in Table 3.2 and Figure 3.8) reflects that the final shape of the yield function depends on three criteria: (1) the failure associated to shear (2) the moving cap due to compression (3) the eventual cohesion.

The previous considerations can be generalized by assuming a family of yield surfaces given by the expression:

$$\left(\frac{p^*}{p_0}\right)^n + \left(\frac{\eta^*}{\eta_0}\right)^\alpha = 1 \tag{3-8}$$

where p_0 is the preconsolidation pressure and η_0 the maximum stress ratio, i.e. the slope of the curve at the origin; n and α are model parameters that control the shape of the curve in stress space. Stress invariants are normalized by their respective maximum (or reference) values. The ratios p^*/p_0 and η^*/η_0 may be defined as the *normalized mean stress* and the *normalized stress ratio*, respectively. Equation 3-8 states that yielding will occur when the sum of powers of normalized stresses is equal to 1. The yield function in the (p, q) space is shown in Figure 3.2. By selecting appropriate parameters in Equation 3-8, one can mimic the yield function of other literature models, as shown in Table 3.1.

For the proposed general yield function, the following stress–dilatancy relation holds:

$$d = (n+\alpha)\,\frac{m^\alpha - \eta^\alpha}{\alpha\eta^{\alpha-1}} \tag{3-9}$$

where m is the stress-ratio at peak deviator stress, given by the following identity:

$$\eta_0^\alpha = m^\alpha\,\frac{n+\alpha}{n} \tag{3-10}$$

It is worth noting that m and η_0^α are real numbers, while η_0 may not. This aspect must be taken into account in numerical implementation to avoid undesirable instabilities.

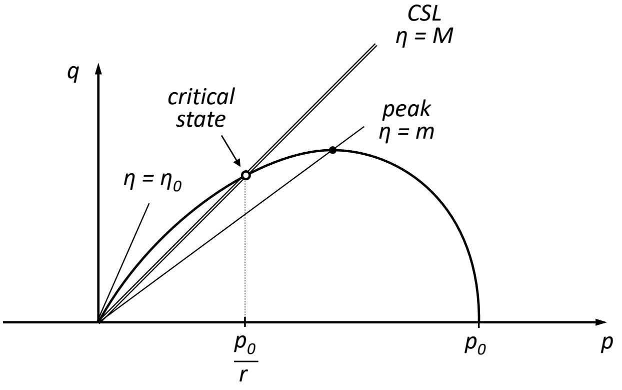

Figure 3.2: Definition of yield function parameters for the general case.

Furthermore, as pointed out by Yu (1998), the critical state may not coincide with peak deviatoric stress. Under this assumption, the intersection of the critical state line with the yield surface can be arbitrarily set by means of a fixed *spacing ratio*, $r = p_0/p_{cs}$, as shown in Figure 3.2. Then, the following relations hold:

$$\eta_0^\alpha = \frac{M^\alpha}{1-(\frac{1}{r})^n} \quad \text{or} \quad r = \left[1 - \frac{M^\alpha}{\eta_0^\alpha}\right]^{-1/n} \tag{3-11}$$

$$n = -\frac{\ln[1 - M^\alpha/\eta_0^\alpha]}{\ln r} \tag{3-12}$$

Therefore, partial derivatives can be written as:

$$\frac{\partial f}{\partial p} = \frac{n}{p}\left[1 - \left(\frac{\eta}{m}\right)^\alpha\right] \tag{3-13}$$

$$\frac{\partial f}{\partial q} = \frac{\alpha}{p}\,\frac{\eta^{\alpha-1}}{\eta_0^\alpha} \tag{3-14}$$

$$\frac{\partial f}{\partial p_0} = -\frac{n}{p_0}\left(\frac{p}{p_0}\right)^n = -\frac{n}{p}\left[1 - \left(\frac{\eta}{\eta_0}\right)^\alpha\right]^{1+1/n} \tag{3-15}$$

In three dimensional stress space it follows immediately (Van Eekelen, 1980):

$$\left(\frac{p}{p_0}\right)^n + \left(\frac{\eta}{\eta_0}\right)^\alpha \left(\frac{1+B\sin 3\theta}{1-B}\right)^{\alpha/4} = 1$$

with the following partial derivatives

$$\frac{\partial f}{\partial p} = \frac{n}{p}\left[1 - \left(\frac{\eta}{m}\right)^\alpha \left(\frac{1+B\sin 3\theta}{1-B}\right)^{\alpha/4}\right] \tag{3-16}$$

$$\frac{\partial f}{\partial q} = \frac{\alpha}{p}\,\frac{\eta^{\alpha-1}}{\eta_0^\alpha}\left(\frac{1+B\sin 3\theta}{1-B}\right)^{\alpha/4} \tag{3-17}$$

$$\frac{\partial f}{\partial \theta} = \frac{\alpha}{4}\left(\frac{\eta}{\eta_0}\right)^\alpha \frac{3B\cos 3\theta}{1+B\sin 3\theta}\left(\frac{1+B\sin 3\theta}{1-B}\right)^{\alpha/4} \tag{3-18}$$

$$\frac{\partial f}{\partial p_0} = -\frac{n}{p}\left[1 - \left(\frac{\eta}{\eta_0}\right)^\alpha \left(\frac{1+B\sin 3\theta}{1-B}\right)^{\alpha/4}\right]^{1+1/n} \tag{3-19}$$

3.1.2
Plastic potential

Following Lagioia et al. (1996), the mathematical expression of the plastic potential can be derived from a suitable stress-dilatancy relationship:

$$d = \frac{d\epsilon_p^p}{d\epsilon_q^p} = -\frac{dq}{dp} \tag{3-20}$$

by substitution into (Desai and Siriwardane, 1984)[Chap. 11, p. 290]:

$$\frac{dp}{p} = -\frac{d\eta}{d+\eta} \tag{3-21}$$

Two suitable stress-dilatancy relations may serve for the purpose of establishing the plastic potential for the structured soil model. The first is a slight modification of Nakai and Hinokio (2004) expression:

$$d = \alpha\frac{M^\beta - \eta^\beta}{\beta\eta^{\beta-1}} \tag{3-22}$$

The second has been inspired by Kim and Lade (1988):

$$d = \frac{(M^2-\eta^2)(\eta^2+\psi)}{\beta\eta} \tag{3-23}$$

The plastic potential adopted in this study is the hybrid resulting from combining the above two expressions. It is reported with other models from literature in Table 3.4. In the triaxial plane (p, q), the general expression is:

$$\left(\frac{\psi_1+\eta^\beta}{\psi_2-\eta^\beta}\right)\left(\frac{p}{p_0}\right)^\mu = \frac{\psi_1}{\psi_2} \tag{3-24}$$

Table 3.1: Parameters in Eq. (3-8) to represent models from literature.

Name	Yield Function	Parameters in Eq. (3-8)				
		α	n	η_0^α	r	m
Original Cam Clay	$\frac{\eta}{M} + \ln\frac{p}{p_0} = 0$	1	10^{-6}	Eq. (3-10)	Eq. (3-11.b)	M
Modified Cam Clay	$\left(\frac{\eta}{M}\right)^2 + 1 - \frac{p_0}{p} = 0$	2	-1	Eq. (3-10)	Eq. (3-11.b)	M
Tear Shape (*)	$\frac{p}{p_0} - e^{-\frac{\eta/M}{1-\alpha}}\left(\frac{1-\alpha}{\alpha}\frac{\eta}{M} + 1\right)^{\alpha/(1-\alpha)^2} = 0$	$1/\ln r$	10^{-6}	Eq. (3-10)	$e^{\frac{1}{1-\alpha}}\alpha^{\alpha/(1-\alpha)^2}$	M
CASM (**)	$\left(\frac{\eta}{M}\right)^n = -\frac{\ln(p/p_0)}{\ln r}$	n	10^{-6}	Eq. (3-11.a)	r	Eq. (3-10)
R-Soil	$\left(\frac{p}{p_0}\right)^n + \left(\frac{\eta}{3}\right)^2 = 1$	2	Eq. (3-12)	3^α	r	Eq. (3-10)

(*) Lagioia et al. (1996), Case 2, $\mu = 1$
(**) Yu (1998)

Table 3.2: Yield functions from literature.

Name	Yield function
Original Cam Clay	$\frac{\eta}{M} + \ln\frac{p}{p_0} = 0$
Modified Cam Clay	$\left(\frac{\eta}{M}\right)^2 + 1 - \frac{p_0}{p} = 0$
CASM	$\left(\frac{\eta}{M}\right)^n = -\frac{\ln(p/p_0)}{\ln r}$
Single Hardening (*)	$f_p = \left(\psi_1\frac{I_1^3}{I_3} - \frac{I_1^2}{I_2}\right)\left(\frac{I_1}{p_a}\right)^h e^q$
Sinfonietta Classica (**)	$9(\gamma - 3)\ln\frac{p}{p_0} - \gamma J_{3\eta} + \frac{9}{4}(\gamma - 1)J_{2\eta} = 0$
Tear Shape	$\frac{p}{p_0} - e^{-\frac{\eta/M}{1-\alpha}}\left(\frac{1-\alpha}{\alpha}\frac{\eta}{M} + 1\right)^{\alpha/(1-\alpha)^2} = 0$
Present study (1)	$\left(\frac{p}{p_0}\right)^n + \left(\frac{\eta}{\eta_0}\right)^\alpha = 1$

(*) Lade (1990)
(**) Lagioia and Nova (1995)

where $(\beta, \psi_1, \psi_2, \mu)$ are parameters of the model. With the above plastic potential, it is possible to derive the following stress-dilatancy relation:

$$d = \frac{d\epsilon_p^{\mathrm{p}}}{d\epsilon_q^{\mathrm{p}}} = \alpha\frac{(M^\beta - \eta^\beta)(\eta^\beta + \psi)}{\beta\eta^{\beta-1}} \tag{3-25}$$

in which the following identities have been introduced:

$$\psi_1 = \frac{1}{2}\left[\sqrt{(M^\beta + \beta/\alpha - \psi)^2 + 4M^\beta\psi} - (M^\beta + \beta/\alpha - \psi)\right] \tag{3-26}$$

$$\psi_2 = M^\beta + \beta/\alpha - \psi + \psi_1 \tag{3-27}$$

$$\mu = \alpha(\psi_1 + \psi_2) \tag{3-28}$$

The input parameters are (α, β, M, ψ), while (ψ_1, ψ_2, μ) are derived. Eventually, imposing the tension cut-off condition, $d(\eta = 3) = -3$, the input parameters for the plastic potential may be reduced from four to three, since α is given by:

$$\alpha = \frac{\beta 3^\beta}{(3^\beta - M^\beta)(3^\beta + \psi)} \tag{3-29}$$

Table 3.3 lists specific combinations of parameters (α, β, M, ψ) that allow to reproduce different literature models from the general expression given in

Equation 3-25. Resulting plots are shown hereafter.

a) Original Cam Clay

Adopt $\beta = 1$ and $\psi = \frac{1}{\alpha} = 10^6$

The stress-dilatancy relation is that of Original Cam Clay: $d = M - \eta$

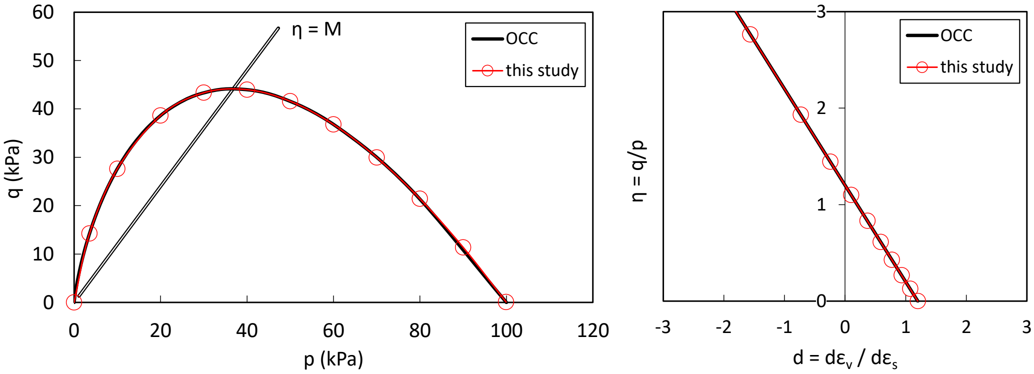

Figure 3.3: Comparison with Original Cam Clay ($M = 1.2$, $p_0 = 100\,\mathrm{kPa}$).

b) Modified Cam Clay

Adopt $\beta = 2$ and $\psi = \frac{1}{\alpha} = 10^6$

The stress-dilatancy relation is that of Modified Cam Clay: $d = \frac{M^2 - \eta^2}{2\eta}$

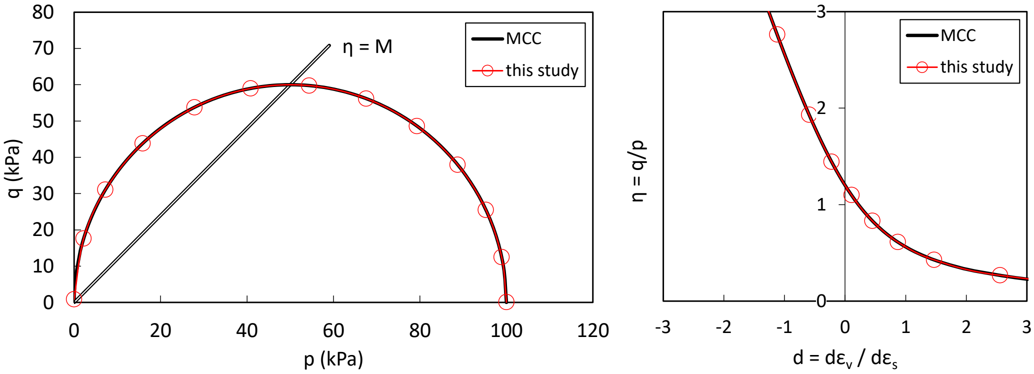

Figure 3.4: Comparison with Modified Cam Clay ($M = 1.2$, $p_0 = 100\,\mathrm{kPa}$).

c) Rowe stress-dilatancy (CASM)

Adopt $\beta = 1$ and $\alpha = \frac{3}{(3-M)(3+\psi)}$

The stress-dilatancy relation becomes: $d = \alpha(M - \eta)(\eta + \psi)$

Table 3.3: Parameters in Eq. (3-24) to represent models from literature.

Name	Plastic Potential	Parameters in Eq. (3-24)			
		α	β	M	ψ
Original Cam Clay	$\frac{\eta}{M} + \ln \frac{p}{p_0} = 0$	10^{-6}	1	M	10^6
Modified Cam Clay	$\left(\frac{\eta}{M}\right)^2 + 1 - \frac{p_0}{p} = 0$	10^{-6}	2	M	10^6
Rowe-CASM (*)	$d = \frac{9(M-\eta)}{9+3M-2M\eta}$	Eq. (3-29)	1	M	$6.4 - 3.6M$
Single Hardening (**)	$g_p = \left(\psi_1 \frac{I_1^3}{I_3} - \frac{I_1^2}{I_2} + \psi_2\right)\left(\frac{I_1}{p_a}\right)^{\mu}$	Eq. (3-29)	2	(***)	$-\frac{81(27\psi_1+\psi_2+3)}{M^2\,\psi_2}$
R-Soil	$\left(\frac{\psi_1+\eta^2}{\psi_2-\eta^2}\right)\left(\frac{p}{p_0}\right)^{\mu} = \frac{\psi_1}{\psi_2}$	Eq. (3-29)	2	M	ψ

(*) Stress-dilatancy relation from Yu (1998). Not suitable for $M > 1.4$.
(**) Kim and Lade (1988)
(***) obtain M imposing $d(\eta = M) = 0$ in stress-dilatancy relation.

Table 3.4: Plastic potentials and related stress-dilatancy relations.

Name	Plastic potential	Stress-dilatancy relation
Original Cam Clay	$\frac{\eta}{M} + \ln\frac{p}{p_0} = 0$	$d = M - \eta$
Modified Cam Clay	$\left(\frac{\eta}{M}\right)^2 + 1 - \frac{p_0}{p} = 0$	$d = \frac{M^2 - \eta^2}{2\eta}$
CASM	$3M\ \ln\frac{p}{\beta} + (3+2M)\ln\left(\frac{2q}{p} + 3\right) - (3-M)\ln\left(3 - \frac{q}{p}\right) = 0$	$d = \frac{9(M-\eta)}{9+3M-2M\eta}$
Single Hardening	$g_p = \left(\psi_1\frac{I_1^3}{I_3} - \frac{I_1^2}{I_2} + \psi_2\right)\left(\frac{I_1}{p_a}\right)^\mu$	$d^* = \frac{3}{2q}\frac{3\frac{\partial g}{\partial I_1} - 6p\frac{\partial g}{\partial I_2} - I_2\frac{\partial g}{\partial I_3}}{\frac{\partial g}{\partial I_2} - (p - \frac{1}{3}q)\frac{\partial g}{\partial I_3}}$
Sinfonietta Classica	$3\beta(\gamma-3)\ln\frac{p}{p_0} - \gamma J_{3\eta} + \frac{9}{4}(\gamma-1)J_{2\eta} = 0$	$d^* = \frac{9(\gamma-3)}{-\frac{2}{9}\gamma\eta^2 + \frac{3}{2}(\gamma-1)\eta} - \eta$
Tear Shape	$\frac{p}{p_0} - e^{-\frac{\eta/M}{1-\alpha}}\left(\frac{1-\alpha}{\alpha}\frac{\eta}{M} + 1\right)^{\alpha/(1-\alpha)^2} = 0$	$d = (M-\eta)\left(\frac{\alpha M}{\eta} + 1\right)$
Present study (2)	$g_p = \left(\frac{\psi_1 + \eta^\beta}{\psi_2 - \eta^\beta}\right)\left(\frac{p}{p_0}\right)^\mu$	$d = \alpha\frac{(M^\beta - \eta^\beta)(\eta^\beta + \psi)}{\beta\eta^{\beta-1}}$

* Valid under axisymmetric state of stress $\sigma_1 \neq \sigma_2 = \sigma_3$.

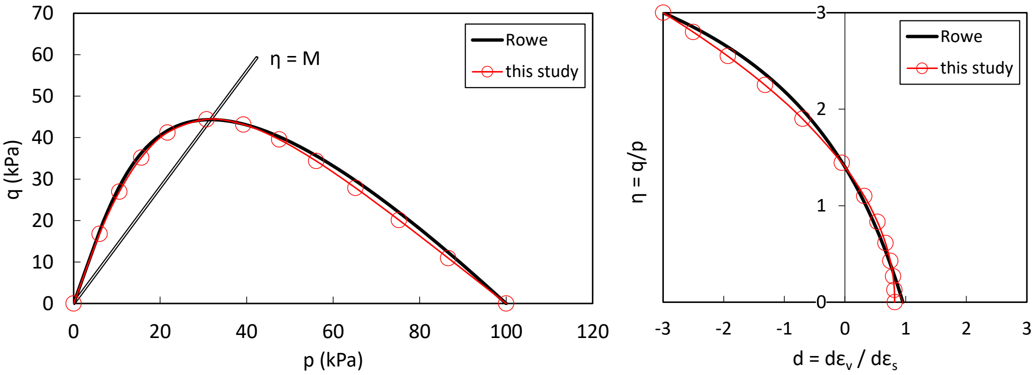

Figure 3.5: Comparison with Rowe's model, employed in CASM ($M = 1.2$, $p_0 = 100\,\text{kPa}, \psi = 2$).

d) Single Hardening (Lade-Kim)

Adopt $\beta = 2$ and $\alpha = \frac{18}{(9-M^2)(9+\psi)}$

The stress-dilatancy relation becomes: $d = \alpha\frac{(M^2-\eta^2)(\eta^2+\psi)}{2\eta}$

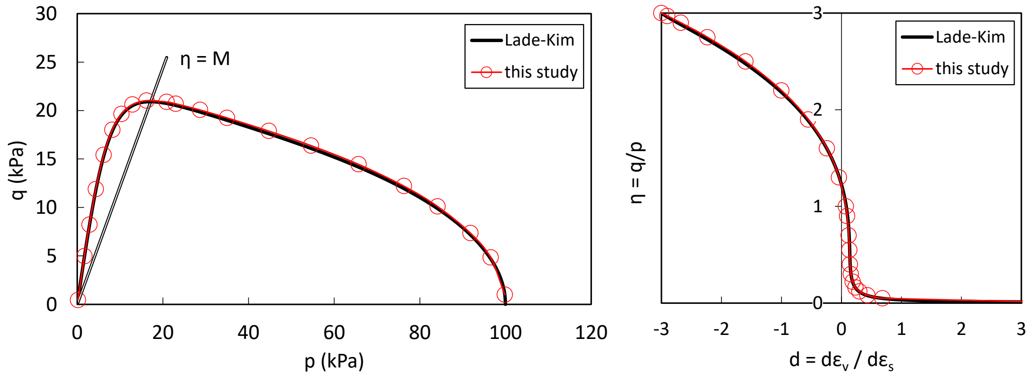

Figure 3.6: Comparison with Lade-Kim model ($M = 1.2$, $p_0 = 100\,\text{kPa}, \psi = 0.21$).

Table 3.5: Model parameters used in Single Hardening model.

Failure criterion	Yield Function	Plastic Potential
$\eta_1 = 48$	$p_0 = 100$ kPa	$\psi_1 = 0.00339$
$m = 0.54$	$h = 0.81$	$\psi_2 = -3.08$
$p_a = 100$	$\alpha = 0.5$	$\mu = 2.38$

e) Tear Shape (Lagioia et al., 1996)

Adopt $\psi = \frac{k}{\alpha} = 10^6$

The stress-dilatancy relation becomes: $d = k\frac{M^\beta-\eta^\beta}{\beta\eta^{\beta-1}}$

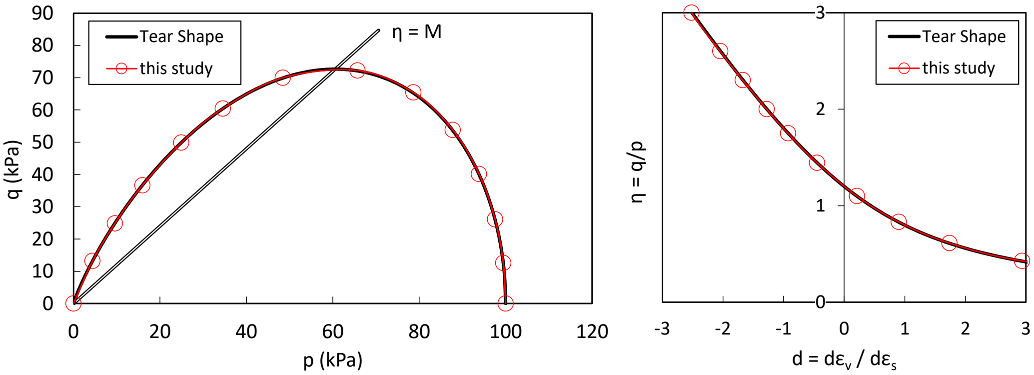

Figure 3.7: Comparison with Tear Shape model from Milan research group ($M = 1.2$, $p_0 = 100\,\text{kPa}, \beta = 2, k = 2$).

Table 3.6: Model parameters used in Tear Shape model.

Yield Function
$\alpha = 0.99$
$M = 1.2$
$p_0 = 100$ kPa

Finally, constitutive modeling is completed by considering the following remaining components:

Elastic constitutive relations. The behavior of soil is elastic within the yield surface. In general, isotropic hypoelasticity is chosen for the elastic stress-strain relationships. Some authors (Yu et al., 2007; Rios et al., 2016) have also made elastic stiffness dependent on bonding. A possible choice is:

$$K = \frac{p + p_t}{\kappa^*} = \frac{\dot{p}}{\dot{\epsilon}_v^e} \tag{3-30}$$

Hardening law. For soils and rocks, the law is generally assumed to be strain hardening, resulting from accumulated plastic strains.

Disintegration law. Destructuration is a chemo-mechanical-softening process. According to Koliji et al. (2008), mechanical degradation is controlled by a suitable *destructuring strain*, a general plastic strain that, depending on loading condition, can be volumetric, deviatoric or a combination of both. Disintegration of interparticle bonds by chemical degradation may be included in the formulation, as shown by Nova et al. (2003) and Castellanza and Nova (2004).

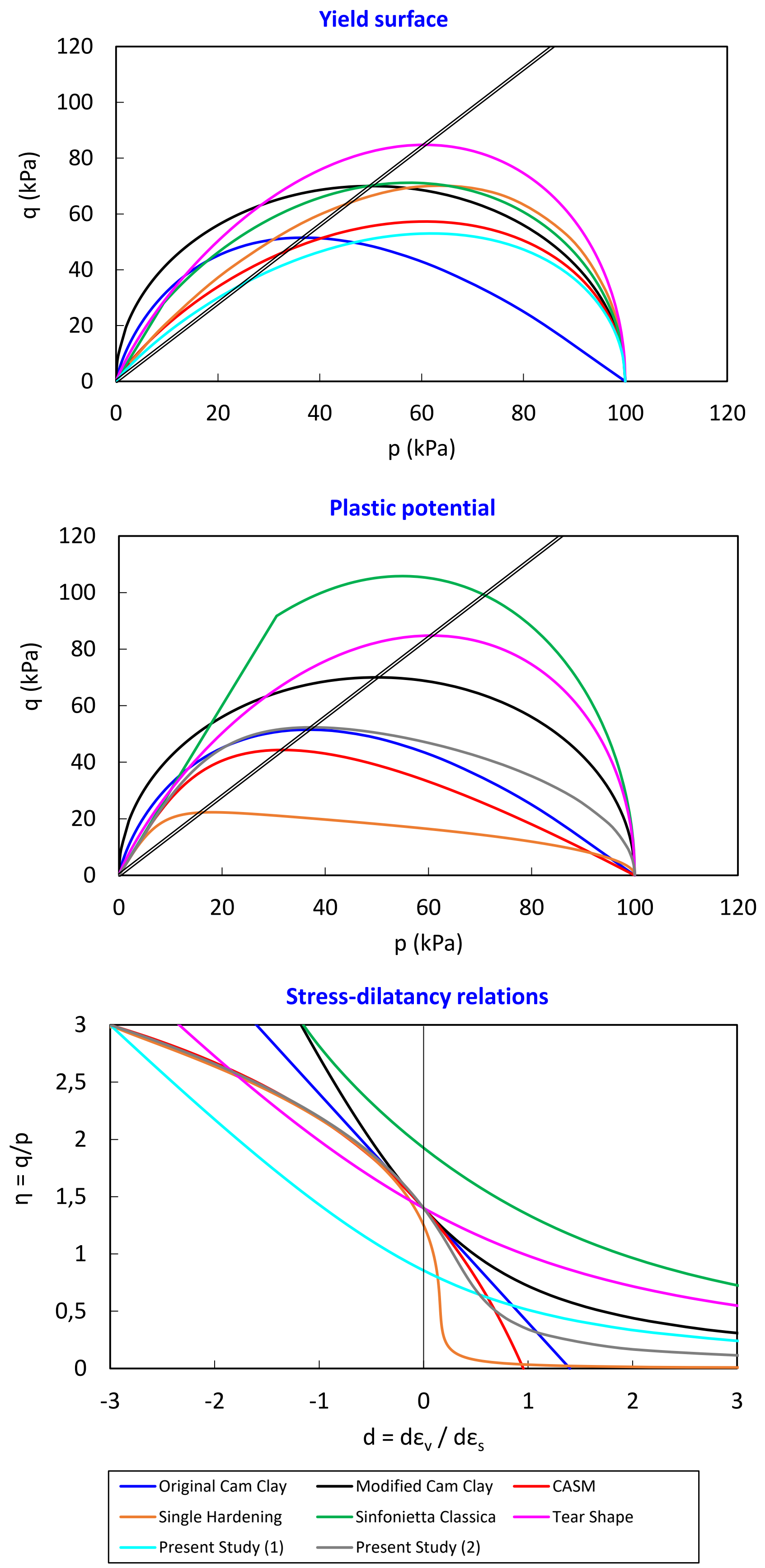

Figure 3.8: Comparison of yield surface, plastic potential and related stress-dilatancy curve from different constitutive models.

3.2
Viscoplasticity

This section presents the framework of elastic viscoplastic modelling proposed by Perzyna (1963, 1966). The theory has been extended to geologic materials by Adachi and Oka (1982); Borja and Kavazanjian (1985); Desai and Zhang (1987); Borja (1992); Kutter and Sathialingam (1992); Liang and Ma (1992); Rowe and Hinchberger (1998); Yin and Graham (1999); Hinchberger and Rowe (2005); Leoni et al. (2008) among others. Models haves been applied to both cohesive and granular materials to reproduce drained and undrained creep, stress relaxation and strain-rate effects on strength. Most of the applications aimed to reproduce phenomena of considerable interest in geomechanics, such as secondary compression (i.e. deformation under constant effective stress), influence of strain rate on undrained strength, constant rate of strain oedometer test, long-term deformations of foundations and excavations, creep behavior of rocks (Hickman and Gutierrez, 2007; Chang and Zoback, 2010) and salt rock, delayed failure of embankments built on soft soils, undrained triaxial stress relaxation, slow landslides and fast landslides of fluidized materials (Pastor et al., 2015).

Perzyna's theory is a straightforward extension of the classical rate-independent plasticity theory. It is assumed that the (total) strain rate can be decoupled into an elastic (recoverable) and a visco-plastic part:

$$\dot{\epsilon}_{ij} = \dot{\epsilon}^{e}_{ij} + \dot{\epsilon}^{vp}_{ij} \tag{3-31}$$

the viscoplastic part represents combined viscous and plastic effects. According to Zienkiewicz and Cormeau (1974), creep and plastic strains cannot be treated separately as only the combined effect is measurable and the idea of instantaneous permanent (plastic) strain is only a *convenient mathematical fiction.*

A static yield function defines the elastic domain, where the material has no viscous behavior, i.e. the viscoplastic strain rates vanish. However, this does not mean that all state variable rates are zero in the elastic region (Lubliner, 2008). The yield function has the form:

$$F(\sigma_{ij}, q_k) = \frac{\sigma_e}{\sigma_0} - 1 \tag{3-32}$$

where σ_e is the *equivalent stress* and σ_0 is the *reference stress*, which may be a hardening parameter. A special case is when the equivalent stress is a function of the state of stress only, i.e. $\sigma_e = f(\sigma_{ij})$.

Perzyna proposed the following viscoplastic strain rate in case of infinitesimal strain field:

Table 3.7: Viscous nucleus from literature. Modified from Yin et al. (2010).

No.	Type	$\phi(F)$	Reference
1	Expon 1	e^{bF}	di Prisco and Imposimato (1996)
2	Expon 2	$e^{bF}-1$	Fodil et al. (1997)
3	Power 1	F^N	Zienkiewicz and Cormeau (1974)
4	Power 2	$(F+1)^N$	Rowe and Hinchberger (1998)
5	Power 3	$(F+1)^N-1$	Perić (1993)

$$\dot{\epsilon}_{ij}^{vp} = \frac{1}{\mu} \langle \phi(F) \rangle \frac{\partial g}{\partial \sigma_{ij}} \tag{3-33}$$

where μ is a "fluidity parameter", that may vary with temperature, g is a plastic potential-like function defining the direction of inelastic flow and $\langle . \rangle$ is the Macauley bracket, defined such that:

$$\langle \phi \rangle = \begin{cases} 0, & \text{if } \phi \leq 0 \\ \phi, & \text{if } \phi > 0 \end{cases} \tag{3-34}$$

Equation 3-33 indicates that the rate in which inelastic deformation takes place increases with the distance from the yield surface. The function $\phi(F)$ is a positive monotonic increasing function (Owen and Hinton, 1980) whose mathematical form is chosen in the light of experimental data (Perzyna, 1966). It has been called by different names: viscous flow function (e.g., Katona, 1984), scaling function (e.g., Yin et al., 2010) and viscous nucleus (e.g., di Prisco and Imposimato, 1996). In this work, the term *viscous nucleus* will be preferably used to not cause confusion with the general concept of *flow rule*. Many mathematical expressions have been proposed in the literature. Some are summarized in Table 3.7. According to Owen and Hinton (1980), recommended forms for the viscous nucleus are:

$$\phi = F^N \tag{3-35}$$

$$\phi = e^{bF} - 1 \tag{3-36}$$

Finally, squaring both sides of Equation 3-33 and combining it with Equation 3-32, the following inverse relation is obtained:

$$\sigma_e = \sigma_0 \left[1 + \phi^{-1} \left(\mu \frac{(\dot{\epsilon}_{ij}^{vp} \dot{\epsilon}_{ij}^{vp})^{1/2}}{(\partial g / \partial \sigma_{ij} \cdot \partial g / \partial \sigma_{ij})^{1/2}} \right) \right] \tag{3-37}$$

the above expression implicitly represents the dynamic yield condition for rate-dependent viscoplastic materials, and describes the dependence of yield condition on the strain rate.

3.2.1
Undrained Hydrostatic Relaxation Test

Rate-dependent behavior may also appear in the form of stress relaxation, that is, a decrease in stress under constant level of strain. To investigate the viscous behavior of geomaterials, the tests that may be carried out are:

1. Monotonic loading at various strain rates
2. Monotonic loading at various effective stress rates
3. Creep test at constant effective stress
4. Stress relaxation at constant strain

In author's opinion, relaxation tests provide a better insight into the mechanisms that control the rate-dependent behavior than creep test, because they reflect in a clearer manner the characteristics of the viscous nucleus.

This section presents a new theoretical interpretation of the Undrained Hydrostatic Relaxation Test (HRU). The analysis is performed in the light of the classical theory of viscoplasticity of Perzyna (1963, 1966). The test provides a clear examination of the viscous properties of clays on the relaxation stage and allows a separate (subsequent) check on the secondary (creep) settlement measured in conventional oedometer tests.

The test is performed in the triaxial apparatus to investigate the undrained relaxation behavior of clay under a hydrostatic state of stress. Figure 3.9 shows a schematic of the experimental apparatus and the results of an idealized experiment. For the initial consolidation phase, a confining pressure is applied to the specimen that is allowed to drain. Once the consolidation is completed, the drainage is closed and the relaxation test is performed at constant cell pressure. Because water cannot escape from pores, the volume of the soil specimen does not change throughout the relaxation process. Instead, an excess pore water pressure develops.

Hypothesis In order to derive an analytical solution for the interpretation of this test, the following assumptions are introduced:

1. The specimen is consolidated under a uniform cell pressure, σ_c, that is kept constant during all stages. The specimen is therefore submitted to a hydrostatic state of stress. No shear stress exists.
2. The average mean effective stress, p', is the difference between cell pressure and pore pressure, $p' = \sigma_c - u$.

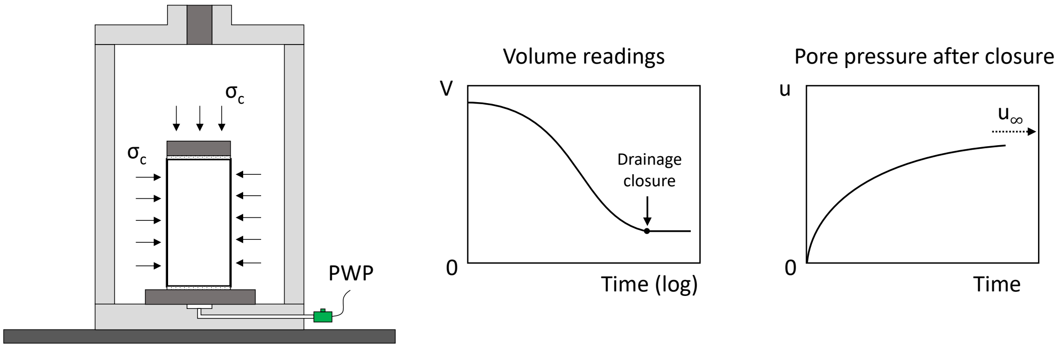

Figure 3.9: Undrained Hydrostatic Relaxation Test

3. The consolidation phase ends when the excess pore pressure is completely dissipated. This condition is usually referred as End of Primary (EOP) consolidation. The time required to achieve 100% degree of consolidation can be estimated according to Taylor's method.

4. Still after pore pressure dissipation, specimen continues to deform under constant effective stress essentially due to creep.

5. As drainage is closed, the total volumetric strain rate instantly drops to zero, i.e. $\dot{\epsilon}_v = 0$.

6. The total strain rate is assumed as the sum of the elastic and the viscoplastic parts. This means that during the relaxation process, the terms sum to zero.

7. Viscoplastic strain rate is calculated according to Perzyna's theory:

$$\dot{\epsilon}^p = \frac{1}{\mu}\,\phi(F) = \frac{1}{\mu}(e^{bF} - 1) \tag{3-38}$$

   where

   - $\mu = \mu(T)$ is a temperature-dependent fluidity parameter
   - b is a rate-sensitivity parameter

   and F is the "overstress" function, equal to the ratio between the mean effective stress and the preconsolidation pressure minus one:

$$F = \frac{p'}{p_y} - 1 \tag{3-39}$$

   The total viscoplastic strain is calculated by integrating the viscoplastic strain rate over time:

$$\epsilon^p = \int_0^t \dot{\epsilon}^p \, dt \tag{3-40}$$

   Obviously, time integration requires a numerical quadrature.

List of symbols For clarity, the following list of symbols is provided:

$\epsilon_v, \dot{\epsilon}_v$	Total volumetric strain and rate
$\epsilon^e, \dot{\epsilon}^e$	Elastic volumetric strain and rate
$\epsilon^p, \dot{\epsilon}^p$	Viscoplastic volumetric strain and rate
σ_c	Cell pressure
p'	Effective mean stress
u	Excess pore pressure
p_y	Yield stress (preconsolidation pressure)

Boundary conditions Assuming no overall volume change during relaxation, the elastic and plastic parts must sum to zero:

$$\epsilon_v = \epsilon^e + \epsilon^p = 0 \quad \text{and} \quad \dot{\epsilon}_v = \dot{\epsilon}^e + \dot{\epsilon}^p = 0 \tag{3-41}$$

The condition of no overall change in volume places no restriction on the individual components that make up that overall change. Elastic and plastic components exactly balance each other to give zero resultant total volumetric strain.

Cell pressure is kept constant: $\sigma_c = p' + u = \text{const}$, then $\dot{p}' = -\dot{u}$

Initial conditions According to the experimental procedure, the drainage is closed at 100% degree of consolidation. Thus, the initial conditions are well established:

$u(0) = 0$	Drainage is closed when pore pressure is completely dissipated
$p'(0) = \sigma_c$	From the definition of effective stress, at the beginning of the relaxation process the effective mean stress equals the total applied cell pressure

Final conditions (equilibrium) The excess pore pressure generated after drainage closure converges to an asymptotic value as time approaches infinity:

$$\lim_{t \to \infty} u(t) = u_\infty \tag{3-42}$$

Governing equations From hypothesis No.1, it follows that the point representing the state of stress moves solely along the hydrostatic axis. Then, the "overstress" is:

$$F = \frac{p'}{p_y} - 1 \tag{3-43}$$

Where $p' = \sigma_c - u$ is the mean effective stress and p_y is the yield stress (preconsolidation pressure).

From hypothesis No.5, it follows that the overall volume of the specimen does not change during the undrained relaxation:

$$\epsilon_v = 0 \quad \text{and} \quad \dot{\epsilon}_v = 0 \tag{3-44}$$

However, according to hypothesis No.6, no particular restriction is imposed on the elastic and/or plastic parts. Indeed:

$$\epsilon_v = \epsilon_v^e + \epsilon_v^p \quad \text{and} \quad \dot{\epsilon}_v = \quad \dot{\epsilon}_v^e + \quad \dot{\epsilon}_v^p \tag{3-45}$$

that yields $\epsilon_v^e = -\epsilon_v^p$ and $\dot{\epsilon}_v^e = -\dot{\epsilon}_v^p$.

After closing the drainage valve, the cell pressure in the triaxial chamber is held constant while the pore pressure is monitored. The following relations hold at any time:

$$\sigma_c = p' + u \quad \text{and} \quad \dot{p}' = -\dot{u} \tag{3-46}$$

This means that an increase of pore pressure corresponds to an equal decrease in mean effective stress. Therefore, the relaxation is an undrained (no overall volume change) unloading process at constant total stress ($\sigma_c = \text{const.}$).

The decrease in mean effective stress results in an elastic expansion such that:

$$\dot{\epsilon}^e = \kappa^* \frac{\dot{p}'}{p'} = -\kappa^* \frac{\dot{u}}{\sigma_c - u} \tag{3-47}$$

where, as usual in practice, the elastic volumetric strain has been related to the effective mean stress through a pressure-dependent bulk modulus $K' = p'/\kappa^*$.

Recalling hypothesis No.3, the above differential equation can be integrated over the interval $[0, t]$ to express the elastic volumetric strain as function of generated pore pressure:

$$\epsilon^e = \kappa^* \ln\left(1 - \frac{u}{\sigma_c}\right) \tag{3-48}$$

Obs: consider that $\epsilon^e(0) = 0$ and $u(0) = 0$. As expected, an elastic volumetric expansion occurs as a result of the reduction of mean effective stress. In contrast, the viscoplastic strain is positive, meaning that creep causes volume contraction. This occurs because elastic and viscoplastic strain rates are equal and opposite, as the drainage is closed, the rate of overall volume change is set to zero. The fundamental result is that elastic (and therefore viscoplastic) strains can be calculated by means of Equation 3-48 from the excess pore pressure monitored during the relaxation stage.

If the sample is allowed to "relax" for a very long time, the excess pore pressure generated after drainage closure will reach a steady state. This means that it converges to an asymptotic value as time approaches to infinity:

$$\lim_{t \to \infty} u(t) = u_\infty \tag{3-49}$$

$$\lim_{t\to\infty} \epsilon^e(t) = \epsilon^e_\infty = \kappa^* \ln\left(1 - \frac{u_\infty}{\sigma_c}\right) \tag{3-50}$$

and the condition

$$\lim_{t\to\infty} \dot{\epsilon}^e = 0 \tag{3-51}$$

is necessary because the steady state condition is reached when all the partial derivatives with respect to time becomes zero and remains so. As a consequence, the viscoplastic strain rate also becomes zero at a time equal to infinity and, in turn, the “overstress” is zero, too:

$$F_\infty = \frac{p'_\infty}{p_{y\infty}} - 1 = 0 \quad \rightarrow \quad p_{y\infty} = p'_\infty = \sigma_c - u_\infty \tag{3-52}$$

In other words, the yield stress becomes equal to the effective mean stress and the “overstress” is zero at the final stationary condition.

The preconsolidation pressure changes with viscoplastic volumetric strains according to the strain-hardening rule of Cam Clay models:

$$\frac{\dot{p}_y}{p_y} = \frac{\dot{\epsilon}^p}{\lambda^* - \kappa^*} \quad \rightarrow \quad p_y = p_{y0} \exp\left(\frac{\epsilon^p}{\lambda^* - \kappa^*}\right) \tag{3-53}$$

for $t \rightarrow \infty$ yields:

$$p_{y0} \exp\left[-\frac{\kappa^*}{\lambda^* - \kappa^*} \ln\left(1 - \frac{u_\infty}{\sigma_c}\right)\right] = \sigma_c - u_\infty \tag{3-54}$$

And after some manipulations, it results in the following:

$$p_{y0} = \sigma_c \left(1 - \frac{u_\infty}{\sigma_c}\right)^{1/\Lambda} \tag{3-55}$$

or, equivalently

$$u_\infty = \sigma_c \left[1 - \left(\frac{p_{y0}}{\sigma_c}\right)^{\Lambda}\right] \tag{3-56}$$

where $\Lambda = \frac{\lambda^* - \kappa^*}{\lambda^*}$. It follows that the value of the preconsolidation pressure at the beginning of the relaxation stage (p_{y0}) is directly related to the asymptotic value of the excess pore pressure (u_∞) at the final steady state. In other words, the final excess pore pressure depends solely on the "initial" condition that is imposed at the beginning of the relaxation stage. As a matter of fact, the magnitude and rate of excess pore pressure are larger for higher volumetric strain ($\dot{\epsilon}_v$) occurring when the drainage valve is closed.

If one knows p_{y0} or u_∞ , then the relaxation stage is fully described by the following governing equations:

$$\begin{aligned} &\epsilon^e + \epsilon^p = 0 && \sigma_c = p' + u \\ &\epsilon^e = \kappa^* \ln\left(1 - \frac{u}{\sigma_c}\right) && p_y = p_{y0} e^{\epsilon^p/(\lambda^* - \kappa^*)} \end{aligned} \tag{3-57}$$

Calibration via least-square method Given the set of observations $\epsilon^e_0, \epsilon^e_1, ..., \epsilon^e_n$ made at times $t_0, t_1, ..., t_n$, the viscoplastic model parameters

(μ, b) are calibrated from experimental data via a least-square minimization procedure.

Model predictions

$$y_i^c = \epsilon_i^p = \int_0^{t_i} \dot{\epsilon}^p \, dt \tag{3-58}$$

are fitted to the experimental data $y_i^e = -\epsilon_i^e$ via the following numerical procedure:

Residual vector $r_i = y_i^c - y_i^e$
Fitting parameters $\alpha_j = \{\mu, b\}$
Jacobian matrix $J_{ij} = \frac{\partial y_i^c}{\partial \alpha_j}$
$\frac{\partial \epsilon_i^p}{\partial \mu} = \frac{\partial}{\partial \mu} \int_0^{t_i} \frac{1}{\mu}(e^{bF} - 1)dt = -\frac{1}{\mu}\epsilon_i^p$
$\frac{\partial \epsilon_i^p}{\partial b} = \frac{\partial}{\partial b} \int_0^{t_i} \frac{1}{\mu}(e^{bF} - 1)dt = \frac{1}{\mu} \int_0^{t_i} F(1+\phi)dt$

Algorithm 1 Least-square procedure for calibration of model parameters

```
Set $k = 1$
Use a set of physical admissible parameters as a guess $\alpha_j^*$
    $\alpha_j^{(k)} \leftarrow \alpha_j^*$
Do for $k$=1, nitMax
    1. Calculate $y_i^c$ and the residual vector $r_i = y_i^c - y_i^c$
    2. Compute the Jacobian matrix
        $J_{ij} = \frac{\partial y_i^c(\alpha^{(k)})}{\partial \alpha_j}$
    3. Solve
        $\boldsymbol{\Delta}\alpha = -(\mathbf{J^T J})^{-1}\, \mathbf{J^T}(\mathbf{y^c} - \mathbf{y^e})$
    4. Update model parameters
        $\alpha^{new} = \alpha^{old} + \Delta\alpha$
        $k = k + 1$
    5. Compute the error
        $error = \frac{\|\mathbf{y^c} - \mathbf{y^e}\|}{\|y^e\|}$
    6. Check if the error is below a given tolerance. If so, return the calibrated parameters.
```

3.3
Summary

This chapter dealt with the mathematical formulation of material behavior by means of the constitutive relations. After an initial review of several literature elastoplastic models, new expressions of the yield function and plastic potential were derived. Those expressions are very general and can mimic a number of existing constitutive models. They were formulated using the triaxial invariants (p, q), which brought several advantages in the mathematical derivations and graphical representations.

The elastoplastic framework to model bonded geomaterials was reviewed. The conceptual basis presented by Gens and Nova (1993) was recalled along with the upgrade proposed by Nova et al. (2003) to introduce chemical weathering effects in the formulation.

In addition, the mathematical framework of elastic viscoplastic modeling, based on Perzyna's overstress theory, was briefly outlined. A unprecedented interpretation of the undrained hydrostatic relaxation test was proposed to calibrate the viscous nucleus functional.

The application of these concepts to simulate the behavior of geomaterials will be presented in Chapter 6.

4
Numerical integration of constitutive equations

4.1
Overview of integration schemes

A wide range of geological materials can be characterized by means of a set of constitutive relations of the general form

$$\epsilon_j = \epsilon_j^e + \epsilon_j^p \tag{4-1}$$

$$\dot{\sigma}_i = D_{ij}^e \, \dot{\epsilon}_j^e \tag{4-2}$$

$$\dot{\epsilon}_j^p = \dot{\lambda} \, \frac{\partial g}{\partial \sigma_j} \tag{4-3}$$

$$h_k = h_k(\epsilon_j^p) \tag{4-4}$$

where, according to Ortiz and Popov (1985); Ortiz and Simo (1986), ϵ_j, ϵ_j^e and ϵ_j^p denote the vectors total, elastic and plastic strains, σ_i is the vector of Cauchy stresses and h_k is a set of hardening variables. Equation 4-1 expresses the commonly assumed additive strain decomposition. Equation 4-2 represents the generalized Hooke's law, with the material stiffness matrix D_{ij}^e that may vary during loading. Equation 4-3 states that the plastic strain rates are derived from a flow rule, that is expressed in rate form and is not necessarily associated, and Equation 4-4 signifies that a strain hardening rule is assumed, in which the evolution of the yield surface depends on the history of the plastic deformations. The plastic multiplier, $\dot{\lambda}$, has to be determined with the aid of the loading-unloading criterion. This can be expressed in Kuhn-Tucker conditions:

$$f(\sigma_i, h_k) \leq 0 \tag{4-5}$$

$$\dot{\lambda} \geq 0 \tag{4-6}$$

$$f \, \dot{\lambda} = 0 \tag{4-7}$$

where $f(\sigma_i, h_k)$ is the yield function of the material. Plastic strains are activated if the yield criterion is violated. Along any process of loading, the Kuhn-Tucker conditions must hold simultaneously. The plastic multiplier is obtained enforcing the so-called plastic consistency condition:

$$df = \frac{\partial f}{\partial \sigma_i} d\sigma_i + \frac{\partial f}{\partial h_k} dh_k = 0 \tag{4-8}$$

Integration of rate constitutive equation is performed at Gauss-point level, requiring the time integration of the flow rule in Equation 4-3. The procedure is discrete in time, with small increments of plastic strains calculated according to the following time integration scheme over Δt:

$$\Delta \epsilon_i^p = \int_t^{t+\Delta t} \dot{\lambda} \frac{\partial g}{\partial \sigma_i} \approx \Delta\lambda \, b_i \tag{4-9}$$

A numerical algorithm is often necessary to evaluate the components of vector b_i, because finding an analytical solution is not trivial. The trapezoidal rule or the midpoint rule are common choices. They are also referred as the θ-method:

$$b_i = (1-\theta) \frac{\partial g}{\partial \sigma_i}^{t} + \theta \frac{\partial g}{\partial \sigma_i}^{t+\Delta t} = \frac{\partial g}{\partial \sigma_i}^{t+\theta\Delta t} \tag{4-10}$$

The values most commonly assigned to θ correspond to the following schemes:

- $\theta = 0$ Forward Euler (Explicit or semi-implicit)
- $\theta = \frac{1}{2}$ Crank-Nicholson
- $\theta = \frac{2}{3}$ Galerkin
- $\theta = 1$ Backward Euler (Fully implicit)

Various geometric return mapping schemes for the integration of rate constitutive equations applicable to soil constitutive models are depicted in Figure 4.1. All consist of a return to the yield surface. Here, three alternative procedures are outlined:

1. Implicit Backward Euler Scheme.
2. Semi-implicit Forward Euler Scheme.
3. Explicit integration with substepping.

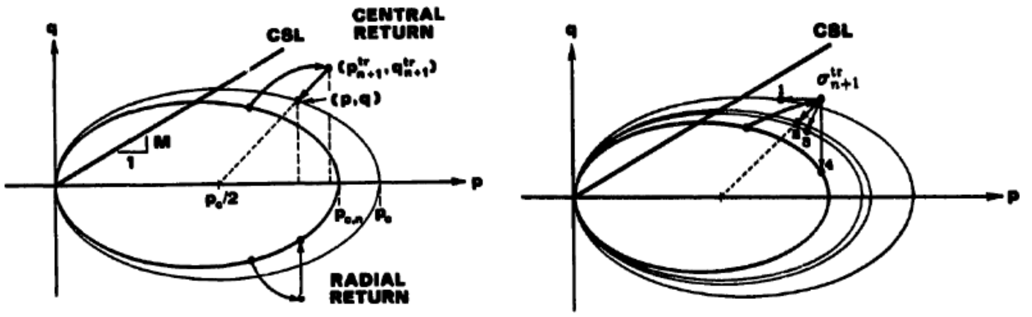

Figure 4.1: Return mapping directions (Borja and Lee, 1990): 1. Hydrostatic return, 2. central return, 3. closest point projection, 4. radial return.

Implicit Backward Euler Scheme

In the fully implicit backward Euler method (Crisfield, 1991; Simo and Hughes, 1998; de Souza Neto et al., 2009; de Borst et al., 2012; Belytschko et al., 2013), the increments in plastic strain are calculated with the flow rule evaluated at the end of the time step. Thus the integration scheme is implicit in plastic flow directions and in the plastic multiplier. An iterative procedure for the solution of the implicit Backward Euler Scheme is necessary and, in general, the standard Newton–Raphson method is employed. Implicit methods are attractive because they are unconditionally stable and the resulting stresses automatically satisfy the yield criterion to a specified tolerance. Furthermore, they do not require the intersection with the yield surface to be computed if the stress point changes from an elastic state to a plastic state.

Semi-implicit Forward Euler Scheme

The semi-implicit Euler scheme (Belytschko et al., 2013) is implicit in the plasticity parameter and explicit in the plastic flow direction. In other words, the plastic multiplier is calculated by enforcing the consistency condition at the end of the step to avoid drift from the yield surface.

Explicit integration with substepping

Explicit algorithms for integrating the elastoplastic constitutive relations have been provided by Sloan (1987); Sloan et al. (2001). In the explicit scheme, the applied strain increment is automatically divided into subincrements using an estimate of the local error and attempt to control the global integration error in the stresses. For a given scheme, the number of substeps used is a function of the error tolerance specified, the magnitude of the imposed strain increment, and the non-linearity of the constitutive relations. Notable examples are the *modified Euler scheme with substeps of variable size* and the *classical Runge-Kutta scheme.*

4.2
Implicit integration: backward Euler algorithm

The backward Euler elastoplastic integration algorithm is given in the general form (Ortiz and Popov, 1985; Tamagnini et al., 2002a,b):

$$\{\boldsymbol{\Delta\epsilon}\} = \{\boldsymbol{\Delta\epsilon}^{\mathrm{e}}\} + \{\boldsymbol{\Delta\epsilon}^{\mathrm{p}}\} \tag{4-11}$$

$$\{\boldsymbol{\Delta\epsilon}^{\mathrm{p}}\} = \Delta\lambda\,\{{}^{t+\Delta t}\boldsymbol{b}\} \tag{4-12}$$

$$\{\boldsymbol{\sigma}^{E}\} = \{{}^{t}\boldsymbol{\sigma}\} + [\boldsymbol{C}^{E}]\,\{\boldsymbol{\Delta\epsilon}\} \tag{4-13}$$

$$\{{}^{t+\Delta t}\boldsymbol{\sigma}\} = \{\boldsymbol{\sigma}^{E}\} - \Delta\lambda\,[\boldsymbol{C}^{E}]\,\{{}^{t+\Delta t}\boldsymbol{b}\} \tag{4-14}$$

$$\{{}^{t+\Delta t}\boldsymbol{p_o}\} = \{{}^{t}\boldsymbol{p_o}\} + \Delta\lambda\,\{{}^{t+\Delta t}\boldsymbol{h}\} + \Delta X_d\,\{{}^{t}\boldsymbol{w}\} \tag{4-15}$$

$${}^{t+\Delta t}f = 0 \tag{4-16}$$

The Backward Euler algorithm involves the vectors $\{{}^{t+\Delta t}\boldsymbol{b}\}$, $\{{}^{t+\Delta t}\boldsymbol{h}\}$ that are evaluated at the final position $\{{}^{t+\Delta t}\boldsymbol{\sigma}\}$, $\{{}^{t+\Delta t}\boldsymbol{p_o}\}$, for which the state of stress satisfy the consistency condition ${}^{t+\Delta t}f = 0$. Because these quantities cannot be directly computed from the current state of stress, an iterative procedure must be used to solve the non-linear equations (Crisfield, 1991).

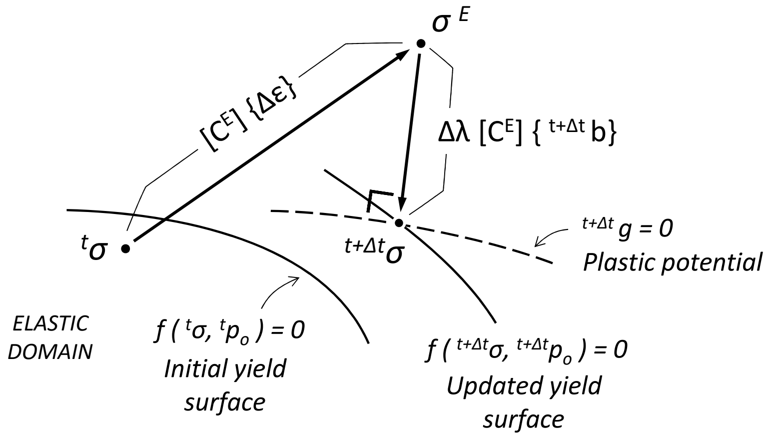

Figure 4.2: Representation of Backward Euler method.

The return mapping algorithm can be conveniently defined based on the elastic-plastic split by first integrating the elastic equations to obtain an *elastic predictor*, which is the taken as an initial condition for the *plastic corrector* phase (Ortiz and Simo, 1986).

The algorithm starts with freezing the plastic strain and applying the elastic predictor:

$$\{\boldsymbol{\sigma}^E\} = \{{}^t\boldsymbol{\sigma}\} + [\boldsymbol{C}^E]\,\{\boldsymbol{\Delta\epsilon}\} \tag{4-17}$$

$$\{\boldsymbol{p}_o^E\} = \{{}^t\boldsymbol{p}_o\} + \Delta X_d\{{}^t\boldsymbol{w}\} \tag{4-18}$$

if yield criterion is violated after trial elastic increment, i.e. $f(\boldsymbol{\sigma}^E, \boldsymbol{p}_o^E) > 0$, then the state of stress is outside the yield locus and plastic strains must be computed by solving the non-linear constitutive equations (Eqs. 4-14 to 4-16) according to Newton-Raphson procedure. Rewriting the system of equations, the residuals are defined as follows:

$$\{\boldsymbol{r}_\sigma\} = \{\boldsymbol{\sigma}^E\} - \{{}^{t+\Delta t}\boldsymbol{\sigma}\} - \Delta\lambda\,[\boldsymbol{C}^E]\,\{{}^{t+\Delta t}\boldsymbol{b}\} \tag{4-19}$$

$$\{\boldsymbol{r}_{p_o}\} = \{\boldsymbol{p}_o^E\} - \{{}^{t+\Delta t}\boldsymbol{p_o}\} + \Delta\lambda\,\{{}^{t+\Delta t}\boldsymbol{h}\} \tag{4-20}$$

$$r_f = -{}^{t+\Delta t}f \tag{4-21}$$

iterations are performed to reduce the residuals to (almost) zero. With the trial elastic stress, $\{\boldsymbol{\sigma}^E\}$, being kept fixed, a truncated Taylor expansion is applied in order to minimize the residuals at each iteration:

$$\{\boldsymbol{r}_\sigma^{(k)}\} = \{\boldsymbol{r}_\sigma^{(k-1)}\} - \{\boldsymbol{d\sigma}\} - d\lambda\,[\boldsymbol{C}^E]\,\{{}^{t+\Delta t}\boldsymbol{b}\} - \Delta\lambda\,[\boldsymbol{C}^E]\,\{\boldsymbol{db}\} \tag{4-22}$$

$$\{\boldsymbol{r}_{p_o}^{(k)}\} = \{\boldsymbol{r}_{p_o}^{(k-1)}\} - \{\boldsymbol{dp_o}\} + d\lambda\,\{{}^{t+\Delta t}\boldsymbol{h}\} + \Delta\lambda\,\{\boldsymbol{dh}\} \tag{4-23}$$

$$r_f^{(k)} = r_f^{(k-1)} - df \tag{4-24}$$

in which the following differentials can be introduced:

$$\{\boldsymbol{db}\} = \left[\frac{\partial \boldsymbol{b}}{\partial \boldsymbol{\sigma}}\right]\{\boldsymbol{d\sigma}\} + \left[\frac{\partial \boldsymbol{b}}{\partial \boldsymbol{p}_o}\right]\{\boldsymbol{dp_o}\} \tag{4-25}$$

$$\{\boldsymbol{dh}\} = \left[\frac{\partial \boldsymbol{h}}{\partial \boldsymbol{\sigma}}\right]\{\boldsymbol{d\sigma}\} + \left[\frac{\partial \boldsymbol{h}}{\partial \boldsymbol{p}_o}\right]\{\boldsymbol{dp_o}\} \tag{4-26}$$

$$df = \{\boldsymbol{a}\}^{\mathsf{T}}\{\boldsymbol{d\sigma}\} + \{\partial f/\partial \boldsymbol{p}_o\}^{\mathsf{T}}\{\boldsymbol{dp_o}\} \tag{4-27}$$

Setting $\{\boldsymbol{r}^{(k)}\} = 0$ and after some algebraic manipulations, it is possible to solve the previous equations to obtain the iterative changes:

$$\begin{Bmatrix} \boldsymbol{d\sigma} \\ \boldsymbol{dp_o} \\ d\lambda \end{Bmatrix} = \left[\boldsymbol{Q}^{(k-1)}\right]^{-1} \begin{Bmatrix} \boldsymbol{r}_{\sigma}^{(k-1)} \\ \boldsymbol{r}_{p_o}^{(k-1)} \\ r_{f}^{(k-1)} \end{Bmatrix} \tag{4-28}$$

where the matrix $[\boldsymbol{Q}]$ can be evaluated as (Tamagnini et al., 2002a,b):

$$[\boldsymbol{Q}] = \left[\begin{array}{c|c|c} [\mathbf{I}] + \Delta\lambda\,[\boldsymbol{C}_E] \left[\dfrac{\partial \boldsymbol{b}}{\partial \boldsymbol{\sigma}}\right] & \Delta\lambda\,[\boldsymbol{C}_E] \left[\dfrac{\partial \boldsymbol{b}}{\partial \boldsymbol{p_o}}\right] & [\boldsymbol{C}_E]\,\{\boldsymbol{b}\} \\ \hline -\Delta\lambda \left[\dfrac{\partial \boldsymbol{h}}{\partial \boldsymbol{\sigma}}\right] & [\mathbf{I}] - \Delta\lambda \left[\dfrac{\partial \boldsymbol{h}}{\partial \boldsymbol{p_o}}\right] & -\{\boldsymbol{h}\} \\ \hline \{\boldsymbol{a}\}^{\mathsf{T}} & \{\partial f/\partial \boldsymbol{p_o}\}^{\mathsf{T}} & 0 \end{array}\right]$$

This iterative procedure is continued until convergence given a certain tolerance, at the final stress state. Stresses, hardening parameters and plastic multiplier are updated at each iteration according to:

$$\left\{{}^{t+\Delta t}\boldsymbol{\sigma}^{(k)}\right\} = \left\{{}^{t+\Delta t}\boldsymbol{\sigma}^{(k-1)}\right\} + \left\{\boldsymbol{d\sigma}^{(k)}\right\} \tag{4-29}$$

$$\left\{{}^{t+\Delta t}\boldsymbol{p_o}^{(k)}\right\} = \left\{{}^{t+\Delta t}\boldsymbol{p_o}^{(k-1)}\right\} + \left\{\boldsymbol{dp_o}^{(k)}\right\} \tag{4-30}$$

$$\Delta\lambda^{(k)} = \Delta\lambda^{(k-1)} + d\lambda^{(k)} \tag{4-31}$$

A starting estimate for the iterative procedure can be obtained evaluating all quantities at trial elastic stress. A first guess for the plastic multiplier is:

$$\Delta\lambda^{(0)} = \frac{f^E}{\{\boldsymbol{a}_E\}^{\mathsf{T}}[\boldsymbol{C}^E]\,\{\boldsymbol{b}_E\} + H_E} \tag{4-32}$$

then, starting stresses are evaluated:

$$\left\{{}^{t+\Delta t}\boldsymbol{\sigma}^{(0)}\right\} = \{\boldsymbol{\sigma}^E\} - \Delta\lambda^{(0)}\,[\boldsymbol{C}^E]\,\{\boldsymbol{b}_E\} \tag{4-33}$$

as well as hardening variables:

$$\left\{{}^{t+\Delta t}\boldsymbol{p_o}^{(0)}\right\} = \{\boldsymbol{\sigma}^E\} + \Delta\lambda^{(0)}\,\{\boldsymbol{h}_E\} \tag{4-34}$$

Iterative procedure simply consists in evaluating the residuals and the $[\boldsymbol{Q}]$ matrix taking stresses, hardening parameters and plastic multiplier from previous iteration. However, the calculation of the second derivatives of hardening laws and plastic potential may difficult the implementation of the method.

4.2.1
Nonlinear elastic integration

Non-linear elasticity involves the integration of rate equations:

$$\dot{\sigma}_i = D^e_{ij}\,\dot{\epsilon}^e_j \rightarrow \Delta\sigma_i = \int_t^{t+\Delta t} D^e_{ij}\,\dot{\epsilon}^e_j dt \approx \bar{D}^e_{ij}\,\Delta\epsilon^e_j \tag{4-35}$$

where D^e_{ij} is the tangent material stiffness matrix, $\bar{D}^e_{ij}$ is the secant (average) material stiffness matrix within the time step and $\Delta\epsilon^e_j$ are the elastic strain increments, assumed to be equal to the total strains in a purely elastic step. The material stress-strain behavior is usually expressed in terms of tangent (instantaneous) stiffness, as the laws are expressed in rate of stress to rate of strain form. In nonlinear elasticity the coefficients of matrix D^e_{ij} are assumed to be dependent on the state of stress (or strain). If an analytical expression for $\bar{D}^e_{ij}$ is not available, a numerical procedure is needed for time integration. As instance, the secant stiffness may be approximated with the trapezoidal rule

$$\bar{D}^e_{ij} = (1-\theta)(D^e_{ij})^t + \theta(D^e_{ij})^{t+\Delta t} \tag{4-36}$$

and the the nonlinear system $\bar{D}^e_{ij}\,\Delta\epsilon^e_j - \Delta\sigma_i = 0$ can be solved by means, for example, of Newton-Raphson method. In this case, the system is reduced to its residual form:

$$r_i = \bar{D}^e_{ij}\,\Delta\epsilon^e_j - \Delta\sigma_i \tag{4-37}$$

and applying a truncated Taylor expansion:

$$r_i + dr_i = r_i + d\bar{D}^e_{ij}\,\Delta\epsilon^e_j - d\sigma_i \tag{4-38}$$

with $d\bar{D}^e_{ij} = \frac{\partial \bar{D}^e_{ij}}{\partial \sigma_k}\,d\sigma_k$ one obtains:

$$r_i + \left(\frac{\partial \bar{D}^e_{ij}}{\partial \sigma_k}\,\Delta\epsilon^e_j - \delta_{ik}\right) d\sigma_k = 0 \tag{4-39}$$

with the predictor $Q_{ik} = \delta_{ik} - \frac{\partial \bar{D}^e_{ij}}{\partial \sigma_k}\Delta\epsilon^e_j$. This means that for nonlinear elastic behavior, an iterative solution may be necessary.

4.2.2
Viscoplastic integration

The Perzyna's viscoplastic strain rate (Eq. 3-33) is integrated over time either using the generalized trapezoidal rule or the generalized midpoint rule:

$$\boldsymbol{\Delta\epsilon}^{vp} = \int_t^{t+\Delta t} \dot{\boldsymbol{\epsilon}}^{vp} dt \approx \left[(1-\theta)(\dot{\boldsymbol{\epsilon}}^{vp})^t + \theta(\dot{\boldsymbol{\epsilon}}^{vp})^{t+\Delta t}\right]\Delta t \tag{4-40}$$

$$\approx (\dot{\boldsymbol{\epsilon}}^{vp})^{t+\theta\Delta t}\Delta t \tag{4-41}$$

The values most commonly assigned to θ correspond to the following methods:

- $\theta = 0$ Forward Euler (explicit)
- $\theta = \frac{1}{2}$ Crank-Nicholson
- $\theta = \frac{2}{3}$ Galerkin
- $\theta = 1$ Backward Euler

It is assumed that total strains can be decoupled into an elastic (recoverable) and a viscoplastic part. Then, they may be written in vectorial form as:

$$\Delta\epsilon_i = \Delta\epsilon_i^e + \Delta\epsilon_i^{vp} \tag{4-42}$$

where the Perzyna's viscoplastic strains are integrated according to a Backward Euler scheme:

$$\Delta\epsilon_i^{vp} = \frac{\Delta t}{\mu}\phi^{t+\Delta t}\frac{\partial g}{\partial\sigma_i}^{t+\Delta t} \tag{4-43}$$

Stress increments are computed according to non-linear elastic constitutive equations:

$$\Delta\sigma_i = \bar{D}_{ij}^e\Delta\epsilon_j^e \tag{4-44}$$

and state variables are updated according to a strain-hardening rule:

$$h_k^{t+\Delta t} = h_k(\epsilon_j^{vp}) = h_k(\epsilon_j - \epsilon_j^e)^{t+\Delta t} \tag{4-45}$$

For a given time step, increments in total strains are kept fixed while the elastic parts are set unknown. Therefore, to perform the viscoplastic integration, we define the residuals:

$$r_i = \Delta\epsilon_i - \Delta\epsilon_i^e - \Delta\epsilon_i^{vp} \tag{4-46}$$

As a matter of fact, viscoplastic strains are treated as functions of stresses, which in turn are functions of elastic strains:

$$d\epsilon_i^{vp} = \frac{\Delta t}{\mu}(b_i\,d\phi + \phi\,db_i) = \frac{\Delta t}{\mu}(b_i f_j + \phi B_{ij})\,d\epsilon_j^e \tag{4-47}$$

where the following differentials have been introduced:

$$d\phi = \frac{d\phi}{dF}\left(\frac{\partial F}{\partial\sigma_i}d\sigma_i + \frac{\partial F}{\partial h_k}dh_k\right) = \frac{d\phi}{dF}\left(\frac{\partial F}{\partial\sigma_i}D_{ij}^e + \frac{\partial F}{\partial h_k}\frac{\partial h_k}{\partial\epsilon_j^e}\right)d\epsilon_j^e = f_j\,d\epsilon_j^e \tag{4-48}$$

$$db_i = \frac{\partial b_i}{\partial\sigma_k}d\sigma_k + \frac{\partial b_i}{\partial h_m}dh_m = \left(\frac{\partial b_i}{\partial\sigma_k}D_{kj}^e + \frac{\partial b_i}{\partial h_m}\frac{\partial h_m}{\partial\epsilon_j^e}\right)d\epsilon_j^e = B_{ij}\,d\epsilon_j^e \tag{4-49}$$

Finally, applying a truncated Taylor expansion to the residuals, defined in Eq. 4-46:

$$r_i + dr_i = r_i - d\epsilon_i^e - d\epsilon_i^{vp} \tag{4-50}$$

the following linear system is obtained for Newton-Raphson iterations:

$$r_i + dr_i = r_i - \left[\delta_{ij} + \frac{\Delta t}{\mu}(b_i f_j + \phi B_{ij})\right]d\epsilon_j^e = 0 \tag{4-51}$$

thus, introducing the predictor

$$Q_{ij} = \delta_{ij} + \frac{\Delta t}{\mu}(b_i f_j + \phi B_{ij}) \tag{4-52}$$

where δ_{ij} is the the Kronecker delta, the iterative solution is:

$$d\epsilon_i^e = Q_{ij}^{-1} r_j \tag{4-53}$$

In general, the inversion of matrix Q_{ij} is not necessary. The linear system can be easily solved with algebraic methods. At most, a 6x6 linear system has to be solved.

4.3
Forward integration

4.3.1
Standard procedure

The Forward Euler elastoplastic integration algorithm is given in the general form:

$$\{\boldsymbol{\Delta\epsilon}\} = \{\boldsymbol{\Delta\epsilon}^{\mathrm{e}}\} + \{\boldsymbol{\Delta\epsilon}^{\mathrm{p}}\} \tag{4-54}$$

$$\{\boldsymbol{\Delta\epsilon}^{\mathrm{p}}\} = \Delta\lambda \, \{\boldsymbol{b}_X\} \tag{4-55}$$

$$\{\boldsymbol{\sigma}^E\} = \{{}^t\boldsymbol{\sigma}\} + [\boldsymbol{C}^E] \, \{\boldsymbol{\Delta\epsilon}\} \tag{4-56}$$

$$\{{}^{t+\Delta t}\boldsymbol{\sigma}\} = \{\boldsymbol{\sigma}^E\} - \Delta\lambda \, [\boldsymbol{C}^E] \, \{\boldsymbol{b}_X\} \tag{4-57}$$

$$\{{}^{t+\Delta t}\boldsymbol{p_o}\} = \{{}^t\boldsymbol{p_o}\} + \Delta\lambda \, \{\boldsymbol{h}_X\} + \Delta X_d \, \{{}^t\boldsymbol{w}\} \tag{4-58}$$

$${}^{t+\Delta t}f = 0 \tag{4-59}$$

The Forward Euler algorithm involves the vectors $\{\boldsymbol{b}_X\}, \{\boldsymbol{h}_X\}$ that are evaluated at the intersection point of the elastic predictor with the yield function. Hence, having computed $\{\boldsymbol{\sigma}^X\}$ and $\{\boldsymbol{p_o}^X\}$, enforcing consistency allows to determine the plastic multiplier, the only unknown quantity.

The algorithm starts with applying the elastic predictor:

$$\{\boldsymbol{\sigma}^E\} = \{{}^t\boldsymbol{\sigma}\} + [\boldsymbol{C}^E] \, \{\boldsymbol{\Delta\epsilon}\} \tag{4-60}$$

$$\{\boldsymbol{p}_o^E\} = \{{}^t\boldsymbol{p}_o\} + \Delta X_d \{{}^t\boldsymbol{w}\} \tag{4-61}$$

if yield criterion is violated after trial chemo-elastic increment, i.e. $f(\boldsymbol{\sigma}^E, \boldsymbol{p}_o^E) > 0$, then the state of stress is outside the yield locus and the elastic predictor crosses the yield function at a certain point. In this case, stresses must be calculated elastoplastically.

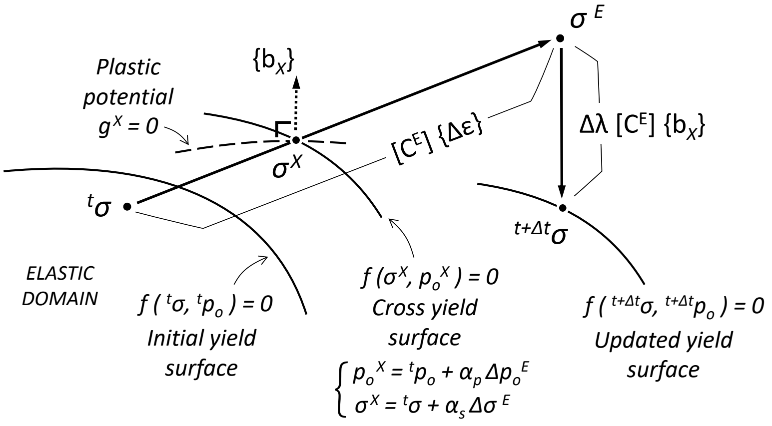

Figure 4.3: Representation of Forward Euler method.

Integrating the constitutive requires computing the vectors $\{\boldsymbol{b}_X\}, \{\boldsymbol{h}_X\}$ at intersection point. Chemical effects are applied first. Stresses are kept fixed during trial hardening/softening and yield criterion is checked. If the stress point is outside the elastic domain, i.e. $f({}^t\boldsymbol{\sigma}, \boldsymbol{p}_o^E) > 0$, then yield surface intersection is found by solving the non-linear equation in the variable α_p:

$$f({}^t\boldsymbol{\sigma},\ {}^t\boldsymbol{p}_o + \alpha_p\, \Delta X_d\, {}^t\boldsymbol{w}) = 0$$

On the other hand, if the stress point is still within the elastic domain after chemical attack, the intersection point is found by solving the non-linear equation in the variable α_s:

$$f({}^t\boldsymbol{\sigma} + \alpha_s\, \boldsymbol{C}^E\, \boldsymbol{\Delta\epsilon},\ \boldsymbol{p}_o^E) = 0$$

A Pegasus procedure is ideally suited to solving the yield surface intersection problem since it is unconditionally convergent, does not require the use of derivatives, and typically converges in four or five iterations (Sloan et al., 2001).

The intersection point is finally:

$$\{\boldsymbol{\sigma}^X\} = \{{}^t\boldsymbol{\sigma}\} + \alpha_s\, [\boldsymbol{C}^E]\, \{\boldsymbol{\Delta\epsilon}\} \tag{4-62}$$

$$\{\boldsymbol{p}_o^X\} = \{{}^t\boldsymbol{p}_o\} + \alpha_p\, \Delta X_d \{{}^t\boldsymbol{w}\} \tag{4-63}$$

and the vectors $\{\boldsymbol{b}_X\}, \{\boldsymbol{h}_X\}$ can be calculated at once.

The forward integration starts with a first guess for the plastic multiplier with a first-order tailor expansion of the yield function at the intersection point:

$${}^{t+\Delta t}f = \underbrace{f^X}_{=0} + \{\boldsymbol{a}_X\}^\mathsf{T}\{\boldsymbol{\Delta\sigma}\} + \{\partial f / \partial \boldsymbol{p}_{\boldsymbol{o}X}\}^\mathsf{T}\{\boldsymbol{\Delta p_o}\} = 0$$

with

$$\begin{aligned}\{\boldsymbol{\Delta\sigma}\} &= (1-\alpha_s)\{\boldsymbol{\Delta\sigma}^E\} - \Delta\lambda\,[\boldsymbol{C}^E]\,\{\boldsymbol{b}_X\}\\ \{\boldsymbol{\Delta p_o}\} &= (1-\alpha_p)\{\boldsymbol{\Delta p_o}^E\} + \Delta\lambda\,\{\boldsymbol{h}_X\}\end{aligned}$$

yields:

$$\Delta\lambda^{(0)} = \frac{(1-\alpha_s)\{\boldsymbol{a}_X\}^\mathsf{T}\{\boldsymbol{\Delta\sigma}^E\} + (1-\alpha_p)\{\partial f/\partial \boldsymbol{p_o}_X\}^\mathsf{T}\{\boldsymbol{\Delta p_o}^E\}}{\{\boldsymbol{a}_X\}^\mathsf{T}\,[\boldsymbol{C}^E]\,\{\boldsymbol{b}_X\} + H_X} \tag{4-64}$$

With this initial estimation, the stress point will not always lies on the yield surface. Therefore, an iterative procedure is needed to refine the value of the plastic multiplier. The iterative change is obtained with a Newton-Raphson procedure:

$$d\lambda^{(k)} = \frac{{}^{t+\Delta t}f^{(k-1)}}{\{\boldsymbol{a}_X\}^\mathsf{T}\,[\boldsymbol{C}^E]\,\{\boldsymbol{b}_X\} + H_X} \tag{4-65}$$

where

$${}^{t+\Delta t}f^{(k)} = f\left(\boldsymbol{\sigma}^E - \Delta\lambda^{(k)}\,\boldsymbol{C}^E\,\boldsymbol{b}_X,\ \boldsymbol{p_o}^E + \Delta\lambda^{(k)}\,\boldsymbol{h}_X\right) \tag{4-66}$$

4.3.2
Alternative procedure

Elastic and plastic strains are set unknown. Within the time step, the following relation holds:

$$\Delta\epsilon_i = \Delta\epsilon_i^e + \Delta\epsilon_i^p \tag{4-67}$$

differentiating the above strain decomposition gives:

$$d\epsilon_i^e = -d\epsilon_i^p \tag{4-68}$$

that is equivalent to say that the sum of elastic and plastic strains is a constant, because the increments in total strains are fixed, their value given from the global equilibrium solution. The plastic strains are calculated according to flow rule:

$$\Delta\epsilon_i^p = \Delta\lambda\, b_i \tag{4-69}$$

where b_i is the vector containing the components of plastic flow rule, i.e. the partial derivatives of plastic potential with respect the stresses. Because the method is *forward*, partial derivatives are calculated at once at the beginning of time step or at crossing point. Nonlinear elastic behavior can be accounted by introducing the secant elastic stiffness matrix:

$$\Delta\sigma_i = \bar{D}_{ij}^e\,\Delta\epsilon_j^e \tag{4-70}$$

Hardening behavior is simply described by a suitable strain hardening rule:

$$h_k^{t+\Delta t} = h_k(\epsilon_j^p)^{t+\Delta t} \tag{4-71}$$

With all these requirements, the value of plastic multiplier is finally obtained by enforcing the consistency rule $f^{t+\Delta t} = 0$ at the end of time step. It is a nonlinear equation in the plastic multiplier. The Newton-Raphson method can be employed to find the root. Applying a truncated Taylor expansion:

$$f^{(k)} + df^{(k)} = f^{(k)} + \frac{\partial f}{\partial \sigma_i} d\sigma_i + \frac{\partial f}{\partial h_m} dh_m = 0 \tag{4-72}$$

the following incremental forms

$$\begin{cases} d\sigma_i = D_{ij}^e \, d\epsilon_j^e = -D_{ij}^e \, d\epsilon_j^p = -D_{ij}^e \, d\lambda \, b_j \\ dh_m = \dfrac{\partial h_m}{\partial \epsilon_j^p} d\epsilon_j^p = \dfrac{\partial h_m}{\partial \epsilon_j^p} d\lambda \, b_j \end{cases} \tag{4-73}$$

are substituted into Eq 4-72 to obtain the iterative update for the plastic multiplier:

$$d\lambda^{(k)} = \frac{f^{(k)}}{a_i \, D_{ij}^e \, b_j + H} \tag{4-74}$$

where:

$$a_i = \frac{\partial f}{\partial \sigma_i}$$
$$b_j = \frac{\partial g}{\partial \sigma_j}$$
$$H = -\frac{\partial f}{\partial h_m} \frac{\partial h_m}{\partial \epsilon_j^p} b_j$$

and D_{ij}^e is the tangent material stiffness. The plastic multiplier is updated at each iteration

$$\Delta\lambda^{(k+1)} = \Delta\lambda^{(k)} + d\lambda^{(k)}$$

and the Newton-Raphson loop is repeated until the error reduces below a given tolerance. The first guess for the plastic multiplier may be, as usual, the trial elastic solution $\Delta\lambda^{(0)} = 0$.

4.3.3
Crossing the yield surface

Newton-Raphson method can also be employed to solving the yield surface intersection problem. Crisfield (1991) presents the standard procedure for the location of the intersection of the elastic stress vector with the yield surface. In this case the strains (not the stresses) are opportunely scaled by a factor, α, that is $\Delta\epsilon_j^e = \alpha\Delta\epsilon_j$, for which it is required that $f(\alpha) = 0$.

For a general yield function, the truncated Taylor expansion is:

$$f + df = f + \frac{\partial f}{\partial \sigma_i}\, d\sigma_i + \cancel{\frac{\partial f}{\partial p_0} dp_0} = \frac{\partial f}{\partial \sigma_i}\, D^e_{ij}\, d\epsilon^e_j = \frac{\partial f}{\partial \sigma_i}\, D^e_{ij}\, \Delta\epsilon_j\, d\alpha \tag{4-75}$$

Hardening parameters do not vary in this circumstance because plastic strains are not activated. The scalar α is iteratively updated using $\alpha^{(k+1)} = \alpha^{(k)} + d\alpha^{(k)}$ with:

$$d\alpha^{(k)} = \frac{-f^{(k)}}{a_i\, D^e_{ij}\, \Delta\epsilon_j} \tag{4-76}$$

The first guess for α may be $\alpha^{(0)} = \frac{-f^t}{f^e - f^t}$. Consequently, stresses are updated according to nonlinear elasticity $\Delta\sigma_i = \bar{D}^e_{ij}\, \Delta\epsilon^e_j$. The remaining part of total strain increments $(1-\alpha)\Delta\epsilon_j$, violating the yield condition, will be integrated in an elastoplastic manner.

4.4
Integration under mixed control

Implicit and explicit stress integration schemes have been addressed in previous sections considering the analysis of the strain-driven problems, which are merely special cases of the general mixed control. For the calibration and evaluation of soil constitutive models, one may need to simulate a number of laboratory experiments performed under stress control, strain control and under mixed control. Mixed control is encountered in most laboratory experiments. The drained triaxial compression tests is an example where the axial strain and the cell pressure are the controlled variables. In other words, mixed control occurs when a suitable combination of strain and stress components are given a prescribed variation (Alawaji et al., 1992). Then, it seems to be useful to develop a ready-to-use integration algorithm in elastoplasticity to deal with mixed control when developing soil constitutive models, at a first stage before finite element implementation.

The integration of constitutive equation under mixed control involves the solution of the following problem: given a deviatoric strain increment, $\Delta\epsilon_s$, compute $\Delta\epsilon_v$ and $\Delta\lambda$ and the stresses at the end of time step $p^{t+\Delta t}$ and $q^{t+\Delta t}$ enforcing the stress ratio $m_r = \Delta q/\Delta p$ ($m_r = 3$ for a drained triaxial compression test).

It is worth noting that an implicit integration can be adopted for mixed control, however, for simplicity, a forward integration scheme is employed herein to solve the following nonlinear system of constitutive equations:

$$p^{t+\Delta t} = p^t + K\Delta\epsilon_v - \Delta\lambda\, K\, \frac{\partial g}{\partial p}^{t} \tag{4-77}$$

$$q^{t+\Delta t} = q^t + 3G\Delta\epsilon_s - \Delta\lambda\, 3G\, \frac{\partial g}{\partial q}^{t} \tag{4-78}$$

In order to compute $\Delta\epsilon_v$ and $\Delta\lambda$, given $\Delta\epsilon_s$ and m_r, the condition $\Delta q = m_r\,\Delta p$ is to be enforced:

$$\frac{3G}{m_r}\left(\Delta\epsilon_s - \Delta\lambda\frac{\partial g}{\partial q}^t\right) = K\Delta\epsilon_v - \Delta\lambda\,K\,\frac{\partial g}{\partial p}^t \tag{4-79}$$

along with the consistency condition $f^{t+\Delta t} = 0$. The system of equation is then written in its residual form:

$$\begin{cases} r_\sigma = \frac{3G}{m_r}\left(\Delta\epsilon_s - \Delta\lambda\frac{\partial g}{\partial q}^t\right) - K\left(\Delta\epsilon_v - \Delta\lambda\,\frac{\partial g}{\partial p}^t\right) \\ r_\lambda = f^{t+\Delta t} \end{cases} \tag{4-80}$$

which is a nonlinear system whose solution consists in minimizing the residuals below a given tolerance. The numerical solution is developed applying the Newton-Raphson method. A truncated Taylor expansion is applied:

$$\begin{cases} r_\sigma + dr_\sigma = r_\sigma - \frac{3G}{m_r}\,\frac{\partial g}{\partial q}^t\,d\lambda - K\,d\epsilon_v + K\,\frac{\partial g}{\partial p}^t\,d\lambda = 0 \\ r_\lambda + dr_\lambda = f + df = 0 \end{cases} \tag{4-81}$$

The differential form of the yield function is computed as:

$$df = \{\partial f/\partial\boldsymbol{\sigma}\}^{\mathsf{T}}\{\boldsymbol{d\sigma}\} + \{\partial f/\partial\boldsymbol{p}_o\}^{\mathsf{T}}\{\boldsymbol{dp_o}\} \tag{4-82}$$

where $\{\boldsymbol{d\sigma}\} = \{dp, dq\}$ is the vector of stress increments and $\{\boldsymbol{dp_o}\}$ is the vector of hardening/softening, containing the increments in hardening variables. The components of vector $\{\boldsymbol{d\sigma}\}$ corresponds to the differential form of constitutive equations in 4-77 and 4-78:

$$dp = Kd\epsilon_v - K\,\frac{\partial g}{\partial p}^t\,d\lambda \tag{4-83}$$

$$dq = -3G\,\frac{\partial g}{\partial q}^t\,d\lambda \tag{4-84}$$

and $\{\boldsymbol{dp_o}\} = \{\boldsymbol{h}^t\}\,d\lambda$. Finally, the linear system becomes, in matrix form:

$$\left[\begin{array}{c:c} K & -K\,\dfrac{\partial g}{\partial p}^t + \dfrac{3G}{m_r}\,\dfrac{\partial g}{\partial q}^t \\ \hdashline -K\,\dfrac{\partial f}{\partial p} & \{\boldsymbol{a}\}^{\mathsf{T}}[\boldsymbol{C}^E]\{\boldsymbol{b}\} + H \end{array}\right] \begin{Bmatrix} d\epsilon_v \\ d\lambda \end{Bmatrix} = \begin{Bmatrix} r_\sigma \\ r_\lambda \end{Bmatrix} \tag{4-85}$$

where:

$$\{\boldsymbol{a}\}^{\mathsf{T}}[\boldsymbol{C}^E]\{\boldsymbol{b}\} = \left\{\frac{\partial f}{\partial\boldsymbol{\sigma}}\right\}^{\mathsf{T}}\left\{K\frac{\partial g}{\partial p}^t,\ \ 3G\frac{\partial g}{\partial q}^t\right\} \tag{4-86}$$

the hardening modulus

$$H = -\{\partial f/\partial\boldsymbol{p}_o\}^{\mathsf{T}}\{\boldsymbol{h}^t\} \tag{4-87}$$

and vectors $\{\partial f/\partial\boldsymbol{\sigma}\}$, $\{\partial f/\partial\boldsymbol{p}_o\}$ are computed at each iteration.

As usual, the first guess is the elastic predictor. The trivial solution is: $\Delta q = \Delta q^e = 3G\Delta\epsilon_s$ and $\Delta p^e = \frac{\Delta q^e}{m_r}$. The volumetric strain is, then, the elastic:

$$\Delta\epsilon_v^e = \frac{3G}{m_r\,K}\Delta\epsilon_s \tag{4-88}$$

If the yield function is violated, the elastoplastic Newton-Raphson iterations may start with the following first guess for the plastic multiplier:

$$\Delta\lambda^{(0)} = (1-\alpha_s)\frac{\sqrt{(\Delta\epsilon_v^e)^2 + (\Delta\epsilon_s)^2}}{\|\boldsymbol{b}\|} \tag{4-89}$$

and volumetric strain:

$$\Delta\epsilon_v^{(0)} = \frac{3G}{m_r\,K}\left(\Delta\epsilon_s - \Delta\lambda\frac{\partial g}{\partial q}^t\right) + \Delta\lambda\frac{\partial g}{\partial p}^t \tag{4-90}$$

Alternatively, the trial elastic solution ($\Delta\lambda = 0$ and $\Delta\epsilon_v = \Delta\epsilon_v^e$) may be assumed as starting point for the Newton-Raphson iterations.

5
Constitutive models formulation and implementation in finite elements

5.1
A model accounting for viscous behavior and non-linear elasticity: Viscous Modified Cam Clay

5.1.1
Preliminaries

The Modified Cam Clay is expressed in terms of stress invariants, being p the "mean stress" and q the "deviator stress":

$$p = \frac{1}{3}(\sigma_1 + \sigma_2 + \sigma_3) \tag{5-1}$$

$$q = \sqrt{\frac{1}{2}[(\sigma_1 - \sigma_2)^2 + (\sigma_2 - \sigma_3)^2 + (\sigma_3 - \sigma_1)^2]} \tag{5-2}$$

A convenient expression for the yield function of Modified Cam Clay is:

$$p\,(p - p_0) + \frac{q^2}{M^2} = 0 \tag{5-3}$$

where M is the critical state parameter and p_0 is the hardening parameter, usually referred as the preconsolidation pressure. The model is associated. In other words, yield function and plastic potential coincide. The corresponding viscoplastic adaptation, according to Perzyna (1963, 1966) approach, arises from rearranging Eq. 5-3, in the form $F = \frac{f(\sigma_{ij})}{k} - 1$, as follows:

$$F = \frac{p_e}{p_0} - 1, \quad p_e = p + \frac{q^2}{M^2 p} \tag{5-4}$$

where F is the yield function based on the concept of "overstress" and p_e is the corresponding "equivalent stress". Figure 5.1 shows the model in the space of stress invariants.

The viscoplastic strain rates are calculated according to Equation 3-33, adopting a viscous nucleus of the exponential type:

$$\phi(F) = e^{bF} - 1 = \exp\left[b\left(\frac{p_e}{p_0} - 1\right)\right] - 1 \tag{5-5}$$

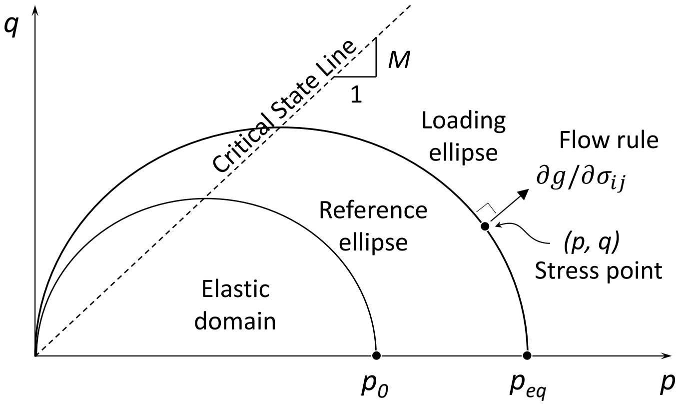

Figure 5.1: Extension of Modified Cam Clay model to Perzyna's theory of viscoplasticity.

As will be seen later in Chapter 6, the choice of the viscous nucleus expression to be exponential is supported by experimental evidence. Finally, the total strain rates of the material can be calculated according to the following expressions:

$$\begin{bmatrix}\dot{\epsilon}_v\\ \dot{\epsilon}_s\end{bmatrix} = \begin{bmatrix}\dot{p}/K\\ \dot{q}/3G\end{bmatrix} + \frac{1}{\mu}\langle \exp\left[b\left(\frac{p_e}{p_0}-1\right)\right]-1\rangle \begin{bmatrix}1-(\eta/M)^2\\ 2\eta/M^2\end{bmatrix} \tag{5-6}$$

These constitutive equations immediately produce the following results:

1. In a hydrostatic stress relaxation test, under undrained conditions, which imply no distortion, no volume change and no shear stress, the sum of the elastic and viscoplastic volumetric deformations is zero. Moreover, since the stress state is represented by a point, which moves along the hydrostatic axis in the principal stress space, the direction of the plastic flow is fixed and aligned with $\eta = 0$. Under the simplifying assumption of a constant bulk modulus, the evolution of the mean effective stress over time can then be calculated by the following integral:

   $$p(t) = p(0) - K\int_0^t \frac{1}{\mu}\langle\phi(F)\rangle dt$$

   that demonstrates, in the relaxation test, the reduction of the mean effective stress over time. As a result, excess pore pressure develops. This is justified because $\langle\phi(F)\rangle$ is always greater than or equal to zero and the respective component of the plastic flow vector is positive, constant and unitary.

2. Analogously, the stress relaxation during an undrained triaxial compres-

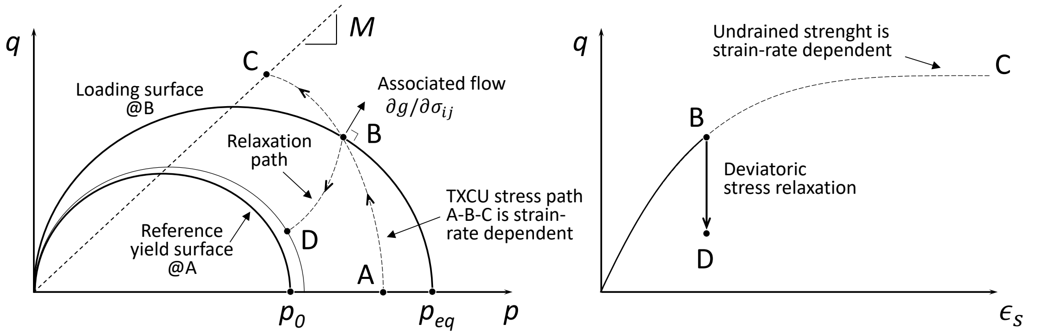

Figure 5.2: Schematic behavior of the model during undrained triaxial stress relaxation.

sion test is:

$$q(t) = q(0) - 3G\int_0^t \frac{1}{\mu}\langle\phi(F)\rangle\frac{\partial g}{\partial q}dt$$

$$p(t) = p(0) - K\int_0^t \frac{1}{\mu}\langle\phi(F)\rangle\frac{\partial g}{\partial p}dt$$

Figure 5.2 shows a schematic of the test and its interpretation according to the present theoretical model. First, the soil is consolidated under hydrostatic state of stress (point A). Then, the drainage valve is closed and a deviator stress is applied by deforming the sample with a constant strain rate. At the desired initial stress the motor of the machine is stopped, thus beginning the stress relaxation (point B) and the vertical load, as well as the pore pressure, are continuosly monitored. The test is carried out on the "wet" side of the domain. The vector of plastic flow is directed outward and is associated to the yield surface. As a consequence, both deviatoric and and mean effective stress will decrease; under constant total stress, pore pressure will raise, accordingly. At point D, the soil has reached equilibrium following the stress relaxation. This behavior is in accordance with experimental findings of Lacerda and Houston (1973). On the "dry" side, the model will predict negative pore pressure development because of dilatancy. In this case, the mean effective stress will raise during a relaxation test, while the deviator stress still continues to decrease.

3. In a creep test, a constant load is maintained and the material exhibits progressive deformation under constant deviator stress ($\dot{q} = 0$). In this case, the constitutive equations takes the form:

$$\dot{\epsilon}_s = \frac{1}{\mu}\langle\phi(F)\rangle\frac{\partial g}{\partial q}$$

As shown in Figure 5.3, depending on the deviatoric stress level, fail-

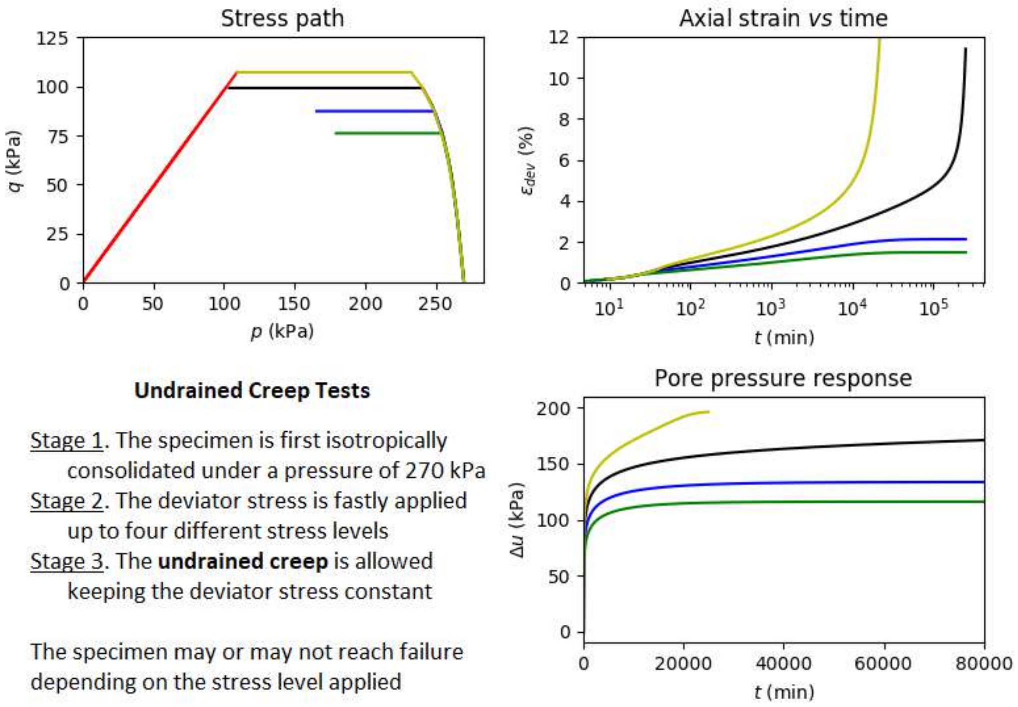

Undrained Creep Tests

Stage 1. The specimen is first isotropically consolidated under a pressure of 270 kPa

Stage 2. The deviator stress is fastly applied up to four different stress levels

Stage 3. The **undrained creep** is allowed keeping the deviator stress constant

The specimen may or may not reach failure depending on the stress level applied

Figure 5.3: Numerically simulated undrained triaxial creep.

ure occurs if the stress point reaches the critical state condition. The application of a higher deviatoric stress causes both greater excess pore pressures and axial strains. When the applied stress cannot be sustained by the material, the equilibrium condition cannot be reached and the axial strain vs time curves show a upward concavity. In this case, the model predicts tertiary creep prior to failure.

4. In an undrained triaxial compression test, performed with a constant strain rate, at failure condition, that is, at critical state ($\eta = M$), the following relation holds:

$$s_u = \frac{1}{2}Mp_e = \frac{1}{2}Mp_0\left[1 + \frac{1}{b}\ln\left(1 + \frac{1}{2}M\mu\dot{\epsilon}_s\right)\right]$$

which points out the relationship between undrained strength and strain rate. Moreover, the expression shows that the undrained strength is the sum of two parts. The former can be defined as "static" because it is independent of the strain rate. The latter arises as a dynamic effect and represents the influence of strain rate on the strength of the material. Taking as an example the results of Kulhawy and Mayne (1990), who concluded that each log cycle increase in strain rate is accompanied by a 10% increse in undrained strength, it can be concluded that the log-linear relationship predicted by the theory is appropriate for clays.

5. In a constant rate of volumetric strain test, the apparent preconsolidation pressure and the volumetric strain rate are related by:

$$\sigma'_p = p_0\left[1 + \frac{1}{b}\ln(1 + \mu\dot{\epsilon}^{vp}_v)\right] \tag{5-7}$$

Where, again, one can see the static and dynamic contributions. The theory seems to be in accordance with experimental findings reported by Leroueil et al. (1985), who have observed the trend of the apparent preconsolidation pressure to increase with the volumetric strain rate.

5.1.2
Elastic behavior

Nonlinear elastic behavior is incorporated in the model according to the formulation proposed by Borja (1991). The bulk modulus is pressure-dependent and the Poisson's ratio is constant. The elastic stress-strain relationships are (in rate form):

$$\dot{\sigma}_i = D^e_{ij}\dot{\epsilon}^e_j = K\dot{\epsilon}^e_v + 2G\dot{e}^e_i \tag{5-8}$$

where $\dot{\epsilon}^e_v = \dot{\epsilon}^e_1 + \dot{\epsilon}^e_2 + \dot{\epsilon}^e_3$ is the rate of volume deformation and $\dot{e}^e_{ij} = \dot{\epsilon}^e_{ij} - \frac{1}{3}\dot{\epsilon}^e_v\delta_{ij}$ is the deviatoric strain rate tensor. For models like Cam Clay, Hooke's law can be written in matrix form, according to Plaxis (2019) manual, as:

$$\begin{bmatrix}\dot{\sigma}_{xx}\\ \dot{\sigma}_{yy}\\ \dot{\sigma}_{zz}\\ \dot{\sigma}_{xy}\\ \dot{\sigma}_{yz}\\ \dot{\sigma}_{zx}\end{bmatrix} = K\begin{bmatrix}c_1 & c_2 & c_2 & 0 & 0 & 0\\ c_2 & c_1 & c_2 & 0 & 0 & 0\\ c_2 & c_2 & c_1 & 0 & 0 & 0\\ 0 & 0 & 0 & c_3 & 0 & 0\\ 0 & 0 & 0 & 0 & c_3 & 0\\ 0 & 0 & 0 & 0 & 0 & c_3\end{bmatrix}\begin{bmatrix}\dot{\epsilon}_{xx}\\ \dot{\epsilon}_{yy}\\ \dot{\epsilon}_{zz}\\ \dot{\gamma}_{xy}\\ \dot{\gamma}_{yz}\\ \dot{\gamma}_{zx}\end{bmatrix} \tag{5-9}$$

$$c_1 = \frac{3-3\nu}{1+\nu}, \quad c_2 = \frac{3\nu}{1+\nu}, \quad c_3 = \frac{3-6\nu}{2+2\nu} \tag{5-10}$$

meaning that the elastic stiffness matrix is the product between the bulk modulus and a matrix with only constant terms, i.e. $D^e_{ij} = K\hat{c}_{ij}$. The bulk modulus is proportional to the mean effective stress:

$$K = \frac{p}{\kappa^*} = \frac{\dot{p}}{\dot{\epsilon}^e_v} \tag{5-11}$$

Integrating the above relation over a finite time increment gives:

$$\int_t^{t+\Delta t}\kappa^*\frac{\dot{p}}{p}dt = \int_t^{t+\Delta t}\dot{\epsilon}^e_v dt \rightarrow \kappa^*\ln(p^{t+\Delta t}/p^t) = \Delta\epsilon^e_v \tag{5-12}$$

after some manipulations, since $\Delta p = \bar{K}\Delta\epsilon^e_v$, the secant bulk modulus is analytically calculated as:

$$\bar{K} = \frac{p^t}{\Delta\epsilon_v^e}(e^{\Delta\epsilon_v^e/\kappa^*} - 1) \tag{5-13}$$

when $\Delta\epsilon_v^e \simeq 0$, the secant and tangent bulk moduli approach the value $\bar{K} \sim \frac{p^t}{\kappa^*}$. This aspect must be included in the numerical computations to avoid division by zero.

Therefore, the stress increments are calculated using a secant material stiffness matrix:

$$\Delta\sigma_i = \bar{K}\Delta\epsilon_v^e + 2\bar{G}\Delta e_i^e \tag{5-14}$$

in which the shear modulus is related to the bulk modulus by means of a constant Poisson's ratio:

$$\bar{G} = \bar{K}\frac{3(1-2\nu)}{2(1+\nu)} \tag{5-15}$$

Working in terms of triaxial stress invariants, the elastic response can be written in compact form using the mean stress, p, the deviator stress, q, the volumetric strain, ϵ_v and the deviatoric strain, ϵ_s:

$$\begin{bmatrix} \dot{p} \\ \dot{q} \end{bmatrix} = \begin{bmatrix} K & 0 \\ 0 & 3G \end{bmatrix} \begin{bmatrix} \dot{\epsilon}_v^e \\ \dot{\epsilon}_s^e \end{bmatrix} \tag{5-16}$$

The off-diagonal zeros indicate the absence of coupling between volumetric and distortional effects for isotropic elastic material (Wood, 1990).

5.1.3
Plastic potential derivatives

To compute the viscoplastic strains, the derivatives of plastic potential must be computed. First derivatives are:

$$\frac{\partial g}{\partial \sigma_i} = \begin{bmatrix} \frac{\partial g}{\partial p} & \frac{\partial g}{\partial q} \end{bmatrix} = \begin{bmatrix} 1 - \frac{\eta^2}{M^2}, & \frac{2\eta}{M^2} \end{bmatrix} \tag{5-17}$$

where $\eta = q/p$ is the stress ratio. The adoption of an implicit integration scheme requires the second order derivatives of plastic potential, which are:

$$\frac{\partial^2 g}{\partial\sigma_i\partial\sigma_j} = \begin{bmatrix} \partial^2 g/\partial p^2 & \partial^2 g/\partial p\partial q \\ \partial^2 g/\partial q\partial p & \partial^2 g/\partial q^2 \end{bmatrix} = \frac{2}{M^2 p}\begin{bmatrix} \eta^2 & -\eta \\ -\eta & 1 \end{bmatrix} \tag{5-18}$$

Note that all derivations are performed with respect to stress invariants.

5.1.4
Yield function derivatives

In order to build up the Newton-Raphson predictor, the calculation of yield function derivatives must be performed considering associated flow. Therefore:

$$\frac{\partial F}{\partial \sigma_i} = \frac{1}{p_0}\frac{\partial g}{\partial \sigma_i}, \qquad \frac{\partial F}{\partial p_0} = -\frac{p_e}{p_0^2} \tag{5-19}$$

5.1.5
Hardening rule

As aforementioned, p_0 is the hardening parameter, function of viscoplastic volumetric strain. This means that, in general, the hardening rule is expressed in terms of viscoplastic strains. By replacing them with elastic strains, the rule becomes:

$$p_0^{t+\Delta t} = p_{0,1}\, e^{\epsilon_v^{vp}/(\lambda^* - \kappa^*)} = p_{0,1}\, e^{(\epsilon_v - \epsilon_v^e)/(\lambda^* - \kappa^*)} \tag{5-20}$$

therefore, the partial derivatives with respect to elastic strains are:

$$\frac{\partial p_0}{\partial \epsilon_v^e} = -\frac{p_0^{t+\Delta t}}{\lambda^* - \kappa^*} \tag{5-21}$$

For a given strain increment, the hardening parameter can be analytically calculated as (Borja and Lee, 1990):

$$p_0^{t+\Delta t} = p_0^t\, e^{(\Delta\epsilon_v - \Delta\epsilon_v^e)/(\lambda^* - \kappa^*)} \tag{5-22}$$

5.1.6
Integration in the space of triaxial invariants

For the Modified Cam Clay, the return map can be performed in the space of (p, q) invariants thanks to a particular feature resulting from plastic potential. As illustrated by Kojic and Bathe (2005)[Chap. 6], recalling the classic elastic predictor/plastic corrector scheme, the following equation can be written for the deviatoric stress components:

$$s_i^{t+\Delta t} = s_i^e - \Delta\lambda\, 2\bar{G} \frac{\partial g}{\partial s_i}^{t+\Delta t} \tag{5-23}$$

The flow rule with respect to deviatoric stress components can be calculated applying the chain rule:

$$\frac{\partial g}{\partial s_i} = \frac{\partial g}{\partial p}\frac{\partial p}{\partial s_i} + \frac{\partial g}{\partial q}\frac{\partial q}{\partial s_i} \tag{5-24}$$

noting that $\frac{\partial q}{\partial s_i} = \frac{3 s_i}{2q}$ and $\frac{\partial p}{\partial s_i} = 0$, one obtains:

$$\frac{\partial g}{\partial s_i}^{t+\Delta t} = \frac{3}{M^2} \cdot \frac{s_i^{t+\Delta t}}{p^{t+\Delta t}} \tag{5-25}$$

that substituted in the elastic predictor/plastic corrector formula (Eq. 5-23) yields:

$$s_i^{t+\Delta t} = \frac{M^2}{M^2 + 6\bar{G}\Delta\lambda / p^{t+\Delta t}}\, s_i^e \tag{5-26}$$

This means that the viscoplastic correction has to provide only the means stress $p^{t+\Delta t}$ and the plastic multiplier $\Delta\lambda$ at the end of the time step. Final deviatoric stress components are computed by "scaling" the corresponding (deviatoric) elastic predictor.

For completeness, algorithm 2 provides all the necessary calculation steps to integrate the constitutive model, accounting for non-linear elasticity.

5.2
R-Soil: a constitutive model for soil and rock

R-Soil (Rock and Soil Model) was developed throughout this doctoral research. It is a constitutive model for both soil and rock. The main feature of R-Soil is that it accounts for non-associated flow rule, intermediate stress influence, structure degradation, metastable behavior, soil sensitivity, weathering, chemical attack and static liquefaction.

This model uses concepts from Critical State Theory (Schofield and Wroth, 1968; Wood, 1990), Single Hardening model (Kim and Lade, 1988; Lade and Kim, 1988), CASM model (Yu, 1998), and bonded soil model (Gens and Nova, 1993; Lagioia and Nova, 1995; Nova et al., 2003) for describing the general material response under various loading conditions.

5.2.1
Elastic Deformations

Recoverable elastic strains are calculated from isotropic elasticity according to the general elastic stress-strain relationship:

$$\left\{ \begin{array}{c} d\epsilon_p^e \\ d\epsilon_q^e \end{array} \right\} = \left[\begin{array}{cc} 1/K & \\ & 1/3G \end{array} \right] \left\{ \begin{array}{c} dp \\ dq \end{array} \right\} \tag{5-27}$$

as in the Cam-clay models, the elastic bulk modulus (K) and shear modulus (G) are functions of mean effective stress and related through a constant Poisson's ratio (ν).

5.2.2
Failure Criterion

Failure is assumed to occur when the soil reaches the critical state:

$$q = M\,p \tag{5-28}$$

The above expression has been generalized for three dimensional stress space by setting the slope of the critical state line, M, as a function of Lode's angle, θ, according to the Lade-Duncan failure criterion, as suggested by Van Eekelen

Algorithm 2 Implicit numerical integration of Viscous Modified Cam Clay accounting for non-linear elasticity

```
 1: Given the previous stresses $\sigma_{ij}^t$ compute the corresponding stress invariants $p^t, q^t$
 2: Given the tensor of strain increments $\Delta\epsilon_{ij}$ compute the volumetric strain increment $\Delta\epsilon_v$
 3: Perform a purely elastic step (null viscoplastic strains):
      a. Compute the secant bulk modulus $\bar{K}$ assuming $\Delta\epsilon_v^e = \Delta\epsilon_v$
      b. Compute the trial Cartesian elastic stresses $\sigma_i^e = \sigma_i^t + \bar{D}_{ij}^e \Delta\epsilon_j$, where $\bar{D}_{ij}^e$ is the stiffness matrix in Eq. 5-9 obtained with the secant bulk modulus.
      c. Compute the corresponding stress invariants $p^e, q^e$
 4: Check the yield criterion: if $\phi(p^e, q^e) < FTOL$ , then RETURN $\sigma_{ij}^{t+\Delta t} = \sigma_{ij}^e$ and $p_0^{t+\Delta t} = p_0^t$. Otherwise, perform the viscoplastic correction.
 5: Assume as starting point for Newton-Raphson loop the trial elastic state, assigning $\Delta\epsilon_v^e = \Delta\epsilon_v$ and $\Delta\epsilon_s^e = (q^e - q^t)/3\bar{G}$. At first iteration: $p^{t+\Delta t} = p^e$, $q^{t+\Delta t} = q^e$, $p_0^{t+\Delta t} = p_0^t$
 6: Compute the viscoplastic strains $\Delta\epsilon_i^{vp} = \frac{\Delta t}{\mu}\phi^{t+\Delta t} b_i^{t+\Delta t}$
 7: Evaluate residuals $r_i = \Delta\epsilon_i - \Delta\epsilon_i^e - \Delta\epsilon_i^{vp}$ and check if the error is below a given tolerance: if $|r_i| < RTOL$ , then EXIT LOOP and go to 13.
 8: Limit the number of iterations. If counter reaches a prescribed maximum (nitMAX), integration has failed. ABORT calculations.
 9: Build the Newton-Raphson predictor $Q_{ij} = \delta_{ij} + \frac{\Delta t}{\mu}(b_i f_j + \phi B_{ij})$ with all quantities evaluated at current time $t + \Delta t$.
10: Solve the linear system* $d\epsilon^e = Q^{-1} r$ and update the elastic strains: $\Delta\epsilon_i^{e,new} = \Delta\epsilon_i^{e,old} + d\epsilon_i^e$
11: Update stress invariants and the hardening variable:
      $p^{t+\Delta t} = p^t \exp(\Delta\epsilon_v^e / k^*)$
      $q^{t+\Delta t} = q^t + 3\bar{G}\Delta\epsilon_s^e$
      $p_0^{t+\Delta t} = p_0^t \exp[(\Delta\epsilon_v - \Delta\epsilon_v^e)/(\lambda^* - \kappa^*)]$
12: Go back to 6.
13: RETURN the Cartesian stresses combining the mean stress with the deviatoric components:
      $\sigma^{t+\Delta t} = p^{t+\Delta t}\delta_{ij} + \frac{M^2}{M^2 + 6\bar{G}\Delta\lambda / p^{t+\Delta t}} s_{ij}^e$
      with $\Delta\lambda = \frac{\Delta t}{\mu}\phi^{t+\Delta t}$
```

* Since the integration is performed in the space of invariants, only a 2x2 linear system has to be solved. For a very general non-associative anisotropic elasto-plastic material, the system may become 6x6 because integration must comprise all tensorial components. This means that the second derivatives of plastic potential generate a 6x6 matrix that may not be easy to compute.

(1980):

$$M = M_c \left(\frac{1 - B}{1 + B \sin 3\theta} \right)^{1/4} \tag{5-29}$$

where

$$B = 1 - \left(\frac{3}{3 + \sin \phi_c} \right)^4$$

is a model parameter that controls the curvature of the failure criterion in the octahedral plane and

$$M_c = \frac{6 \sin \phi_c}{3 - \sin \phi_c}$$

is the slope of the critical state line in triaxial compression, with ϕ_c the respective effective friction angle. According to Van Eekelen (1980), the model is convex if $B < 0.756$, that is always the case.

5.2.3 Yield surface

The R-Soil yield surface function can be expressed in terms of the conventional triaxial parameters. The contribution of Lode's angle is introduced to include the effect of third stress invariant. The yield surface is:

$$\left(\frac{q}{3p} \right)^2 \left(\frac{1 + B \sin 3\theta}{1 - B} \right)^{1/2} + \left(\frac{p}{p_0} \right)^n = 1 \tag{5-30}$$

where

$$\begin{aligned} p &= I_1/3 \\ q &= \sqrt{3J_2} \\ \sin 3\theta &= \frac{27}{2} \frac{J_3}{q^3} = \frac{J_3}{2} \left(\frac{3}{J_2} \right)^{3/2} \end{aligned}$$

The exponent n depends on the spacing ratio, $r = p_0/p_{cs}$, according to the following expression:

$$n = -\frac{\ln(1 - M_c^2/9)}{\ln r} \tag{5-31}$$

The parameter n determines the shape of the yield surface in the meridian plane and r is the spacing ratio used to control the intersection point of the critical state line and the yield surface.

The shape of the R-Soil yield surface is a teardrop and its contours, with $\phi_c = 30°, r = 4$ and $p_0 = 100$ kPa), are plotted in Figure 5.4.

During elastoplastic loading the soil is yielding and the size of the yield surface changes. The change in size of the yield locus is linked to changes in effective stresses and hardening parameters. To ensure consistency, it is necessary that the new state of stress remains on the yield surface, fulfilling

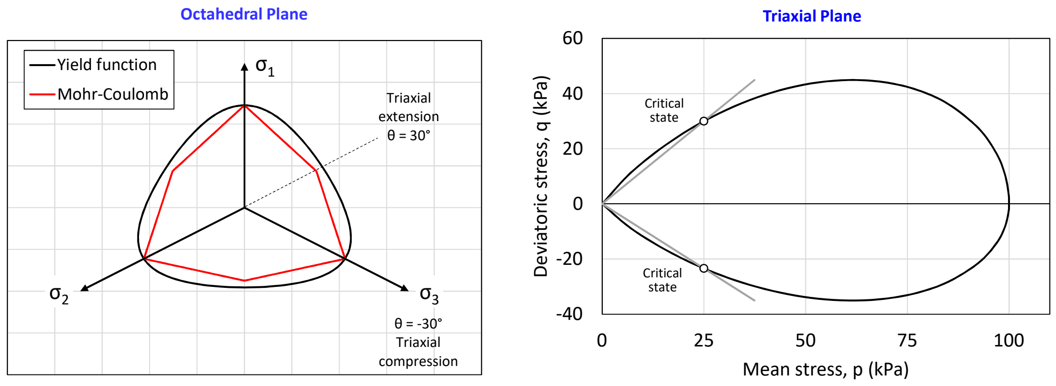

Figure 5.4: Yield function in stress space. ($\phi_c = 30°, r = 4$ and $p_0 = 100$ kPa)

the differential form of the yield function:

$$df = \frac{\partial f}{\partial \sigma_{ij}} d\sigma_{ij} + \frac{\partial f}{\partial p_0} dp_0 = 0 \tag{5-32}$$

The partial derivatives with respect to the stresses $\left(\frac{\partial f}{\partial \sigma_{ij}}\right)$ are calculated applying the chain rule to Equation 5-30, rewritten as $f(I_1, J_2, J_3)$, to obtain:

$$\frac{\partial f}{\partial \sigma_{ij}} = \frac{1}{3}\frac{\partial f}{\partial p}\frac{\partial I_1}{\partial \sigma_{ij}} + \frac{\partial f}{\partial J_2}\frac{\partial J_2}{\partial \sigma_{ij}} + \frac{\partial f}{\partial J_3}\frac{\partial J_3}{\partial \sigma_{ij}} \tag{5-33}$$

where (Crisfield, 1997)[p.105]:

$$\begin{aligned}
\frac{\partial I_1}{\partial \sigma_{ij}} &= (1, 1, 1, 0, 0, 0) \\
\frac{\partial J_2}{\partial \sigma_{ij}} &= (s_x, s_y, s_z, 2\tau_{xy}, 2\tau_{yz}, 2\tau_{zx}) \\
\frac{\partial J_3}{\partial \sigma_{ij}} &= ((s_y s_z - \tau_{yz}^2 + J_2/3), (s_x s_z - \tau_{xz}^2 + J_2/3), (s_x s_y - \tau_{xy}^2 + J_2/3), \\
&\quad 2(\tau_{yz}\tau_{xz} - s_z\tau_{xy}), 2(\tau_{xz}\tau_{xy} - s_x\tau_{yz}), 2(\tau_{xy}\tau_{yz} - s_y\tau_{xz}))
\end{aligned} \tag{5-34}$$

The derivatives of the yield function, given in Equation 5-30, can be written as:

$$\frac{\partial f}{\partial p} = \frac{n}{p}\left[1 - \frac{\eta^2}{m^2}\left(\frac{1 + B\sin 3\theta}{1 - B}\right)^{1/2}\right] \tag{5-35}$$

$$\frac{\partial f}{\partial J_2} = \frac{1 + \frac{1}{4}B\sin 3\theta}{3p^2\sqrt{1 - B}\sqrt{1 + B\sin 3\theta}} \tag{5-36}$$

$$\frac{\partial f}{\partial J_3} = \frac{9B/4q}{3p^2\sqrt{1 - B}\sqrt{1 + B\sin 3\theta}} \tag{5-37}$$

$$\frac{\partial f}{\partial p_0} = -\frac{n}{p_0}\left(\frac{p}{p_0}\right)^n \tag{5-38}$$

where $m = 3\sqrt{\frac{n}{2+n}}$. A value of B equal to zero in the above expressions gives back their original form, as they were conceived in triaxial compression. In this special case, the yield function becomes symmetric with respect the hydrostatic axis (i.e. a circle in the octahedral plane) and the failure occurs according to Von Mises's criterion.

5.2.4
Plastic Potential

The following expression is assumed for the stress-dilatancy relation:

$$d = \frac{(M^2 - \eta^2)(\eta^2 + \psi)}{\beta\eta} \tag{5-39}$$

imposing the tension cut-off condition, $d(\eta = 3) = -3$, it gives:

$$\beta = -\frac{1}{9}(M^2 - 9)(9 + \psi) \tag{5-40}$$

meaning that only two independent parameters are needed to fully describe the plastic flow rule. As shown by Lagioia and Nova (1995), the related plastic potential can be obtained by substitution of Equation 5-39 into the differential equation:

$$\frac{dp}{p} = -\frac{d\eta}{d + \eta} \tag{5-41}$$

whose integration gives the mathematical expression for the plastic potential:

$$g : \left(\frac{\psi_1 + \eta^2}{\psi_2 - \eta^2}\right)\left(\frac{p}{p_0}\right)^{\mu} = \frac{\psi_1}{\psi_2} \tag{5-42}$$

that is a simplified version of the plastic potential proposed by Kim and Lade (1988). It is possible to demonstrate the existence of simple relations between parameters (M, ψ, β) and (ψ_1, ψ_2, μ):

$$\psi_1 = \frac{M^2\psi}{9} = \frac{1}{2}\left[\sqrt{(M^2 + \beta - \psi)^2 + 4M^2\psi} - (M^2 + \beta - \psi)\right] \tag{5-43}$$

$$\psi_2 = 9 = M^2 + \beta - \psi + \psi_1 \tag{5-44}$$

$$\mu = \frac{2}{\beta}\left(\frac{M^2\psi}{9} + 9\right) = \frac{2}{\beta}(\psi_1 + \psi_2) \tag{5-45}$$

These identities allow to calibrate the plastic potential parameters directly from the stress-dilatancy relation.

The first derivatives of plastic potential are:

$$\begin{cases} \dfrac{\partial g}{\partial p} = \psi_1(2 + \mu)\, p \left(\dfrac{p}{p_0}\right)^{\mu} + \mu\dfrac{q^2}{p}\left(\dfrac{p}{p_0}\right)^{\mu} - 2\psi_1 p \\ \dfrac{\partial g}{\partial q} = 2q\left(\dfrac{p}{p_0}\right)^{\mu} + 2\dfrac{\psi_1}{\psi_2}q \end{cases} \tag{5-46}$$

If a backward Euler return is chosen for stress integration, the calculation of second partial derivatives is necessary to perform numerical iterations:

$$\begin{cases} \dfrac{\partial^2 g}{\partial p^2} = \psi_1(2+\mu)(1+\mu)\left(\dfrac{p}{p_0}\right)^{\mu} + \mu(\mu-1)\dfrac{q^2}{p^2}\left(\dfrac{p}{p_0}\right)^{\mu} - 2\psi_1 \\ \dfrac{\partial^2 g}{\partial q^2} = 2\left(\dfrac{p}{p_0}\right)^{\mu} + 2\dfrac{\psi_1}{\psi_2} \\ \dfrac{\partial^2 g}{\partial p \partial q} = 2\mu\dfrac{q}{p}\left(\dfrac{p}{p_0}\right)^{\mu} \end{cases} \tag{5-47}$$

where

$$\left(\frac{p}{p_0}\right)^{\mu} = \frac{\psi_1}{\psi_2}\cdot\frac{\psi_2 - \eta^2}{\psi_1 + \eta^2}$$

can be substituted in the previous expressions to avoid the evaluation of p_0.

The shapes of R-Soil plastic potential with different values of M and ψ are plotted in Figures 5.5 and 5.6. The parameter M controls the stress ratio corresponding to critical state (as in Cam Clay models), while ψ is a parameter related to dilatancy and K_0-condition. The shape of the plastic potential is assumed to be a circle in the deviatoric plane. This means that the partial derivative of the plastic potential with respect to the Lode's angle is implicitly set to zero, i.e. $\partial g/\partial\theta = 0$. However, the slope of critical state line, M, must be updated according to Equation 5-29, in order to correctly predict dilatancy depending on state of stress.

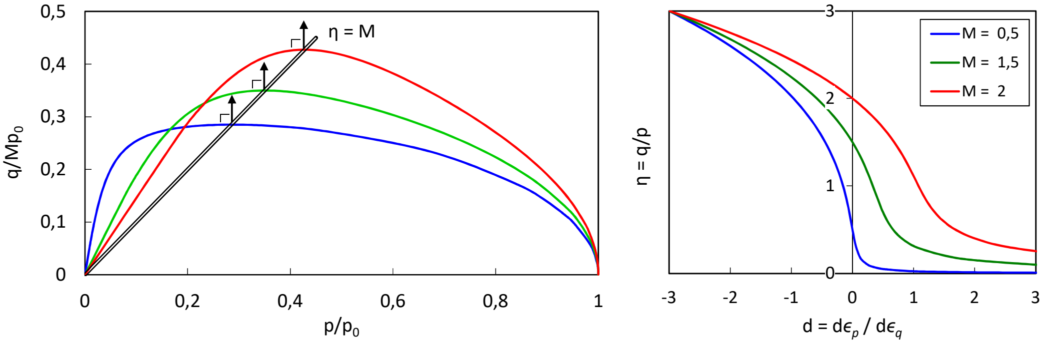

Figure 5.5: Contours of plastic potential and corresponding stress-dilatancy relations with $\psi = 1$ and varying M.

5.2.5
Destructuration behavior

The fundamental hypothesis to model the destructuration of structured soils and weathered rocks is to make the size of yield surface dependent on a set of constitutive parameters sensitive to chemical weathering and mechanical

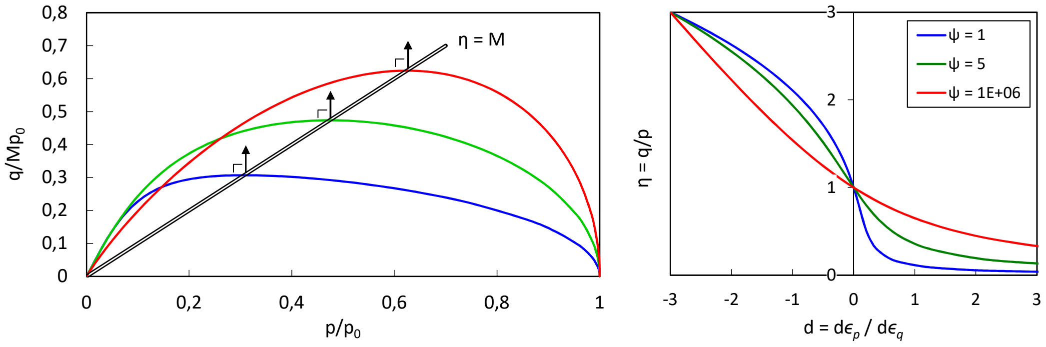

Figure 5.6: Contours of plastic potential and corresponding stress-dilatancy relations with $M = 1$ and varying ψ.

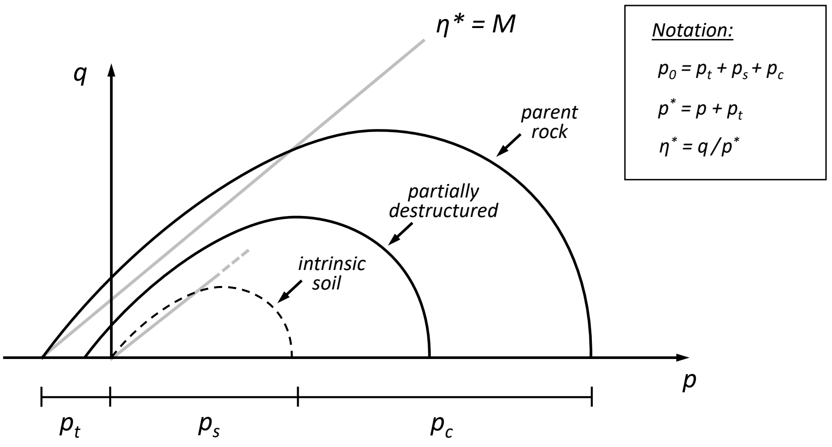

Figure 5.7: Evolution of yield surface during destructuration. Adapted from Nova et al. (2003).

damage. In this sense, the conventional preconsolidation pressure is assumed to be the sum of three contributions, $p_0 = p_t + p_c + p_s$, associated to the tensile, compressive and intrinsic soil strength. As shown in Figure 5.7, those parameters are responsible for enlarging and shrinking the yield locus (Gens and Nova, 1993) according to predetermined hardening and softening laws, based on plastic strains and degree of weathering (Castellanza and Nova, 2004).

The expression of the yield function is, therefore, modified to account the new hardening parameters:

$$\left(\frac{\eta^*}{3}\right)^2 + \left(\frac{p^*}{p_0}\right)^n = 1 \tag{5-48}$$

where $p^* = p + p_t$, $p_0 = p_t + p_s + p_c$ and $\eta^* = q/p^*$.

A particular choice is made when compressive and tensile strength are set proportional to each other, by assuming a constant factor, $R = (p_c/p_t)$, usually between 10 and 20 (Nova, 2005). In this case, it is postulated that the size of the yield function is controlled only by two variables, p_s and p_t, with:

$p_s =$ internal variable related to soil hardening. It acts as common strain hardening parameter for the intrinsic soil matrix and is affected only by plastic strain history.

$p_t =$ internal variable related to the interparticle bonds and cementation, suffering mechanical damage and chemical weathering from combined physical actions and chemical agents.

Enforcing the consistency rule, that is $df = 0$:

$$df = \frac{\partial f}{\partial p^*}dp + \frac{\partial f}{\partial q}dq + \frac{\partial f}{\partial p_0}dp_s + \left[\frac{\partial f}{\partial p^*} + \frac{\partial f}{\partial p_0}(1+R)\right] dp_t = 0 \qquad (5\text{-}49)$$

it follows that

$$\frac{\partial f}{\partial p} = \frac{\partial f}{\partial p^*} \qquad (5\text{-}50)$$

$$\frac{\partial f}{\partial p_s} = \frac{\partial f}{\partial p_0} \qquad (5\text{-}51)$$

$$\frac{\partial f}{\partial p_t} = \frac{\partial f}{\partial p^*} + \frac{\partial f}{\partial p_0}(1+R) \qquad (5\text{-}52)$$

5.2.6
Hardening law

The yield surface size of the soil matrix is governed by the preconsolidation pressure (p_s), which is taken as one of the hardening parameters and is related to both plastic volumetric and plastic deviatoric strains as stated by the *hardening law*:

$$dp_s = \frac{\partial p_s}{\partial \epsilon_p^{\mathrm{p}}}d\epsilon_p^{\mathrm{p}} + \frac{\partial p_s}{\partial \epsilon_q^{\mathrm{p}}}d\epsilon_q^{\mathrm{p}} \qquad (5\text{-}53)$$

It is well understood that whilst volumetric hardening models are normally sufficient to describe the behaviour of clays, it is necessary to additionally introduce shear hardening to model the observed behaviour of sands (Nova and Wood, 1978, 1979). Then, the hardening law can be written as follows:

$$\frac{\partial p_s}{\partial \epsilon_p^{\mathrm{p}}} = \frac{p_s}{\lambda^* - \kappa^*} \qquad (5\text{-}54)$$

$$\frac{\partial p_s}{\partial \epsilon_q^{\mathrm{p}}} = B_q \frac{p_s}{\lambda^* - \kappa^*} \qquad (5\text{-}55)$$

where λ^* and κ^* are the modified loading/unloading indexes, and B_q is the parameter controlling the deviatoric hardening.

5.2.7
Softening law

The *softening law* sets the consequences of mechanical damage and chemical weathering on interparticle bonds (Lagioia and Nova, 1995; Castellanza and Nova, 2004):

$$p_t = p_{t0}(1 - X_d)^C \, e^{-\omega \, \epsilon^{\mathrm{d}}} \tag{5-56}$$

where ϵ^{d} is a suitable destructuring plastic strain and X_d is the degree of chemical weathering, a scalar varying between 0 and 1, that maps the transition from hard rock ($X_d = 0$) to totally weathered soil ($X_d = 1$). The parameter ω controls the destruction rate of bonds. The differential form of the softening law establishes the evolution of the parameter p_t:

$$dp_t = -p_t \left[\omega d\epsilon^{\mathrm{d}} + \frac{C}{1 - X_d} \, dX_d \right] \tag{5-57}$$

According to Koliji et al. (2008), mechanical degradation is controlled by a suitable *destructuring strain*, a general plastic strain that, depending on loading condition, can be volumetric, deviatoric or a combination of both:

$$d\epsilon^{\mathrm{d}} = (1 - B_d) \| d\epsilon_p^{\mathrm{p}} \| + B_d \, d\epsilon_q^{\mathrm{p}} \tag{5-58}$$

where B_d acts as damage weighting factor.

5.2.8
Model parameters and their identification

It can be seen that there are a total of 10 model constants required in R-Soil, all of which can be determined in the laboratory. They are λ^*, κ^*, ν, M, ψ, r, B_q, ω, B_d and R. It is desirable to have a number of laboratory tests under different stress paths and confining pressures to evaluate reliable values of material constants.

- The elastic behavior is modelled by the Poisson' ratio (ν) and the slope of the swelling line (κ^*).
- The critical state line is defined by the critical state parameter (M) in triaxial compression. The curvature of the plastic potential is controlled by ψ, that has consequences on dilatancy and K_0-condition. From the stress-dilatancy relationship (Eq. 5-39), one can derive the expression relating the K_0-condition and the dilatancy parameter (ψ):

$$\psi \approx \frac{3}{2} \left(1 - \frac{\kappa^*}{\lambda^*} \right) \frac{\beta \eta_{K_0}}{M^2 - \eta_{K_0}^2} - \eta_{K_0}^2$$

where $\eta_{K_0} = \frac{3(1-K_0)}{1+2K_0}$ is the stress ratio corresponding to virgin loading in oedometric compression.

- The spacing ratio (r) is used to locate the critical state along the yield function. In the original and modified Cam Clay models, r is fixed at 2,718 and 2, respectively. As in CASM model (Yu, 1998), the assumption of a variable r is adopted.
- Isotropic hardening is controlled by the modified compression index (λ^*). Deviatoric hardening is introduced by setting $B_q \neq 0$.
- The parameters ω, B_d and R are related to bonds degradation.

The code requires six non-null parameters $(\lambda^*, \kappa^*, \nu, M, \psi, r)$ related to the *critical state model.* The remaining entries introduce, to the model, the deviatoric hardening and the bonds degradation. It is advisable to make a "rough" calibration with the first six parameters and, only then, add more complexity, introducing additional parameters. Again, the spacing ratio (r) controls the position of the critical state on the yield surface. The deviatoric hardening coefficient (B_q) produces hardening at critical state. In author's opinion, both parameters can be easily visualized with a series of undrained triaxial compression tests run at different confining pressures. Bonds degradation parameters $(\omega,\ B_d,\ R)$ are calibrated similarly to Lagioia and Nova (1995). At the end of the day, a specific experimental procedure has to be adopted to determine all model parameters.

5.3
Implementation in Plaxis

In this section, an algorithm is presented for the implementation of soil constitutive models in finite element (FE) analysis, based on the displacement approach. Plaxis has a facility that allows to implement a user-defined soil model (UDSM) into the finite element code. This requires programming a Fortran subroutine that must be compiled into a Dynamic Link Library (DLL) and then added to the Plaxis program directory.

The compilers employed to make the DLL file were `g95` or MinGW (`https://www.g95.org/`) and `gfortran` or GNU Fortran `gfortran` (`https://gcc.gnu.org/`). G95 was used to make the 32-bit DLL file with the following command:

```
g95 usrmod.for -o usrmod.dll -shared -fcase-upper -fno-underscoring
-mrtd
```

GNU Fortran (GFortran) was used to make the 64-bit DLL file with the following command:

```
gfortran usrmod.for -o usermod64.dll -shared -fno-underscoring
-static
```

The USDM is called at Gauss-points to return the stress increment according to the constitutive equations of the model. Plaxis provides information about the previous stresses, pore pressure and state variables, and also strain and time increments:

σ_i^t	`Sig0(6)`	array with previous stresses
p_w^t	`Swp0`	previous pore pressure
h_k^t	`StVar0(*)`	array with previous state variables
Δt	`dTime`	time increment
$\Delta\epsilon_j$	`dEps(6)`	array with strain increments

The user-defined subroutine returns the updated constitutive stresses, pore pressures, state variables and material stiffness matrix:

$\sigma_i^{t+\Delta t}$	`Sig(6)`	array with updated stresses
$p_w^{t+\Delta t}$	`Swp`	updated pore pressure
$h_k^{t+\Delta t}$	`StVar(*)`	array with updated state variables
D_{ij}	`D(6,6)`	material stiffness matrix

The subroutine is governed by an input parameter to the subroutine, the `IDTask`-parameter. There are six `IDTask` defined. For each, PLAXIS assigns different tasks that the global calculation needs at different stages in the calculation process:

`IDTask`	Task description
1	Initialize state variables
2	Integrate constitutive relations (`Sig(6)`,`StVar(*)` and `Swp`)
3	Create `D(6,6)` (tangent material stiffness matrix)
4	Return the number of state variables
5	Inquire Matrix attributes `NonSym, iStrsDep, iTimeDep, iTang`
6	Create `De(6,6)` (elastic material stiffness matrix)

5.3.1
Main subroutine

The structure of the main subroutine is designed to manage the six IDTasks independently of the chosen constitutive model. After declaring the properties inherent to the constitutive model stored in the array `Props` (which allows max. 50 entries), the subroutine is comprised by the following tasks:

Task #1. In IDTask 1, state variables are initialized. When starting a new calculation phase, the initial value of the state variables is read from the output file of the previous calculation step. However, in the very first calculation step, the `STVar0` should be initialized, otherwise it would contain only zeros. In this case, the Task #1 generates the initial value of the state variables based on the actual stress state at the beginning of the step. The equivalent stress (p_{eq}) is calculated from the initial effective stress state generated using the K_0-condition. Based on the shape of the yield surface, the user defines the expression for p_{eq} and the initial value of the equivalent overconsolidation ratio. Then, the preconsolidation pressure is calculated simply as $p_0 = p_{eq} \cdot OCR$.

Task #2. In IDTask 2, the constitutive stresses are calculated with an automatic substepping algorithm (Sloan, 1987; Sloan et al., 2001) to stabilize stress integration. Substepping starts with applying a subincrement equal to the total strain increment and calling an external subroutine, the so-called *stress integrator*, to integrate stresses and hardening variables according to backward (implicit) or a forward (semi-implicit) Euler schemes. If integration fails, the size of the subincrement is reduced and the procedure continues until the total strain increment is applied (see Algorithm 3).

Moreover, under undrained conditions (i.e. if `IsUndr`=1), changes in pore water pressure are calculated from the equivalent bulk stiffness and the total volumetric strain increment:

$$\begin{aligned} \Delta p_w &= K_f \, \Delta\epsilon_v \\ K_f &= K_u - K' = \frac{2G}{3}\left(\frac{1+\nu_u}{1-2\nu_u} - \frac{1+\nu'}{1-2\nu'}\right) \end{aligned}$$

The bulk modulus of the soil under undrained condition (K_u) is calculated using the undrained Poisson's ratio $\nu_u = 0.495$.

Control of substepping procedure is made by using two indicators. The first is the plasticity indicator `ipl` (for output purpose). According to Plaxis manual, `ipl`=0 for elastic points, `ipl`=1 for plastic points and `ipl`=2 for tension cut-off points. The second is the user-defined `iConv` (convergence flag). This control variable allows the substepping algorithm to recognize if the stress integration has succeeded (`iConv`

= 1) or failed (`iConv` = 0) within a prescribed number of iterations (`nitMAX`=15) given a specified tolerance (`TOL`=1e-9).

Task #3. and #6. In IDTask 3, the material stiffness matrix (D) is created. It may contain only the elastic components of the stress-strain relationship (as it is the case for the existing soil models in Plaxis) or the full elastoplastic material stiffness matrix (tangent stiffness matrix). The models that have been implemented do not use a tangent stiffness matrix, which means that both IDTask 3 and IDTask 6 return the elastic material stiffness matrix of the current stress point. In any case, the elastic tangent (instantaneous) stiffness is considered.

If undrained behavior is considered (`isUndr`=1), then a bulk stiffness for water (`BulkW`) must be specified at the end of Task 3. Plaxis will automatically add the stiffness of water to the stiffness matrix (see Naylor and Pande, 1981; Potts and Zdravkovic, 1999).

Task #4. This task allows the program to know the number of state variables by means of the parameter `nStat`.

Task #5. Task 5 returns the matrix attributes. Four attributes need to be declared:

1. `NonSym` indicates if the material stiffness matrix is symmetrical. For `NonSym`=0 only one half of the global stiffness matrix is stored, whereas for `NonSym`=1 the full matrix is stored.
2. `iStrDep` indicates if the material stiffness matrix is stress-dependent. For `iStrDep`=1 the stiffness matrix is created and decomposed at the beginning of each calculation step based on the actual stress state.
3. `iTimeDep` indicates if the stiffness is time-dependent. For `iTimeDep`=1 the stiffness matrix is created and decomposed when the time step changes.
4. `iTang` indicates if the tangent stiffness matrix is utilized in global finite element Newton-Raphson procedure. If the elastic stiffness is employed as N-R predictor, one should declare `iTang`=0.

5.3.2
Automatic substepping

Constitutive equations are integrated over the time interval Δt assuming that strain rates are constant throughout the time interval. Substepping with error control (Sloan, 1987; Sloan et al., 2001) is adopted in this implementation. The "dimensionless time" is introduced, a scalar quantity such that $T(t) = 0$ and $T(t + \Delta t) = 1$. Considering a pseudo time increment ΔT_n, the corresponding strain subincrement is $\{\Delta\epsilon_n\} = \Delta T_n \{\Delta\epsilon\}$, and the values for the stresses $\{\sigma\}$ and hardening variables $\{k\}$ at the end of ΔT_n are:

$$\{\sigma_n\} = \{\sigma_{n-1}\} + \{\Delta\sigma_n\}$$
$$\{k_n\} = \{k_{n-1}\} + \{\Delta k_n\}$$

The current strain subincrement $\{\Delta\epsilon_n\}$ is rejected if the residual norm (R_n) is greater than a prescribed tolerance (`TOL`) within a defined maximum number of iterations (`nitMAX`). If so, the size of the subincrement is automatically reduced and new substeps are repeated until $T = 1$. The complete substepping integration algorithm is presented in details in Algorithm 3 and in flowchart 5.8.

Algorithm 3 Automatic substepping algorithm

```
1: Get the previous information at the start of time increment:
   Read $\{\sigma^t\}$ Sig0 , $\{k^t\}$ StVar0, $\Delta t$ dTime, $\{\Delta\epsilon\}$ dEps
2: Assume $T_0 = 0$ and $\Delta T_1 = 1$, then $\{\Delta\epsilon_1\} = \Delta T_1\{\Delta\epsilon\}$
3: Call the stress integrator subroutine to compute updated $\{\sigma_n\}$ and $\{k_n\}$.
   If the stress integrator fails to converge, try with a smaller substep
   $\Delta T_n = q \cdot \Delta T_n$ where $q = \max\{0.8\sqrt{\frac{TOL}{R_n}}, 0.1\}$.
4: Repeat until the subincrement is successful. Update stresses and state
   variables:
   Sig←Sig_n    StVar←StVar_n
5: Estimate a new subincrement size $q = \min\{0.8\sqrt{\frac{TOL}{R_n}}, 2.0\}$ and then set
   $\Delta T_{n+1} = q \cdot \Delta T_n$.
6: Before returning to step 3, update time and check that integration does
   not proceed beyond $t + \Delta t$:
       $T = T + \Delta T_n$
       $\Delta T_{n+1} = \min\{\Delta T_{n+1}, 1 - T\}$
7: Exit with stresses $\{\sigma^{t+\Delta t}\}$ and state variables $\{k^{t+\Delta t}\}$ at the end of time
   step.
```

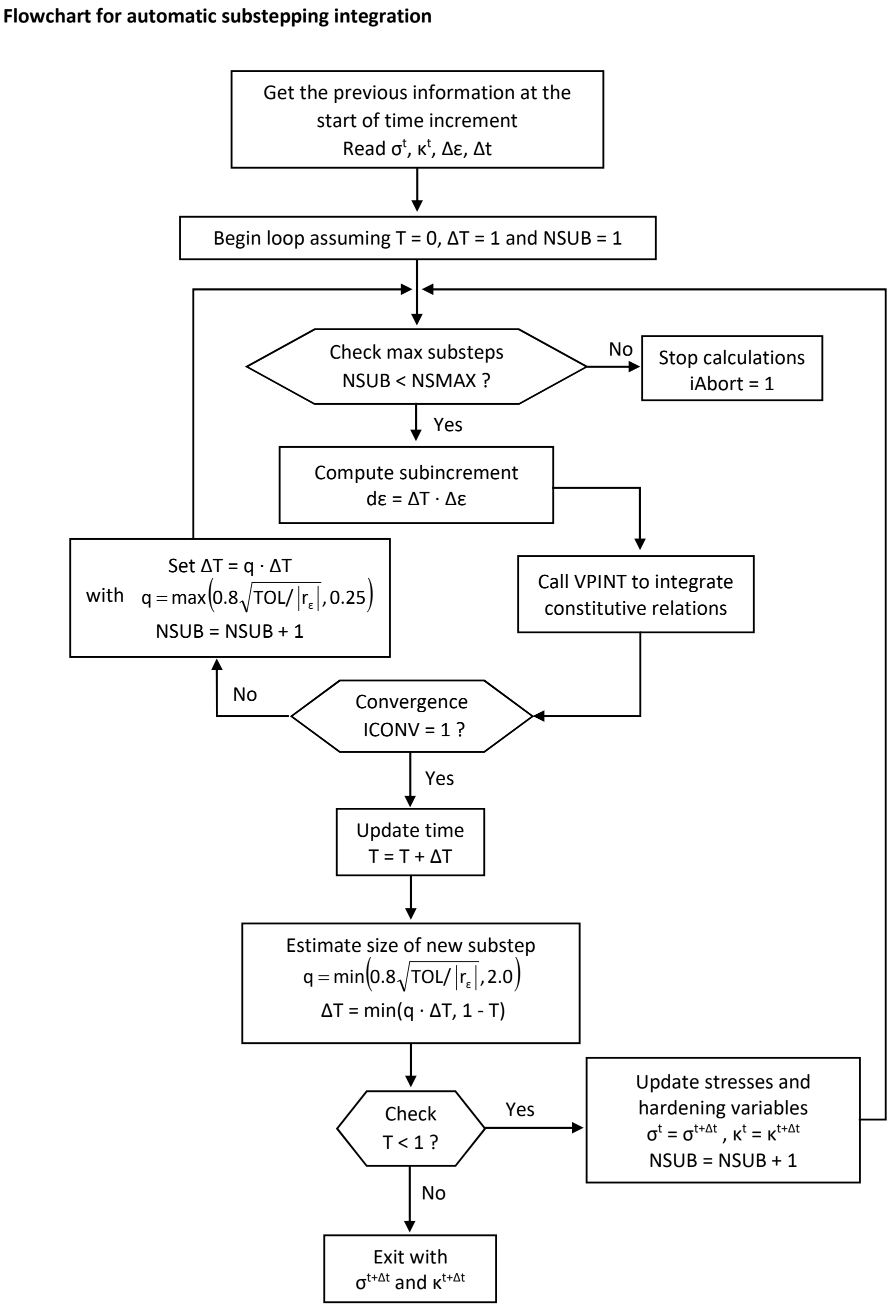

Figure 5.8: Flowchart for automatic substepping integration.

6
Application of advanced soil models to tropical soils

6.1
Laboratory behavior of Sarapuí soft clay using the finite element method

Creep and consolidation substantially influence the mechanical behavior of clay soils. They influence each other, too. Long-term deformations caused by these processes may be expressive and difficult to quantify. Moreover, though related, such phenomena have very distinct origin.

Soil deforms under chemical, thermal and mechanical effects. As instance, it is known that it can expand/shrink due to changes of salt content in interstitial fluid, temperature variations or by changing the state of effective stresses.

Strains occurring instantaneously, and proportionally to the variation of the effective stress state, are called "elastic". Those occurring subsequently, and over time, are called "viscous" ("viscoelatic" or "viscoplastic"). Therefore,creep is considered herein as the viscous phenomenon of mechanical nature, which produces time-dependent inelastic deformations after loading the material.

Consolidation is understood only as the process of dissipation of excess pore pressure that generates a variation in the state of effective stresses. Its duration essentially depends on the permeability, compressibility and the drainage condition (boundary condition) of the soil. For this reason, deformations induced by the consolidation can be elastic, viscoplastic or a combination of both.

Creep can be observed in all materials, whether crystalline, fibrous, granular or polymeric. In metals and polymers, for example, the effective stress is equal to the total stress because there is no fluid phase. In saturated soils, for stresses below 1 MPa, according to the principles of soil mechanics, the effective stress was defined by Terzaghi (1943):

$$\sigma' = \sigma - u \tag{6-1}$$

from now on, this definition will be adopted to describe the behavior of soil. Elastic strains will occur due to effective stress variations:

$$\dot{\epsilon}^e_{ij} = C_{ijkl}\,\dot{\sigma}'_{kl} \tag{6-2}$$

where C_{ijkl} is the compressibility tensor. On the other hand, viscoplastic strains will be activated by means of a yield criterion, $f(\sigma'_{ij}, h_k)$, being their direction given by the flow rule:

$$\dot{\epsilon}_{ij}^{vp} = \dot{\lambda}\frac{\partial g}{\partial \sigma_{ij}} \qquad \text{(6-3)}$$

where λ is the so-called plastic multiplier, a scalar that quantifies plastic strains (i.e. the module of $\dot{\epsilon}_{ij}^{vp}$), whereas $\frac{\partial g}{\partial \sigma_{ij}}$ gives the direction. The way λ is calculated will determine the evolution of viscoplastic strains. Models that can be adopted are those proposed by Perzyna (1963, 1966), Duvaut and Lions (1972) and Wang et al. (1997).

6.1.1
Viscous behavior of Sarapuí clay

Samples of soft fluvial-marine clay from Sarapuí experimental site have been widely used for theoretical and experimental studies by Brazilian researchers. Almeida and Marques (2003) provide a summary of laboratory and in situ tests carried out in the last 30 years at the Sarapuí site, describing the clay in terms of its geological origin, index properties, stress history, compressibility, consolidation and strength properties, and viscous behaviour, a feature here addressed in details. The large number of tests carried out allowed to establish important experimental evidences, which led to the conclusion that Sarapuí clay has a marked viscous behavior, whose characteristics can be summarized as follows:

1. Secondary compression is caused by creep, with deformations that develop under constant effective stress.

2. During secondary compression the lateral earth pressure coefficient K_0 increases gradually until it stabilizes within a region of indifferent equilibrium.

3. At lower load increment ratios, the effect of secondary compression is predominant in the development of deformation. By increasing the loading ratio ($\Delta\sigma/\sigma$), the importance of secondary compression becomes smaller compared to the primary consolidation.

4. The residence time of the previous loading influences the soil response in the next loading stage.

5. If during a test all deformations are interrupted (there is no volume variation or distortion), the soil undergoes stress relaxation. Effective stresses "relax", that is, decrease.

6. If the total stress is kept constant during the relaxation phase, the reduction in the effective stress corresponds to an equal increase in pore pressure, called excess.

7. The higher the rate of deformation, the greater the resistance mobilized under loading.

A list of selected researches at COPPE/UFRJ on the rheological behaviour of saturated clays is given in Table 6.1.

Table 6.1: Summary of the main experimental studies.

Author	Tests	Purpose
Vieira (1988)	Long-term conventional oedometer test	Observe the influence of load increment ratio $\Delta\sigma/\sigma$ on the development of consolidation curves
Carvalho (1989)	Constant rate of strain oedometer test	Establish a standard experimental procedure
Feijó (1991)	Long-term conventional oedometer test	Observe long-term behavior of samples subjected to different OCRs
Lima (1993)	Stress-controlled oedometer test with bottom pore pressure measurement	Monitor pore pressures during consolidation and stress relaxation under undrained conditions
Garcia (1996)	Conventional oedometer test with relaxation stages	Show that that both stress relaxation and secondary compression proceed towards the line of end of secondary
Guimarães (2000)	Undrained triaxial creep	Study porepressures and strains during the secondary and tertiary creep
Aguiar (2014)	Undrained hydrostatic relaxation test	Monitor the increase in porepressure during the relaxation process under constant total hydrostatic stress and undrained conditions

6.1.2
Numerical simulations

Numerical simulations were performed using Plaxis 2D finite element software. Figure 6.1 shows the axisymmetric finite element mesh used to simulate the conventional and CRS consolidation tests. Model dimensions and assumed boundary conditions are briefly discussed. There are 14 elements, 145 nodes and 168 integration points. The model consist of a soil column with a

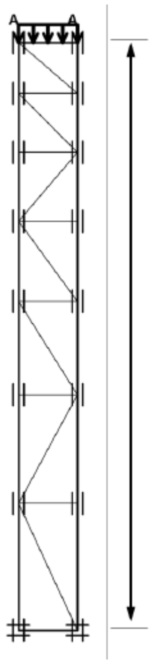

Figure 6.1: Finite element mesh used for numerical simulation of consolidation tests on Sarapuí clay.

load and/or a prescribed displacement on its top. Evidently, the prescribed displacement on the top of the sample is used to simulate constant strain rate tests, as shown hereafter. Drainage is allowed only from the upper face. In all cases, the height of the column is equal to the drainage path (Hd). In the edometric consolidation tests with bottom pore pressure measurement, the drainage path is Hd = 2 cm instead of Hd = 1 cm, the latter value being used for conventional edometric tests.

The elongated mesh used in the numerical analyses is justified by the nature of the problem, which consists of a one-dimensional (vertical) fluid flow-coupled deformation. Consequently, horizontal displacement are avoided, but the vertical ones are free along both sides. In the laboratory, the diameter of the sample is much larger than its height to minimize the undesired effects arising from side friction. That is not the case in the numerical simulations.

The behavior of Sarapuí clay was simulated with the Viscous Modified Cam Clay constitutive model, which was implemented in Plaxis 2D through the User Defined Soil Models (UDSM) facility. To this aim, it was necessary to compile a specific routine written in FORTRAN, following the instructions provided by the Plaxis software developer himself (Brinkgreve et al., 2016). In the numerical simulations, the specific weight was kept null and *Undrained* option was selected to represent the material behavior. The constitutive model parameters used in finite element numerical simulations are shown in Table 6.2. The critical state parameters were derived from Almeida (1982, 1986). The law of variation of permeability with the void ratio follows the experimental results of Lacerda et al. (1977) *apud* Almeida and Ferreira (1992); Almeida and Marques (2003). The parameters, μ and b, related to the viscous behavior of the material were calibrated against the hydrostatic relaxation tests performed by Aguiar (2014). It is noteworthy that the fluidity parameter was determined at constant room temperature (21 °C).

Table 6.2: Adopted model parameters for Sarapuí clay.

Symbol	Description	Value
λ^*	Modified compression index	0.235
κ^*	Modified swelling index	0.025
ν	Poisson's ratio	0.20
M	Slope of critical state line	1.14
μ	Fluidity parameter	22760 days
b	Rate sensitivity index	10.73
p_0	Initial isotropic preconsolidation pressure	15 kPa
k_y	Vertical hydraulic conductivity	2×10^{-3} m/day
e_0	In-situ void ratio	4.2
c_k	Permeability reduction factor with the void ratio	1.03

*OBS: μ and b were calibrated in undrained hydrostatic relaxation.

This section will not illustrate the theoretical derivation used to interpret the undrained hydrostatic relaxation test, nor the least-squares formulation used to calibrate the viscous behavior parameters. It has been alredy done in Section 3.2.1. However, it is worth to mention that this type of test allows to observe, indirectly, the shape of the viscous nucleus down to very low viscoplastic strain rates (of the order of 5×10^{-10} s^{-1}) by monitoring the increase in pore pressure for a few days. In fact, there is a closed-form solution that allows to derive the accumulated viscoplastic volumetric strains by observing the increase of excess pore pressure over time. For an infinite time, the pore pressure excess reaches a stable maximum corresponding to the steady state condition. The value will be u_∞, which is a value to be extrapolated from the experimental data. The estimation of u_∞ depends on the length of the observation period, which in the available laboratory tests was approximately 15 days. Of course, the longer the test, the more reliable the value of u_∞ will be. For calculation purposes, the value of u_∞ was estimated by the experimental adjustment curve proposed by Aguiar (2014). The equations that describe the stress relaxation test in the undrained hydrostatic condition are reported in the following. Viscoplastic strains can be calculated as:

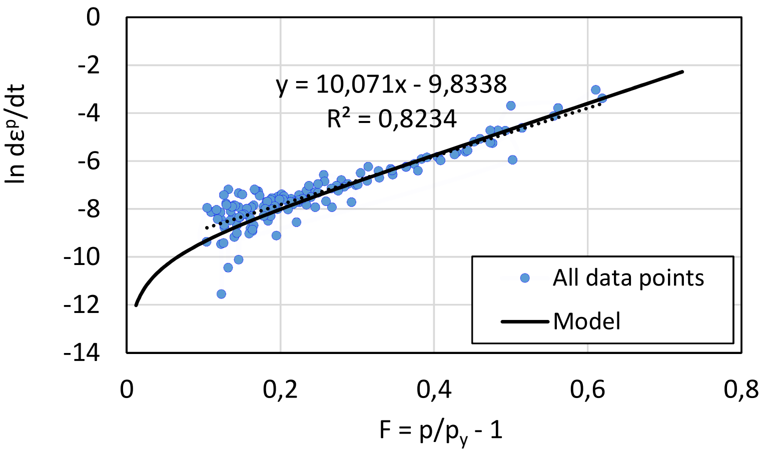

Figure 6.2: Calibration of viscous nucleus. Data points from Aguiar (2014).

$$\epsilon^p = \int_0^t \dot{\epsilon^p} dt = -\kappa^* \ln\left(1 - \frac{u}{\sigma_c}\right) \tag{6-4}$$

and the value of the preconsolidation pressure (position of the reference ellipse) is given by:

$$p_y = \sigma_c \left(1 - \frac{u_\infty}{\sigma_c}\right)^{\frac{\lambda^*}{\lambda^* - \kappa^*}} \exp\left(\frac{\epsilon^p}{\lambda^* - \kappa^*}\right) \tag{6-5}$$

Figure 6.2 shows the experimental data from tests 1.1, 2.1 and 3.1 performed by Aguiar (2014), which have been processed by means of Eqs. 6-4 and 6-5. Experimental points are well aligned, tracing an almost linear trend. Thus, one can even fit a regression line, according to a relationship such as:

$$\ln \dot{\epsilon^p} = bF - \ln \mu \tag{6-6}$$

that immediately yields $\dot{\epsilon^p} = \frac{1}{\mu} e^{bF}$, suggesting a function of the exponential type for the viscous nucleus like $\phi(F) = e^{bF}$. An inconvenient related to such an approximation is that the value of the viscoplastic strain rate does not cancel out, although it should, when the viscous nucleus is zero ($F = 0$). Then, a slight modification is done, adopting:

$$\dot{\epsilon^p} = \frac{1}{\mu}(e^{bF} - 1) \rightarrow \phi(F) = e^{bF} - 1 \tag{6-7}$$

this expression has already been proposed by different authors (see for example Fodil et al., 1997) and is considered one of the most common by Owen and Hinton (1980). The viscoplastic nucleus of the exponential type can reproduce the experimental data in an excellent way. Calibration involves two parameters, μ and b, which can be determined by least squares method or, simply, by linear regression (at least at first estimate). The calibrated viscous nucleus, with the parameters in Table 6.2, provides the predictions shown in Figures 6.2 and 6.3.

The next step was to simulate the CRS tests performed by Carvalho

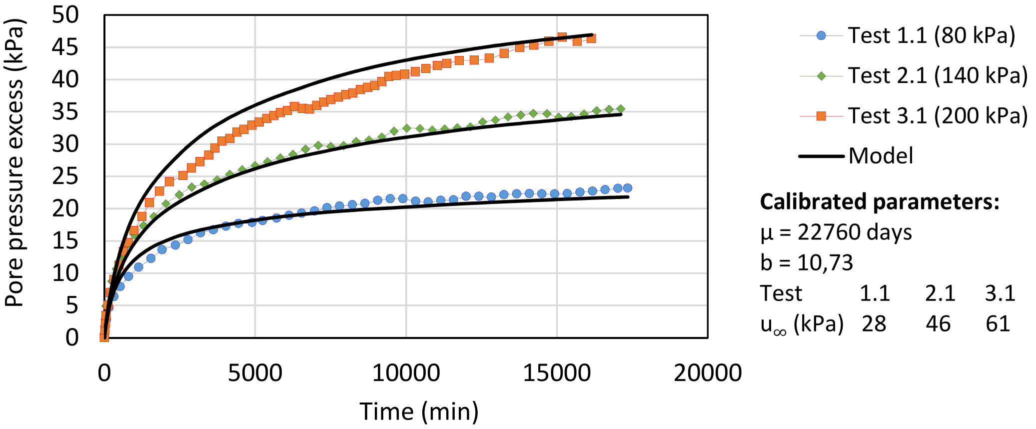

Figure 6.3: Simulated and measured increase of pore pressure after closing the drainage at the end of primary consolidation. Data points from Aguiar (2014).

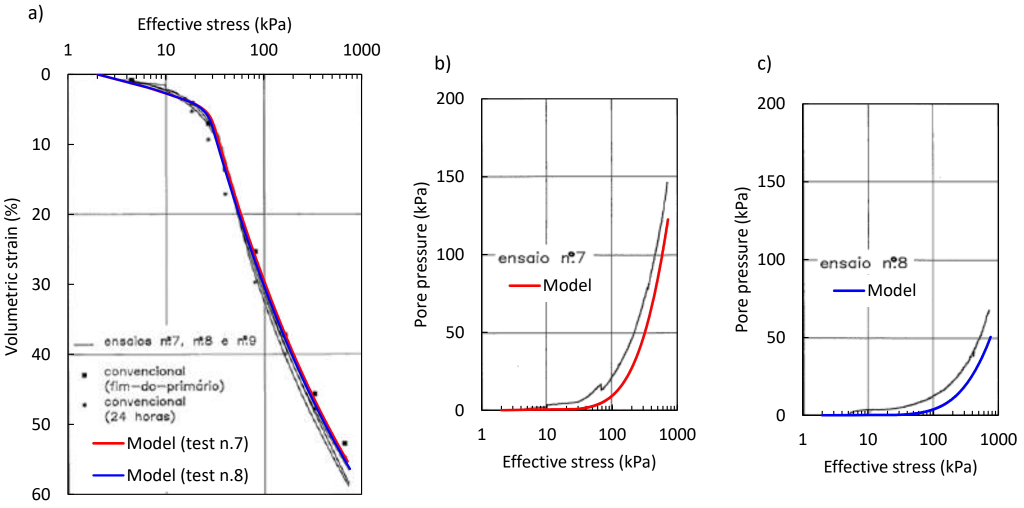

Figure 6.4: Simulated and measured compression curves and pore pressures of CRS tests (Carvalho, 1989).

(1989); Almeida et al. (1992). The model overall behavior got better by activating Plaxis *Update Mesh* and *Update Pore Pressures* options by performing a *Consolidation Analysis*. It was noted that the response of pore pressures was substantially affected by permeability variations during the consolidation process, but following the experimental results of Lacerda et al. (1977), the prediction was consistent, although slightly shifted to the right, as shown in Figure 6.4.

The initial value of the preconsolidation pressure also generally influences the model response. It is worth remembering that the preconsolidation pressure observed in the CRS test increases with the imposed strain rate. This phenomenon was evidenced by Leroueil et al. (1985) by means of CRS tests performed on Batiscan clay. Those authors have shown the trend of the apparent preconsolidation pressure to increase with the volumetric strain rate.

The experimental trend is reflected by the theory. As a matter of fact, according to the elasto-viscoplastic constitutive model presented in Section 5.1, one can demonstrate that exists a direct relationship between the apparent preconsolidation pressure and the volumetric strain rate, given by:

$$\sigma'_p = p_0 \left[1 + \frac{1}{b} \ln(1 + \mu \dot{\epsilon}_v^{vp}) \right] \tag{6-8}$$

In the above equation there are two contributions, one static and one dynamic. The value actual value of the in-situ preconsolidation pressure, p_0, probably cannot be directly observed in any test, as one should carry out a quasi-static loading program. Moreover, p_0 can assume whatever value, as the soil may be unconsolidated (OCR $<$ 1), normally consolidated (OCR $=$ 1) or overconsolidated (OCR $>$ 1).

After that, it was tried to reproduce the long-term behavior (creep behavior) observed in conventional oedometric tests. Figure 6.5 shows the tests performed by Vieira (1988) on Sarapuí clay plotted as settlement versus time curve (time in log scale). One can observe in these curves practically all the characteristics of the theoretical curves: the primary consolidation branch is followed by the secondary compression phase. The effect of different loading ratios is investigated on the development of settlement curves, showing that the primary consolidation becomes more predominant with increasing the loading ratio (Leonards and Girault, 1961). And the model predictions (red, blue, yellow and green curves in Figure 6.5) are satisfactory with respect to the stabilization time and the magnitude of the secondary settlement.

Afterward, one of the experiences reported by Lima (1993) was simulated. In test no. 08, at the end of the primary consolidation, Lima (1993) observed that the pore pressure began to increase after drainage closure. Thus, he concluded that excess pore pressure may develop in absence of deformations of the sample. The test is, indeed, a stress relaxation test under constant vertical total stress.

In Plaxis 2D, drainage closure was activated by imposing undrained conditions at the same time as Lima (1993). Switching from a *Consolidation Analysis* to a simple *Plastic fully undrained* option, the numerical model prediction was appropriate, with pore pressure starting to rise consistently. Figure 6.6 shows the pore pressure experimental curve for the one-dimensional consolidation test performed by Lima (1993) and its comparison with the numerical simulation.

Feijó (1991) carried out a series of edometric tests to study the phenomenon of secondary expansion in specimens subjected to different unloading

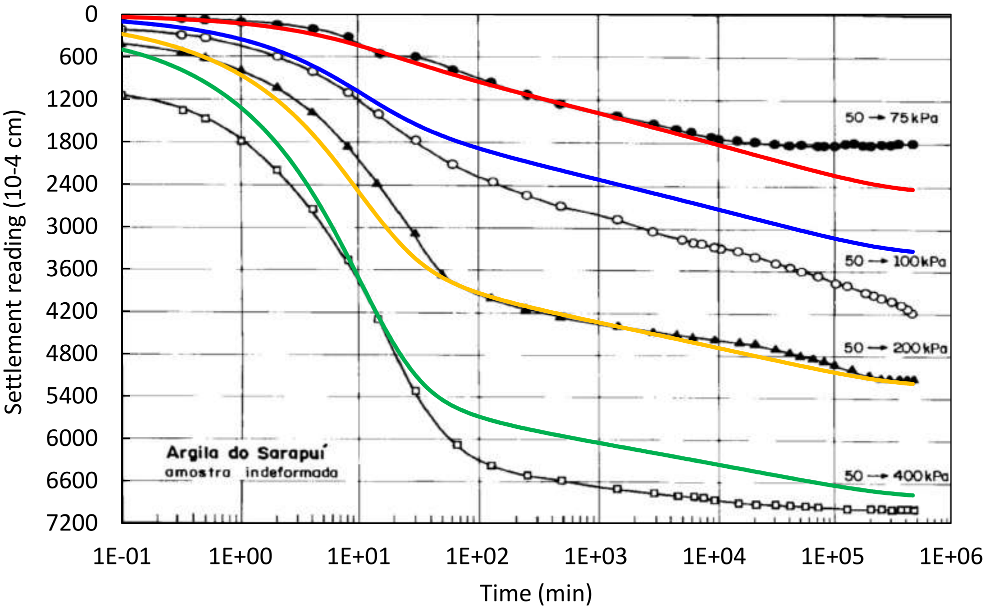

Figure 6.5: Simulated and measured long term one-dimensional consolidation tests on Sarapuí clay (Vieira, 1988).

ratios. In this case, the numerical model greatly underestimated the volumetric expansion for highest OCRs (Figure 6.7). However, the model was able to predict the overall characteristics of the experimental curves, including secondary expansion. It was concluded that for OCR < 2, model predictions were acceptable.

6.1.3
Conclusion

In this section, the capability of a viscoplastic constitutive model to reproduce the viscous behavior of Sarapuí clay was evaluated. It was adopted an elasto-viscoplastic constitutive model based on Modified Cam Clay and Perzyna's classical theory of viscoplasticity. The model was implemented in Plaxis 2D to simulate several consolidation and stress relaxation tests reported in the literature.

Particular attention was given to the stress relaxation test under undrained hydrostatic condition. The equations that govern the problem and the viscoplastic parameters related to the pore pressure increase were presented, allowing the experimental determination of the viscous nucleus function. The adoption of a viscous nucleus of the exponential type was able to reproduce the experimental data in an excellent way. Since the constitutive model was conceived to exhibit isotropic hardening with volumetric viscoplastic strain, hydrostatic tests were considered the most favorable for the calibra-

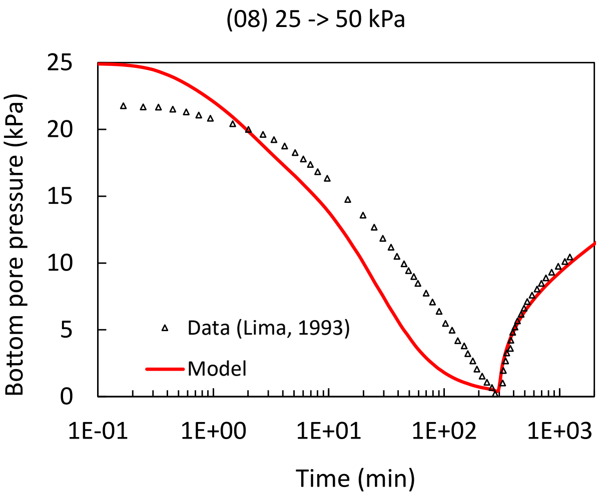

Figure 6.6: Simulated and measured increase of pore pressure after closing the drainage at the end of primary consolidation (Lima, 1993).

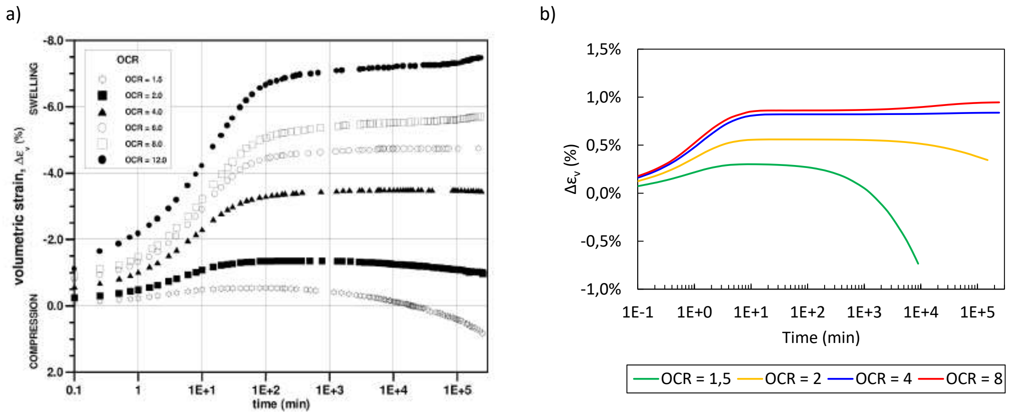

Figure 6.7: Volumetric strains after unloading of Sarapuí clay: (a) experimental curves from (Feijó, 1991); (b) simulated volumetric expansion.

tion of the parameters λ^*, μ and b. The remaining parameters were obtained similarly as for ordinary Modified Cam Clay.

Finite element numerical simulations were performed in order to reproduce the laboratory tests reported by Vieira (1988), Carvalho (1989), Feijó (1991) and Lima (1993). When necessary, a consolidation analysis was performed in order to account for the hydro-mechanical coupling. Unfortunately, the numerical model greatly underestimated the volumetric expansion for high OCRs and is therefore not recommended for highly overconsolidated clays.

The results of the numerical simulations indicated that the proposed constitutive model is capable of reproducing practically all the characteristics of the experimental curves, requiring only two additional parameters compared to Modified Cam Clay.

6.2
R-Soil model parameters of Vila Velha sandstone from laboratory tests

The mechanical behavior of hard soils and soft rocks can be modeled under the unified framework proposed by Gens and Nova (1993) since critical state models accounting for bonds degradation have been satisfactorily applied for predicting the mechanical behavior of calcarenite (Lagioia and Nova, 1995), chalk (Hickman et al., 2008), weathered granite (Nova, 2000), artificially cemented sands (Yu et al., 2007) and structured clays (Suebsuk et al., 2010).

On the basis that the sandstone can be regarded as belonging to this category, this section addresses the laboratory tests carried out on Vila Velha sandstone by Barroso (2002), which are simulated with finite elements to examine the performance of the R-Soil model (proposed in Sec. 5.2) for predicting the mechanical behavior of the soft sedimentary rock under different stress paths. In addition to validating the basic formulation and numerical implementation, this study aims to provide a new tool for the oil industry to model adequately the oil production to more profitable operations. Although simplex, the simulations presented herein are seen as laying the basis for more complex analysis, such as the wellbore instability and sand production in weakly consolidated to unconsolidated sandstone formations.

6.2.1
Case description

Barroso (2002) reports an extensive experimental program comprising 33 tests carried out on samples from sandstone outcrops of Vila Velha and Rio Bonito from Paraná Basin, Brazil. The tests were performed at the rock mechanics laboratory of the Petrobrás S.A. Research Center (Cenpes) in Rio de Janeiro. The hydro-mechanical behavior of these weak sedimentary rocks is considered analogous to oil reservoir formations usually encountered in Brazil. Tests consisted of:

1. Complete physical and mineralogical characterization.
2. Uniaxial (unconfined) compression tests.
3. Drained triaxial compression tests.
4. Hydrostatic compression tests.
5. Constant $s' = \frac{\sigma'_1+\sigma'_3}{2}$ stress tests.

This study will focus on the laboratory tests conducted on Vila Velha sandstone retrieved from the outcrop of Vila Velha, that is a sandstone ruiniform relief of the ltararé Group in the Paraná Basin, Brazil. The sandstone is a

Table 6.3: Mineralogical composition and experimental parameters of Vila Velha sandstone (Barroso, 2002).

Element	Content
Quartz	56.4%
Feldspar	5.4%
Rock fragments	1.6%
Matrix	8.7%
Silica cement	4.6%
Iron oxide cement	2.4%
Pores	20.7%

Peak strength envelope
$\phi = 53.7°$, $c = 0.72$ MPa

Elastic behavior

E (GPa)	ν	Test
1.3	0.25	Uniaxial
8.8	0.26	TXCD 5 MPa
10.9	0.17	TXCD 10 MPa

homogeneous weak rock with very low permeability ($k = 10.7\,\mathrm{mD}$), characterized by a porosity around 20%, a granular matrix predominantly composed by quartzitic grains and clay minerals of kaolinite and illite. Mineralogical composition, strength and stiffness characteristics of the sandstone are synthetically presented in Table 6.3.

The presence of cementation filling the intergranular space arises from mineral cements (silica) and iron oxides at inter-particle contacts. The high packing density (70.74%) - a textural parameter defined by Kahn (1956) - indicates that the material has a compact internal structure, that leads to improved geomechanical properties, like higher strength, lower deformability and lower permeability.

Mineralogy and petrographical characteristics have remarkable consequences on the geomechanical properties and, as it will be shown in the next section, the behavior of Vila Velha sandstone is similar to that of a very-dense (or heavily overconsolidated) weakly-cemented sand.

6.2.2
Experimental results and model calibration

Table 6.4 lists the material parameters involved in the model. Compared to the original Cam Clay model, seven additional parameters are introduced. For calibrating them, a staged approach is applied, as follows:

1. Calibration of the Basic R-Soil parameters for the uncemented reference material ($\lambda^*, \kappa^*, \nu, M, p_0$).

2. Calibration of advanced parameters controlling the yield function (r), plastic potential (ψ) and deviatoric hardening (B_q).

3. Calibration of the parameters related to bond strengths (p_{t0}, R) and the corresponding degradation law (ω, B_d).

Table 6.4: R-Soil model parameters for Vila Velha sandstone.

Model setup	Parameters	Physical meaning
Basic Critical State Model (associated)	$\lambda^* = 0.024$	Modified compression index
	$\kappa^* = 0.004$	Modified swelling index
	$\nu = 0.227$	Poisson's ratio
	$M = 1.85$	Critical state parameter
	$p_0 = 130.077$ MPa	Isotropic preconsolidation stress
Nonassociative Model	$\psi = 10^6$	Dilatancy parameter
	$r = 2.037$	Spacing ratio
	$B_q = 0$	Deviatoric hardening coefficient
Structured Model	$\omega = 300$	Destructuring rate
	$p_{t0} = 0.209$ MPa	Initial value of tensile yield stress
	$B_d = 0.33$	Weighting factor for destructuring strain
	$R = 20$	Compressive/tensile bonds strength ratio

The Basic R-Soil parameters are those shared with classical critical state models. The critical state parameter (M) may be obtained from the ultimate strength or directly from the stress-dilatancy behavior. The former approach assumes an ultimate state associated with large strains, where the geomaterial behaves in conditions of perfect plasticity (Nova, 2010). The latter consists of fitting Eq. 5-39 against the experimental stress-dilatancy behavior (see Fig. 6.8), in order to correctly predict the evolution of plastic strains and the stress ratio at critical state. Ideally, the calibration of M should be carried out as a compromise between all "situations" allowing to the model to simulate real behavior and economize on parameters.

As shown in details in Figure 6.9(a), the envelope corresponding to the ultimate state is assumed to coincide with the critical state line. This straight line passes through the origin because, at the ultimate state, there is a significant reduction in cohesion associated to the destruction of natural bonds. The ultimate friction angle is $\phi_u = 45°$, because $M = \frac{6\sin\phi}{3-\sin\phi} = 1.85$.

Figure 6.9(b) shows the whole theoretical yield locus obtained by curve fitting the peak strength points with the expression given in Eq. 5-48. The yield locus is idealized as a tear-drop aligned with the hydrostatic axis. The calibrated values of p_0, p_{t0} and n provide the best fit to experimental peak strengths along the shear failure surface. Although there is a lack of information about the position of the cap, the isotropic preconsolidation pressure (p_0) is automatically extrapolated by means of the curve fitting process. Obviously, to make a more reliable estimation about the position of the cap, one should run additional drained triaxial tests at higher confining pressures or, at least, a hydrostatic compression beyond the elastic threshold. Figure 6.10

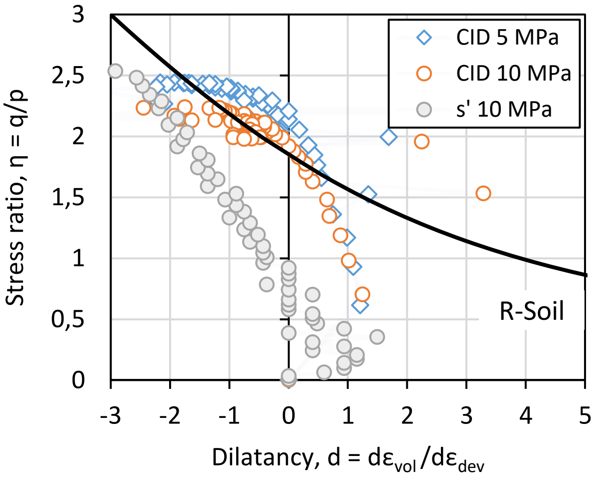

Figure 6.8: Test results of stress–dilatancy relation obtained from drained triaxial tests on Vila Velha sandtone (Barroso, 2002), and R-Soil formulation with Eq. 5-39 and M, ψ from Tab. 6.4.

shows the compression behavior of Vila Velha sandstone up to a pressure of about 80 MPa. There is no evident sign of the preconsolidation pressure in the experimental curve, therefore, it is assumed that the material was not sufficiently loaded to reach the elasto-plastic regime.

The second set of parameters (ψ, r, B_q) determines the stress-dilatancy behavior, location of critical state and deviatoric hardening. In Table 6.4, there are default values corresponding to the trivial choices of neglecting the deviatoric hardening ($B_q = 0$) and assuming a plastic potential similar to Modified Cam Clay, with M and n given, then:

$$\psi = 10^6 \quad \text{and} \quad r = \left[1 - \frac{M^2}{9}\right]^{-1/n}$$

Another possibility could have been keeping the plastic flow associated:

$$\psi = 10^6 \quad \text{and} \quad r = \left[1 - \frac{M^2}{9}\right]^{\frac{1}{2} - \frac{9}{2M^2}}$$

but a lower values for M should be used instead.

The third set of parameters (ω, p_{t0}, B_d, R) is used to model the mechanical degradation. Calibration of these parameters is made along post-peak (softening) response, taking into account all the considerations made by Nova and coworkers (Lagioia and Nova, 1995; Castellanza and Nova, 2004; Navarro et al., 2010; Rios et al., 2016; Ciantia et al., 2018).

The magnitude of cementation is expressed by the bond strength (p_t). If this quantity is simply set to zero, the structured model is deactivated. The

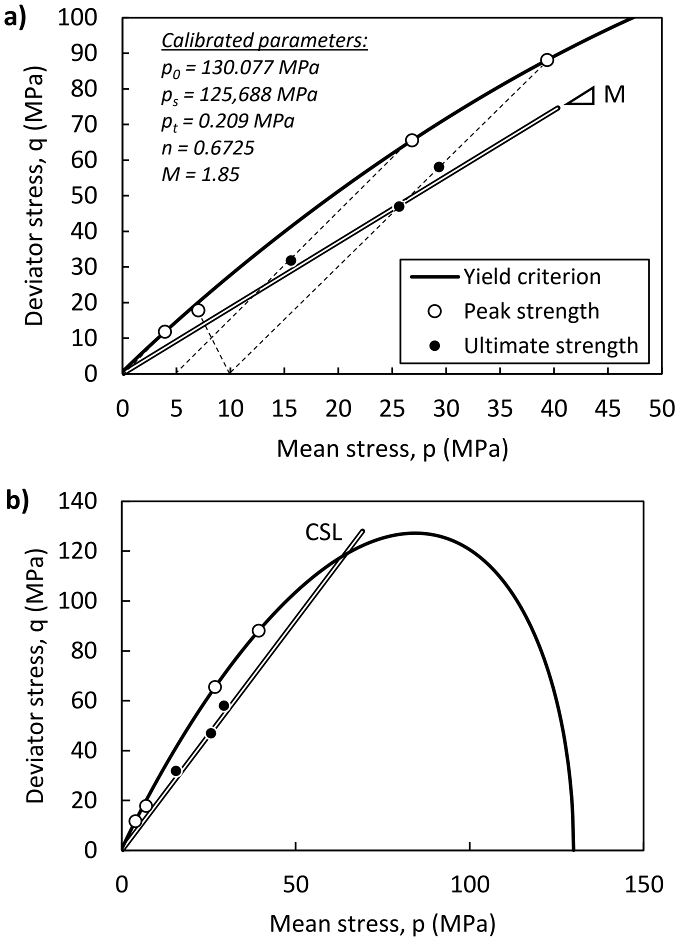

Figure 6.9: Calibration of the R-Soil yield function for Vila Velha sandstone.

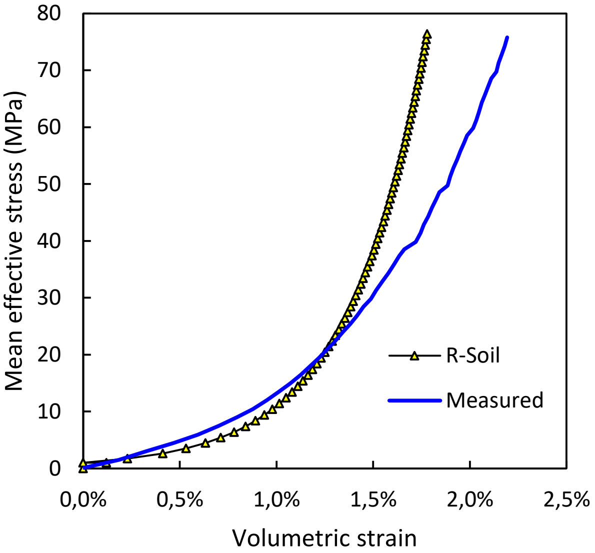

Figure 6.10: Simulated and measured hydrostatic loading on Vila Velha sandstone.

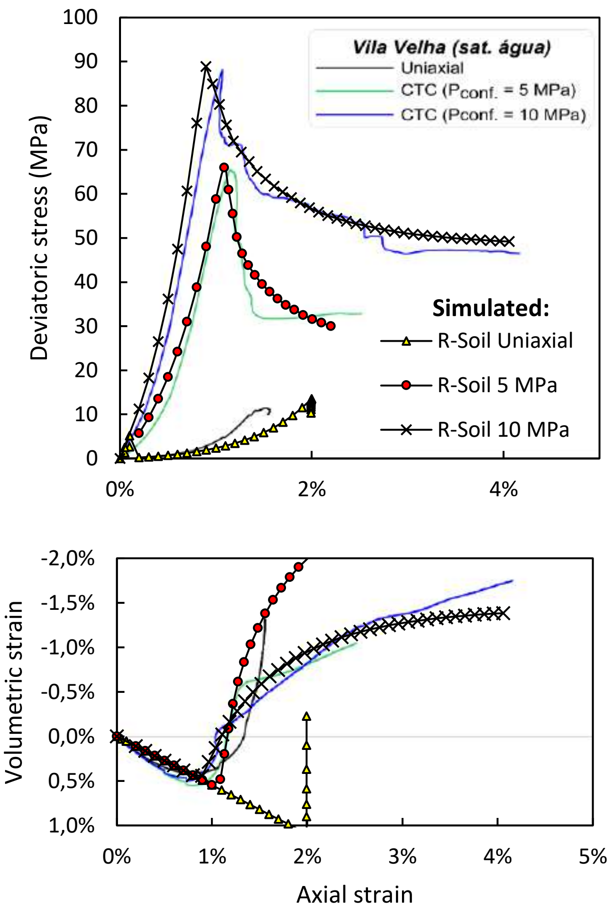

Figure 6.11: Simulated and measured drained triaxial compression tests on Vila Velha sandstone.

softening law can be assumed equal to the hardening law, either in relative (i.e. $\frac{dp_s}{p_s} \approx \frac{dp_t}{p_t}$) or in absolute variations (i.e. $dp_s \approx dp_t$). At a first attempt, a trial value for the rate of bond degradation may be $\omega = \frac{1}{\lambda^* - \kappa^*}$.

The comparison between the simulated and measured stress-strain behavior in drained compression is shown in Figs. 6.10, 6.11 and 6.12. In triaxial compression, Vila Velha sandstone shows brittle failure with well pronounced peak deviatoric stress within the range of applied confining pressures. Failure occurs at around 1% of axial strain. In Figure 6.11, the initial part of the curve is elastic and concave upward. The post-peak response is dilatant with a sudden drop in shear strength accompanied by progressive softening until a stable (ultimate) condition is reached.

In Figure 6.12, the stress-strain curve under constant s'-compression does not show a post-peak behavior because the test was performed under loading control. It can be seen from the figures that the simulated response is in good agreement with the experimental data.

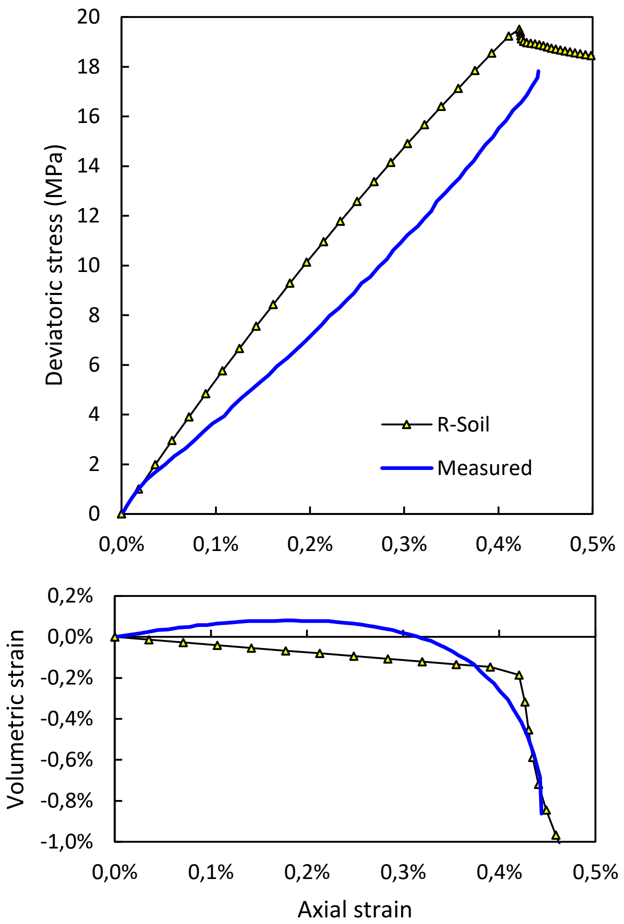

Figure 6.12: Simulated and measured behavior in constant-s' test.

6.2.3
Final remarks

The laboratory tests reported by Barroso (2002) were used to calibrate the R-Soil model parameters in order to reproduce the mechanical behavior of Vila Velha sandstone. From test results, the post-peak response was accurately calibrated according to the characteristics of strength and dilatancy. On the basis that the sandstone can be regarded as a heavily overconsolidated cemented sand, the overall predicted stress-strain behavior coincided well with test results.

The overconsolidation ratio is high (OCR=12-25) and its effect is significant. However, the influence of cementing elements is prominent close to the origin, introducing a tensile yield strength or, equivalently, a cohesive intercept with the q-axis, given by the following expression:

$$q_t = 3p_t\sqrt{1-\left(\frac{p_t}{p_0}\right)^n} \tag{6-9}$$

For Vila Velha sandstone $q_t = 0.623$ MPa, that is a value approximately three times the yield stress in pure tension (p_t).

7
Attached Papers

7.1
Constitutive modeling of residual soils based on the decomposition of irreversible strains

Constitutive modeling of residual soils based on irreversible strains decomposition

Alessandro Cirone[1*], Eurípedes Vargas Jr[1], and Tácio de Campos[1]

[1]Department of Civil and Environmental Engineering, Pontifical Catholic University of Rio de Janeiro, Brazil

*Corresponding author, Tel: +55 (21) 995461945; email: a.cirone@aluno.puc-rio.br

ABSTRACT

A constitutive model is proposed for describing the stress-strain behavior of saturated residual soils based on experimental observations from oedometer testing, triaxial and direct shear testing. The model is formulated within the classical theory of plasticity with a non-associated flow rule. In order to reproduce particular features of residual soils, inelastic strains are decomposed in two components, namely the plastic dilation due to the rearrangement of grains and the volumetric collapse resulting from bonds degradation. The yield surface is tear-drop shaped and obeys an isotropic volumetric strain-hardening rule related to collapse strains, along with a shear softening with developing plastic deviatoric strains. Comparison with published experimental data confirms the capability of the model of reproducing observed behavior of tropical residual soils in consolidated drained and undrained triaxial compression.

Keywords: constitutive relations, plasticity, residual soil,

INTRODUCTION

The term residual soil is widely used in contrast to *sedimentary (or transported) soil* to designate those soils that do not derive from erosion, transport and deposition of sediments, but result substantially from the in place weathering of the parent rock (Duarte and Rodrigues, 2017). This origin-based definition reflects the importance of lithological characteristics and environmental conditions on the engineering behavior of residual soils, whose description and study cannot be dissociated from the respective weathering history of the parent rock.

Occurring in many regions of Brazil, residual soils may derive from the weathering of granite, gneiss, basalt or sandstone. In southern Brazil residual soils from basalt are dominant (Consoli et al., 1998), whereas weathering profiles of granite-gneiss are commonly encountered around São Paulo and Rio de Janeiro (de Mello, 1972). Martins et al. (2005) have also reported a residual soil originated from the weathering the Aeolian Botucatu sandstone.

The weathering profile reflects the decay of rock towards the residual soil condition. Typical examples from Brazilian literature have been reported by Viana da Fonseca and Coutinho (2008). Ideally, the weathering profile consists of different horizons varying from sound rock, weathered rock to residual soil. If the soil exhibits features from the parent rock, then it is classified as *young residual soil* or *saprolitic soil*. Otherwise, if there is no detectable relic structure, the expression *mature residual soil* is used. On top, one may encounter *lateritic* soils or transported soils (*colluvium*) that may undergo weathering as well. Lateritic soils contains laterite, which is impregnated with, cemented by or partly replaced by hydrated oxides of iron and alluminium (Fookes, 1997). Quite well known by Brazilian engineers, these denominations were further explained by Vargas (1953) and Barata (1969).

Depending on the weathering grade, residual soils may preserve macrostructure inherited from the parent rock (schistosity, fissures, joints, litho-relicts etc.) as well as microstructure (macropores, fabric, bonds between particles). According to Costa Filho et al. (1989), the presence a weakly bonded structure, resulting from predominant chemical weathering, provides to the residual soil:

a) true cohesion in terms of effective stress
b) apparent preconsolidation pressure related to structure and bonds strength
c) higher stiffness at lower stresses and plastic behavior at higher stresses, characterizing a yield surface.

The natural process of weathering influences the composition (clay minerals), grain shape, grain size, void ratio, structure, permeability, strength and deformability of residual soils. Obviously, those features strongly affect the overall engineering behavior of residual soils, as well explained in the general reports provided by Blight (1989) and Costa Filho et al. (1989). From a mechanical standpoint, weathering is modeled as a softening process (Vaughan and Kwan, 1984).

During the last four decades an extensive laboratory work has been carried out mainly at Rio de Janeiro to study the stress-strain relationships of tropical granite-gneiss residual soils. Testing has been carried out on intact and compacted samples of local lateritic and saprolitic soils, under both saturated and unsaturated conditions. Strong experimental evidences have been produced and some patterns of the geotechnical behavior have been established. The research focused mostly on the geotechnical and geological characterization, analyzing test results according to the conventional principles and methods of soil and rock mechanics. Similar studies have been carried out on residual soils from the São Paulo Metropolitan Area (Futai et al., 2012), North-east of Argentina (Bogado et al., 2019; Franscisca and Bogado, 2019), Indonesia and New Zealand (Wesley, 2009) and Hong Kong (Rocchi and Coop, 2015), just to cite a few.

The experimental characterization has been accompanied by the need of developing a modeling framework for predicting the mechanical behavior of residual soils and the response of related geotechnical structures. Various advanced constitutive models have been employed and tested. Some researchers used enhanced versions of Cam Clay, introducing isotropic damage (Puppi et al., 2018), influence of structure (Mendoza et al., 2014) or the subloading surface (Mendoza and Muniz de Farias, 2020). Others (Azevedo et al., 2006) have used the Lade's model (Lade and Kim, 1988; Kim and Lade, 1988) and the discrete element modeling approach (Ibañez, 2008). Unfortunately, most of the aforementioned models were conceived for sedimentary soils and then adjusted to residual soils. In contrast, the authors have developed a constitutive model specifically designed to reproduce the behavior of residual soils starting from experimental observations. The main assumption is the decomposition of irreversible strains into two mechanisms: the particle rearrangement and the bonds degradation. In addition, specific hardening laws have been adopted.

This paper presents the formulation of this new constitutive model within the framework of classical strain hardening plasticity. In doing so, the behavior of saturated residual soils observed from oedometer testing, triaxial and direct shear testing is firstly examined. Then, the constitutive model is formulated and validated in drained and undrained triaxial compression tests.

SHEAR STRENGTH AND STRESS-STRAIN BEHAVIOR OF RESIDUAL SOILS

For sake of clarity, results of several tests on residual soils are herein summarized to establish patterns of the behaviour observed from oedometer testing, triaxial and direct shear testing.

Figure 1 presents the results of a K_0-test on a partially saturated sample of intact gneissic residual soil carried out by Maccarini (1980, 1987). The sample was obtained from the slope of an excavation at a depth of 8.05 m, measured from the original ground level, where the total vertical in situ stress was estimated to be 130 kPa prior the excavation. The sample was incrementally loaded under stress control allowing drainage from top and bottom against atmospheric pressure.

As shown in Figure 1(a), below a quite pronounced yield stress, σ_{vm}, located around 200-250 kPa, the behavior is stiff and elastic. This first part of the oedometric curve comprises a reloading stage. As the vertical stress is increased, yield occurs, the soil becomes more compressible and the behavior is elastoplastic. This is reflected by the sharp difference of the slopes in the compression curve of Figure 1(a). Figure 1(b) shows that the same trend is clearly followed by the stress path in the (q, p) plane. There is an initial elastic response and stress path draws a straight line up to the yield stress. Further loading deviates the stress path, which gradually approaches the K_0-line of the destructured soil (Leroueil and Vaughan, 1990) as the vertical stress is increased. As shown by Castellanza and Nova (2004), during elastic loading the slope of the stress path is directly linked to Poisson's ratio. Maccarini (1987) measured K_0 as low as 0.1 within the elastic domain, corresponding to a Poisson's ratio of 0.09. At higher stresses, the same author reported values of K_0 6 or 7 times greater, compatible with the destructured soil. It should be noted that Maccarini (1980, 1987) measured K_0 in terms of stress increments, i.e. $K_0 = \Delta\sigma_3/\Delta\sigma_1$, following the definition given by Andrawes and El-Sohby (1973).

Shearing tests on residual soil give plots of the general shape showed in Figure 2, where data from a series of direct shear tests performed by Escalaya (2016) on young granitic residual soil from Duque de Caxias, Rio de Janeiro, are presented. Intact (undisturbed) samples tested in the direct shear apparatus were first sheared in submerged condition to obtain the peak shear strength. Afterwards, the residual strength was determined using the polished cut-plane technique as described by Garga and Seraphim (1975).

Results from drained shear tests on residual soil reveal that the shear strength parameters are related to the weathering grade, to the mineralogical content and the macrofabric resulting from weathering of the parent rock (Garga, 1988; Massey et al., 1989; Lacerda, 2010). The behavior is similar to that of a dense sand, yet with less pronounced peak strength at low normal stress. The displacement at failure increases with increasing the applied normal stress and, as shown in Figure 2(a), there is a clear reduction in dilatancy as the normal stress is increased. The gradual loss of strength after peak point is passed may be attributed to a gradual decrease in interlocking and destructuration.

The failure envelopes are shown in Figure 2(b). High mica content in mineralogical composition may explain the significant drop in shear strength between peak and residual condition. The residual shear strength envelope, although passing through the axis origin, is not linear at low vertical stress. At a first approximation, a linear envelope with no cohesion intercept has been assumed in Figure 2(b). The peak strength envelope is markedly curved at lower normal stresses. Adopting a linear strength envelope from tests run at high stresses underestimates the strengths in the low stress range (Brand, 1985). Some authors (Massey et al., 1989; Gan and Fredlund, 1996) attribute this additional strength to dilation and weak bonding derived from weathering. Volume increases which are taking place at failure cause somewhat greater values of shearing strength along the curved portion of the envelope, whereas volume decrease takes place along the straight line portion of the envelope. For the case under consideration, the deviation from a straight line occurs at normal stress of about 100 kPa. This point is often referred as the “critical normal stress” that marks the transition from dilatant to contractant behavior during shear.

Figure 3 shows the result of a set of standard drained triaxial tests performed by De Oliveira (2000) on intact young residual soil derived from biotite-gneiss, collected in Alto Leblon, a neighbourhood in the city of Rio de Janeiro. Specimens were isotropically consolidated to effective stresses of 25, 70 and 150 kPa, and then sheared at constant axial strain rate equal to 8.2 x 10^{-5} mm/s. It is possible to identify a general trend in the stress-strain behavior under different confining stresses:

a) at low confining pressure, after reaching a well defined peak deviator stress at an axial strain less than 3%, the specimens exhibits brittle failure associated with dilatant behavior. Softening occurs until a stable deviator stress is reached. Additionally, the lower the confining pressure the more dilatant is the behaviour.

b) at the highest confining pressure, equal to 150 kPa, no peak stress is observed. The stress-strain curve resembles that for an elastic–perfectly plastic material. However, the soil still exhibits the tendency to dilate at failure.

According to De Oliveira (2000), such behavior is typical of soils with bonded structure in the sense described by Leroueil and Vaughan (1990): at low confining stress, peak strength is due to structure, yield is abrupt and the material very brittle; as the confining pressure is increased, the behavior changes from brittle to ductile. De Oliveira (2000) attributed the presence of natural bonding agents between particles to the precipitation of iron oxides between quartz, feldspar and garnet.

Behavior in drained triaxial compression may also follow the trend shown in Figure 4, which is quite different from the one presented in Figure 3. Data are taken from Reis (2004), who tested a gneissic young residual soil from the city of Viçosa, Minas Gerais State, under confining effective stresses ranging from 50 to 400 kPa and obeying the natural banding inclination. The resulting stress-strain curves exhibited less marked peaks and a gradual change from dilatant to contractive behavior with increasing confining stress, which also increased the axial strain at peak. Remarkable was the fact that at the highest confining stress, the soil contracted reaching a peak stress and then it softened at constant volume. This behavior can be explained considering destructuration during the shearing phase, which implies shear strength degradation. Similar results have been presented by Santos et al. (2020), who attributed this kind of behavior to the structure inherited from the parent rock. According to them, the observed peak strength should be attributed to the structural effects, as there is no geological evidence of past overconsolidation in this soil.

Other experimental evidences for the existence of bonded structure in residual soils were given by Consoli et al. (1998). They have shown that prestressing a soil sample produces substantial damage to the bonds, deteriorating its strength and stiffness. According to them, this experimental evidence contrasts with ordinary patterns observed on clay, for which overconsolidation has a positive impact on strength and stiffness.

CONSTITUTIVE MODEL FORMULATION – MATHEMATICAL TREATEMENT OF SOIL BEHAVIOR

In the proposed model the irreversible strains are decomposed into two parts, namely the strains resulting from the rearrangement of the grains (plastic strains) and those resulting from damage of structure (collapse strains). Therefore, the total strain rate is decomposed into elastic, plastic and collapse components:

$$\dot{\varepsilon}_{ij} = \dot{\varepsilon}_{ij}^{e} + \dot{\varepsilon}_{ij}^{p} + \tfrac{1}{3}\delta_{ij}\dot{\varepsilon}_{v}^{c} \qquad (1)$$

where δ_{ij} is the Kronecker delta. The additive strain decomposition holds under the small strain hypothesis. The elastic strains are, by definition, recoverable and uniquely related to stresses by Hooke's law. Irrecoverable strains are decoupled into those resulting from plastic deformation of the granular matrix, $\dot{\varepsilon}_{ij}^{p}$, and those resulting from volume change due to structure collapse, $\dot{\varepsilon}_{v}^{c}$. Both are calculated according to the classical theory of plasticity by assuming the existence of a yield criterion and a flow rule.

The decomposition of irreversible strains into two parts (plastic collapse strain and plastic expansive strain) is not novel in constitutive modeling. As instance, Lade (1977) used distinct yield surfaces and flow rules to calculate plastic and collapse strains in modeling the behavior of Sacramento River Sand.

Within the framework of modeling the behavior of residual soils, the collapse strains are assumed as the volumetric contraction caused by structure degradation. On the other hand, the plastic strains are associated uniquely to grain rearrangement as described by Chandler (1985).

A suitable stress space to describe the triaxial stress state is (p',q), where $p' = (\sigma'_1 + 2\sigma'_3)/3$ is the effective mean stress and $q = \sigma'_1 - \sigma'_3$ is the deviator stress. The corresponding strain invariants are $\varepsilon_v = \varepsilon_1+2\varepsilon_3$, the volumetric strain, and $\varepsilon_d = 2/3*(\varepsilon_1 - \varepsilon_3)$, the deviatoric strain. Furthermore, the ratio between the deviator and effective mean stress, $\eta' = q/p'$, is very useful in calculations and is referred to as the stress ratio. For simplicity, only saturated behavior is considered, being the aim of the model to reproduce the soil response under drained and undrained triaxial compression.

The assumed expression to describe a teardrop shaped yield locus for a residual soil is:

$$f : \left(\frac{p'}{p_0}\right)^2 + \left(\frac{\eta'}{\eta_0}\right)^2 = 1 \qquad (2)$$

Figure 5 shows that the model has a single yield function with two portions clearly distinguishable: the compression cap and the shear failure envelope. The transition between the two parts is smooth and occurs at $\eta' = \eta_0 / \sqrt{2}$. The parameter p_0 controls the position of the cap, while η_0 is the maximum stress ratio associated to shear failure. They are treated as hardening parameters and both depend on irrecoverable strains.

To develop simple and suitable hardening laws to describe the evolution of the yield surface during loading, the following assumptions are introduced:

1. when soil is loaded under isotropic compression, the irreversible volume strain is only caused by structure collapse. In this sense, the cap hardening depends solely on collapse strains resulting from yielding of soil structure, i.e. $p_0 = p_0\left(\varepsilon_v^c\right)$.
2. the shear failure envelope is related to frictional strength and grain rearrangement and, consequently, to plastic strains, i.e. $\eta_0 = \eta_0\left(\varepsilon_{ij}^p\right)$.

The dependence on p_0 of the collapse volumetric strain can be derived by assuming convenient expressions for the calculation of total and elastic volumetric strain increments in isotropic loading. The elastic volumetric response associated with changes in mean effective stress may be described by an equation in the form:

$$e = e_k - \kappa \ln p' \qquad (3)$$

where e_k is the intercept of the unloading-reloading line at $p = 1$ and κ is its slope in the $e - \ln p'$ plot. Equation (3) is a common description of soil elastic behavior and provides the shape of the unloading-reloading lines in the (e,p') plane for stress states within the elastic domain.

For loading beyond the elastic threshold, it is assumed that the reduction in void ratio is directly proportional to the void ratio itself and the increase in mean effective stress:

$$de = -\frac{e}{C_b}dp' \tag{4}$$

in which a constant of proportionality, C_b, has been introduced. Such constant has the dimension of a stress. It has the role of a stiffness and will be referred herein as the "*compaction modulus*". Equation (4) may also be regarded as the constitutive law for hydrostatic compaction. It states that that the compressibility, $\beta = d\varepsilon_v/dp'$, is proportional to the current porosity, $\phi = e/(1+e)$. Indeed, dividing both sides of Equation (4) by $1+e$ and recalling that $d\varepsilon_v = -de/(1+e)$, one obtains:

$$\frac{d\varepsilon_v}{dp'} = \frac{\phi}{C_b} \tag{5}$$

It is worth noting that this result is valid under the hypothesis of incompressible solids ($dV_s = 0$). Equation (4) and (5) are both written in incremental form and are formally identical. Equation (4) can be easily integrated to obtain the equation for the normal compression line:

$$e = e_0 \exp\left(-\frac{p' - p_0}{C_b}\right) \tag{6}$$

that provides a simple description of the shape of the normal compression line, in the (e,p') compression plane, accounting for non-linearity of stress-strain response under applied isotropic compression.

The cap hardening law arises from assumption 1. If plastic volumetric strain are neglected in isotropic compression, then the total volumetric strain resulting from the change in p_0 is just elastic and collapse:

$$d\varepsilon_v = d\varepsilon_v^e + d\varepsilon_v^c \tag{7}$$

recalling Equations (3) and (4), it yields

$$\frac{e}{1+e}\frac{dp_0}{C_b} = \frac{\kappa}{1+e}\frac{dp_0}{p_0} + d\varepsilon_v^c \tag{8}$$

from which the cap hardening law is derived:

$$\frac{dp_0}{d\varepsilon_v^c} = \frac{p_0}{\lambda' - \kappa'} \qquad \text{with} \quad \lambda' = \frac{e}{1+e}\frac{p_0}{C_b} \quad \text{and} \quad \kappa' = \frac{\kappa}{1+e} \tag{9}$$

where λ' is the slope of the normal compression line and κ' that of the unloading-reloading line in the ($\varepsilon_v, \ln p'$) plane. It is worth noting that e, p_0 and, therefore, λ' change as the soil undergoes volumetric deformation.

As introduced in Equation (1), plastic deviatoric strains are assumed to derive from rearrangement of the grains and, thus, are related to grain alignment on a possible slip surface. This latter mechanism is responsible for decreasing the shear strength and will be modeled as an exponential decay of the maximum stress ratio with plastic deviatoric strain:

$$\frac{d\eta_0}{d\varepsilon_d^p} = -B_q\,(\eta_0 - \eta_r) \tag{10}$$

where B_q is the stress ratio decay rate, η_r is a reference value and η_0 tends asymptotically to it at failure. Equation (10) is the hardening law of the shear failure envelope.

In general, inelastic flow is not normal to the yield surface. This means that the flow rule is non-associated. Plastic strains are derived from a plastic potential, whereas volumetric collapse is derived from a collapse potential. The flow rule is:

$$\begin{aligned} \dot{\varepsilon}_v^p &= \dot{\lambda}\frac{\partial g}{\partial p'} = -\dot{\lambda} B \eta' \\ \dot{\varepsilon}_d^p &= \dot{\lambda}\frac{\partial g}{\partial q} = \dot{\lambda} \eta' \\ \dot{\varepsilon}_v^c &= \dot{\lambda}\frac{\partial g^c}{\partial p'} = \dot{\lambda} A \end{aligned} \qquad (11)$$

where $\dot{\lambda}$ is the plastic multiplier, η' is the stress ratio, A and B are parameters of the model. Following Chandler (1985), the rate of plastic volumetric change resulting from grains rearrangement is assumed to be proportional to the plastic deviatoric rate by a factor, B, that is a generalization of the angle of dilatancy. In other words, the plastic volumetric strain rate is the expansion necessary for shearing distortion; conversely, the volume collapse is, by definition, the volume contraction due to bonds breakage and mechanical damage. With such a separation, the proposed model has two mechanisms and one criterion (2M1C) according to Chaboche's (2008) classification.

The stress-dilatancy relationship corresponding to Equations (11) is:

$$d = \frac{\dot{\varepsilon}_v^c + \dot{\varepsilon}_v^p}{\dot{\varepsilon}_d^p} = \frac{A - B\eta'}{\eta'} \qquad (12)$$

that indicates no irreversible volume change at $\eta' = A/B$, that is the so-called "critical state". Hence, the parameters A and B characterize dilatancy, structure collapse and critical state.

The plastic multiplier, for a given stress increment, is derived according to the consistency condition, $\dot{f} = 0$. From Equation (2), the differential form of the yield function is:

$$\dot{f} = 0 = \frac{\partial f}{\partial p'}\dot{p}' + \frac{\partial f}{\partial q}\dot{q} + \frac{\partial f}{\partial p_0}\dot{p}_0 + \frac{\partial f}{\partial \eta_0}\dot{\eta}_0 \tag{13}$$

which combined with Equations (9), (10) and (11), gives the expression for the plastic multiplier:

$$\dot{\lambda} = \frac{1}{H}\left(\frac{\partial f}{\partial p'}\dot{p}' + \frac{\partial f}{\partial q}\dot{q}\right) \tag{14}$$

where H is the hardening modulus:

$$H = -\left(\frac{\partial f}{\partial p_0}\frac{\partial p_0}{\partial \varepsilon_v^c}\frac{\partial g^c}{\partial p'} + \frac{\partial f}{\partial \eta_0}\frac{\partial \eta_0}{\partial \varepsilon_d^p}\frac{\partial g}{\partial q}\right) \tag{15}$$

The overall value of *H* depends on two competing terms, each one related to a different mechanism: the first term is linked to volumetric collapse, the second to deviatoric plastic strains.

SUMMARY OF MODEL PARAMETERS - THEIR PHYSICAL MENANING AND EXPERIMENTAL DETERMINATION

Elastic constants

The parameter κ, the so-called "swelling index", coincides with the slope of the unloading-reloading line in the (e, ln p') plot. It can be determined with an isotropic compression test performing unloading-reloading cycles.

The Poisson's ratio relates the bulk modulus, *K*, with the shear modulus, *G*, according to the following expression:

$$\frac{G}{K} = \frac{3(1-2\nu)}{2(1+\nu)} \tag{16}$$

The ratio G/K coincides with the gradient of the volume change curve for a conventional drained compression test (Wood, 1990) if the confining pressure is below the in-situ preconsolidation pressure.

Inelastic flow

The parameters A and B control the inelastic flow. They can be determined using the expression for the stress-dilatancy relationship given in Equation (12). Figure 6 shows the dilatancy ratio ($d\varepsilon_{vol} / d\varepsilon_{dev}$) obtained from drained triaxial compression tests under different confining stresses plotted against the stress ratio (q/p'). Data points were derived from total strain increments. For this reason, the initial branch of the stress-dilatancy curve is strongly affected by elastic strains and is not recommended for calibration. Data points taken from the final branch should be favored because they lies on (or are closer to) the critical state. The intercept with the vertical axis corresponds to M = A/B = 1.32, denoting the critical state. In the present analysis, B was taken equal to M, giving a satisfactory description of the stress-dilatancy relationship. The value of parameter A is the result of the estimation of M and B. Therefore, the selected values are of A = 1.74 and B = 1.32.

The influence of the parameters A and B on the predicted response for a drained triaxial test is shown in Figure 7. The results can be summarized as follows. Increasing B shifts the volume change curve upwards, so greater volume dilation is predicted. Higher and sharper peaks also occur in the stress-strain curve. Conversely, lowering B increases the volume contraction and reduces the peak strength. Since calculations were made with constant M, the ultimate strength is not affected.

Volumetric hardening

The volumetric hardening law is calibrated by means of an isotropic compression test. Taking logarithms of both sides in Equation (6), a linear relationship is predicted between the mean effective stress and the logarithm of void ratio:

$$p' = p_0 - C_b \ln\left(\frac{e}{e_0}\right) \tag{17}$$

Therefore, the compaction modulus, C_b, equals the slope of the straight line obtained from experimental data if ln e is plotted against p', as indicated in Figure 8.

The estimation of the preconsolidation pressure should not follow conventional graphical methods, such as the Casagrande's method. Several authors (Vargas, 1953; Vaughan et al., 1988; Wesley, 1990) questioned the validity of those "conventional" approaches arguing that they were not conceived for residual soils, for which the common definition of "preconsolidation" pressure should not be applied because they do not undergo loading-unloading processes in their formation.

Imposing the continuity of the gradient along the compression curve may be an alternative method to estimate the preconsolidation pressure. If it is assumed that at elastic threshold the unloading-reloading line and the normal compression line have the same slope, one obtains:

$$\frac{\kappa}{p_0} = \frac{e_0}{C_b} \tag{18}$$

from which the in-situ p_0 is easily found, known the swelling index, κ, the in-situ void ratio, e_0, and the compression modulus C_b.

Deviatoric softening

The softening rule is a function of plastic deviatoric strains and is calibrated along the post-peak portion of the stress-strain curve for a drained triaxial compression test conducted at low confining pressure.

From Equation (10), it is clear that the relationship between $\ln(\eta - M)$ and ε_d^p is linear, being the parameter B_q equal to the slope of straight line that best fits the experimental data. The diagram of Figure 9 is obtained using data taken from post-peak branch of the stress-strain curves of the drained triaxial compression tests conducted at low confining pressures. Results clearly suggest that B_q depends on the effective confining stress. However, for simplicity, B_q is taken as constant and equal to the average of the slopes.

A general indication of the influence of the value of B_q on the response in the conventional drained triaxial compression test is shown in Figure 10. Increasing B_q increases the rate of deviatoric softening, so the stress-strain relationship shows a lower peak strength and the critical state is quickly reached. On the other hand, when B_q is small, a more ductile behavior is predicted and the model shows higher shear strength. Moreover, the model needs larger deformations to reach the critical state, the volumetric response is strongly affected and the behavior is much more dilative.

MODEL PREDICTIONS AND COMPARISON WITH EXPERIMENTAL RESULTS

The model has been employed for predicting the triaxial behavior of Ouro Preto residual soil in drained and undrained conditions. The experimental data have been provided by Futai (2002), who performed isotropic consolidation, consolidated-drained and undrained triaxial compression tests at different cell pressures. Futai et al. (2004) described the testing procedure in detail. The measured stress-strain curves, strain paths and pore pressures responses are presented in the following along with predictions from the present model.

The value of the parameters for Ouro Preto residual soil have been determined from consolidated-drained triaxial compression tests. They are listed in Table 1. A python code was developed to integrate the constitutive relations using a semi-implicit algorithm.

The results of the drained triaxial tests are shown in Figure 11(a), together with the predictions of the model. Points indicate the measured soil behavior and solid lines are model predictions. The comparison shows a good agreement between the predicted behavior and the experimental observations. The model is able to predict satisfactorily the stress-strain curves, including the gradual change from dilative to contractive behavior, accompanied by a more ductile response, when confining stress is increased. However, the model overpredicts the volume contraction in the beginning of the loading; a drawback attributable to the chosen flow rule, which is very basic.

The results of the consolidated undrained triaxial compression tests are compared with the predictions in Figure 11(b). The predicted response is less accurate, but still good. Although the model parameters were calibrated from the results of the drained triaxial tests, the model reflects the particular trend in the undrained behavior, especially for the stress paths (Figure 12) and the pore-pressure response, which are reasonably predicted. The response switches from initially contractive (increasing pore pressure, decreasing mean effective stress) to dilative (reducing pore pressure, increasing mean effective stress). The rearrangement mechanism is predominant at low confining stress and high stress ratio, so negative pore pressure are consistently predicted for the tests run at 25 kPa and 100 kPa. At higher confining pressures, the dilatancy is suppressed and positive pore pressures are developed. One negative outcome is the stiffer response of the model compared with the test run at 400 kPa of confining pressure.

CONCLUSION

A summary of relevant Brazilian experimental work was presented, involving the main geotechnical laboratory tests, in order to address typical patterns of the mechanical behavior of residual soils. The data were used to develop a constitutive model for residual soils based on the assumption that incremental strains consist of elastic, plastic and collapse components. Decomposition of inelastic strains allowed to distinguish the deformations arising from particle rearrangement from those resulting from bonds degradation and particle breakdown. A non-associated flow rule was assumed by adopting two distinct potential functions, from which each individual inelastic strain was derived. The yield surface, a single continuous function shaped as a teardrop, was expressed in terms of two stress invariants – the mean effective stress and the stress ratio. The hardening laws were developed in order to reproduce the non-linear volumetric response in the $(e, \ln p')$ plane, under purely isotropic compression, and the softening behaviour associated with shearing strains. The model is characterized by nine parameters that can be determined from simple laboratory tests, such as isotropic compression and conventional consolidated drained triaxial compression tests.

The novel feature of the model is the treatment of bond degradation as a strain-inducing process causing primarily volume contraction. Loss of interlocking is modeled as a softening process related to the particle alignment along a slip plane. The description of those two mechanisms is unified under a single yield criterion. Such an approach is pioneer and some generalizations are still under development.

The model may be enhanced to account some aspects of the engineering behavior of residual soils that were not included in this work. Possible improvements are: extension to partially saturated states, elastic stiffness degradation with mechanical damage, influence of the third stress invariant, addition of a true cohesion and modeling the anisotropic behavior due to structural discontinuities inherited from the parent rock. In addition, the model should also be tested under loading paths that are more complex than conventional CID and CIU triaxial tests.

The comparison made between published experimental behavior and model predictions is overall acceptable and encouraging. The model was validated in conventional triaxial drained and undrained compression tests by comparing the predicted and observed behavior of Ouro Preto residual soil. In particular, trends in stress-strain, dilatancy and pore pressure behavior, as well as the effective stress paths were reasonably captured under a wide range of confining stresses.

REFERENCES

K.Z. Andrawes, M.A. El-Sohby (1973). Factors Affecting Coefficient of Earth Pressure Ko. Journal of Soil Mechanics and Foundation Engineering Division, Proceedings ASCE, 99, SM7, 527-539

Azevedo, R. F., Reis, R. M., & Vilar, O. M. (2006). Elasto-Plastic Modeling of a Young Gneiss Residual Soil in Saturated and Non-Saturated Conditions. In Unsaturated Soils 2006 (pp. 1968-1979).

Barata, F.E. (1969). Landslides in the tropical region of Rio de Janeiro. 7th Int. Confer. on Soil Mech. and Found. Eng., Mexico. ISSMFE, London, pp. 507 – 516

Blight, G.E. (1989) Design assessment of saprolites and laterites. Invited Lecture, Session 6, 12th ICSMFE. Rio de Janeiro. Vol. 4, 2477–2484.

Bogado, G. O., Reinert, H. O. & Francisca, F. M. (2019). Geotechnical properties of residual soils from the North-east of Argentina. International Journal of Geotechnical Engineering, 13(2), 112-121.

Brand, E.W. (1985) Predicting the performance of residual soil slopes, in Proceedings of the Eleventh International Conference on Soil Mechanics and Foundation Engineering, San Francisco, pp. 2541-78.

Castellanza, R., & Nova, R. (2004). Oedometric tests on artificially weathered carbonatic soft rocks. Journal of geotechnical and geoenvironmental engineering, 130(7), 728-739.

Chaboche, J. L. (2008). A review of some plasticity and viscoplasticity constitutive theories. International Journal of Plasticity, 24, pp. 1642–1693

Chandler, H. W. (1985). A plasticity theory without Drucker's postulate, suitable for granular materials. Journal of the Mechanics and Physics of Solids, 33(3), 215-226.

Consoli, N. C., Schnaid, F., & Milititsky, J. (1998). Interpretation of plate load tests on residual soil site. Journal of Geotechnical and Geoenvironmental Engineering, 124(9), 857-867.

Costa Filho, L. M., Doebereiner, L., De Campos, T. M. P. & Vargas Jr., E. (1989). Fabric and engineering properties of saprolites and laterites. General report/Discussion Session 6 - Invited lecture. Proc. 12th ICSMFE. Rio de Janeiro. Vol. 4, 2463–2476 .

De Mello, V. F. B. (1972). Thoughts on soil engineering applicable to residual soils. Proc. 3rd Southeast Asian Conf. on Soil Engineering, Hong Kong, 5–34.

De Oliveira, C. P. (2000). Estudo do comportamento tensão-deformação-resistência de um solo residual de biotita gnaisse saturado. Dissertação (Mestrado em Engenharia) – Curso de Pós-Graduação em Engenharia Civil . Pontifícia Universidade Católica do Rio de Janeiro, Rio de Janeiro, 114 p.

Duarte I.M.R., Rodrigues C.M.G. (2017) Residual Soils. In: Bobrowsky P., Marker B. (eds) Encyclopedia of Engineering Geology. Encyclopedia of Earth Sciences Series. Springer, Cham

Escalaya, M. R. A. (2016). Avaliação do efeito de aumento de poropressão nas características de resistência de três solos tropicais. Tese de Doutorado –

Curso de Pós-Graduação em Engenharia Civil . Pontifícia Universidade Católica do Rio de Janeiro, Rio de Janeiro, 278 p.

Fookes, P. G. (Ed.). (1997). Tropical residual soils: A Geological Society Engineering Group working party revised report. Geological Society of London.

Francisca, F. M., & Bogado, G. O. (2019). Weathering effect on the small strains elastic properties of a residual soil. Geotechnical and Geological Engineering, 37(5), 4031-4041.

Futai, M. M. (2002). "Theoretical and experimental study of unsaturated tropical soil behavior: Applied a gully case." PhD thesis, COPPE Federal University of Rio de Janeiro (in Portuguese).

Futai, M. M, Almeida, M. S. S. & Lacerda, W. A. (2004). Yield, strength and critical state conditions of a tropical saturated soil. J. Geotech. Geoenviron. Engng 130, No. 11, 1169–1179.

Futai, M. M., Cecilio , M. O. & Abramento, M. (2012). Shear Strength and Deformability of Residual Soils from the Sao Paulo Metropolitan Area. In Negro, A. et al. (eds.) Twin Cities - Soils from Sao Paulo and Curitiba Metropolitan Areas, Chapter 7, D'Livros.

Gan, J. K., & Fredlund, D. G. (1996). Shear strength characteristics of two saprolitic soils. Canadian Geotechnical Journal, 33(4), 595-609.

Garga, V. K. (1988). Effect of sample size on shear strength of basaltic residual soils. Canadian Geotechnical Journal, 25(3), 478-487.

Garga, V. K., & Seraphim, L. A. (1975). A note on some observations on a migmatitic residual soil from Rio de Janeiro. Soils and foundations, 15(4), 1-11.

Ibañez, J. P. (2008). Modelagem micro-mecânica discreta de solos residuais, Tese (Doutorado em Engenharia Civil) – Curso de Pós-Graduação em Engenharia Civil. Pontifícia Universidade Católica do Rio de Janeiro, Rio de Janeiro, 394 p.

Kim, M. K., & Lade, P. V. (1988). Single hardening constitutive model for frictional materials: I. Plastic potential function. Computers and Geotechnics, 5(4), 307-324.

Lacerda, W. A. (2010). Shear strength of soils derived from the weathering of granite and gneiss in Brazil. in Calcaterra, D. & Parise, M. (eds) Weathering as a Predisposing Factor to Slope Movements. Geological Society, London, Engineering Geology Special Publications, 23, 167–182.

Lade, P. V. (1977). Elasto-plastic stress-strain theory for cohesionless soil with curved yield surfaces. International Journal of Solids and Structures, 13(11), 1019-1035.

Lade, P. V., & Kim, M. K. (1988). Single hardening constitutive model for frictional materials II. Yield critirion and plastic work contours. Computers and geotechnics, 6(1), 13-29.

Leroueil, S., & Vaughan, P. R. (1990). The general and congruent effects of structure in natural soils and weak rocks. Géotechnique, 40(3), 467-488.

Maccarini, M. (1980). Ensaios triaxiais e cisalhamentos direto de um solo residual jovem, derivado de gneisse. Dissertação (Mestrado em Engenharia) – Curso de Pós-Graduação em Engenharia Civil. Pontifícia Universidade Católica do Rio de Janeiro, Rio de Janeiro, 276 p.

Maccarini, M. (1987). Laboratory Studies of a weakly bonded artificial soil. Ph. D. Thesis, Imperial College of Science and Technology, London U.K. 323 p.

Martins, F. B., Ferreira, P. M. V., Flores, J. A. A., Bressani, L. A., & Bica, A. V. D. (2005). Interaction between geological and geotechnical investigations of a sandstone residual soil. Engineering Geology, 78(1–2), 1–9.

Massey, J. B., Irfan, T. Y. & Cipullo, A. (1989). The characterization of granitic saprolitic soils. 12th ICSMFE. Rio de Janeiro, vol. 6, pp 533-542.

Mendoza, C., Farias, M. & P. da Cunha, R. (2014). Validación de modelos constitutivos avanzados de comportamiento mecánico para la arcilla estructurada de Brasilia. Obras y Proyectos 15, 52-70

Mendoza, C., Muniz de Farias, M. (2020). Critical state model for structured soil. Journal of Rock Mechanics and Geotechnical Engineering, 12, pp. 630-641.

Puppi, R. F. K., Hecke, M. B., & Romanel, C. (2018). MCC Hyperplastic constitutive model with coupled damage applied to structured soils. Geotecnia, 142, pp. 35-61. (in Portuguese)

Reis, R. M. (2004) Comportamento tensão-deformação de dois horizontes de um solo residual de gnaisse. Tese (Doutorado) – Escola Politécnica de São Carlos-Universidade de São Paulo, São Carlos, 198 p.

Rocchi, I., & Coop, M. R. (2015). The effects of weathering on the physical and mechanical properties of a granitic saprolite. Géotechnique, 65(6), 482-493.

Santos, O.F., Lacerda, W.A. & Ehrlich, M. (2020). Effects of Cyclic Variations of Pore Pressure on the Behaviour of a Gneiss Residual Soil. Geotech Geol Eng

Vargas, M. (1953): Some engineering properties of residual clay softs occuring in Southern Brazil, Proc. 3rd int. conf. S.M.F.E. Zurich 1, 67-71

Vaughan, P. R., & Kwan, C. W. (1984). Weathering, structure and in situ stress in residual soils. Géotechnique, 34(1), 43-59.

Vaughan, P. R., Maccarini, M., & Mokhtar, S. M. (1988). Indexing the engineering properties of residual soil. Quarterly Journal of Engineering Geology and Hydrogeology, 21(1), 69-84.

Viana da Fonseca, A. & Coutnho, R. Q. (2008). Characterization of residual soils. Keynote Lecture, in: Huang, A-B & Mayne, P. (eds.) Proceedings of the 3rd International Conference on Site Characterization (ISC'3), 1–4 April 2008, Taiwan. 195–248.

Wesley, L. D. (1990). Influence of structure and composition on residual soils. Journal of geotechnical engineering, 116(4), 589-603.

Wesley, L. (2009). Behaviour and geotechnical properties of residual soils and allophane clays. Obras y proyectos, 6, 5-10.

Wood, D. M. (1990). Soil behaviour and critical state soil mechanics. Cambridge university press.

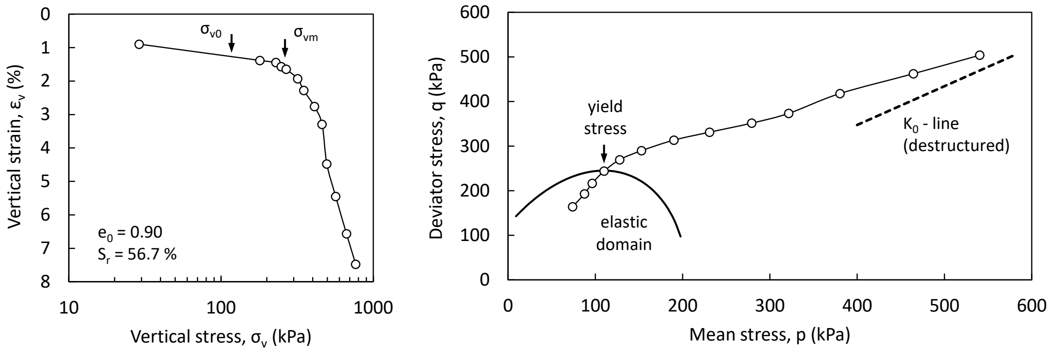

(a) **(b)**

Figure 1. K0 compression test on gneissic residual soil. Adapted from Maccarini (1980, 1987).

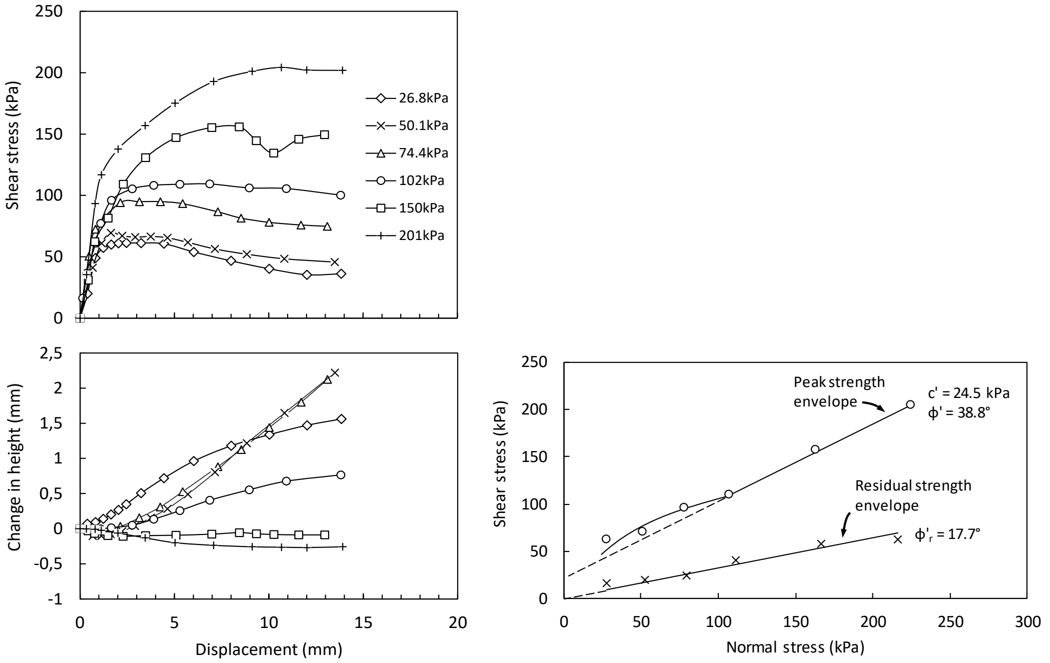

(a) **(b)**

Figure 2. Drained direct shear test on granite saprolitc soil from Duque de Caxias, Rio de Janeiro (after Escalaya, 2016). (a) Stress-displacement curves. (b) Peak and residual strength envelopes.

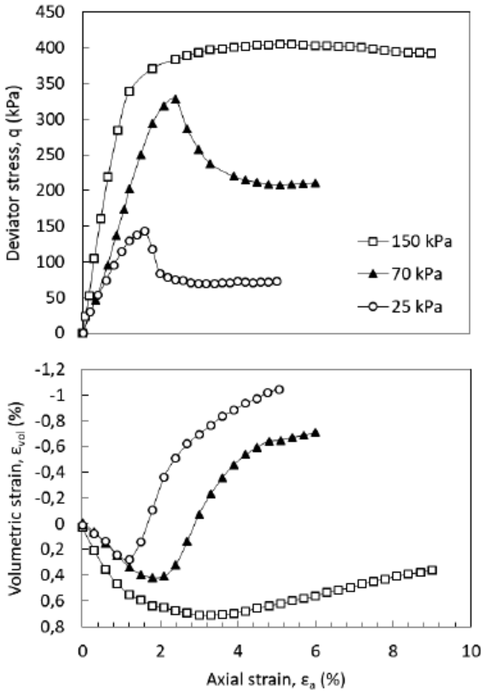

Figure 3. Drained triaxial compression test on intact young residual soil derived from biotite-gneiss. Adapted from De Oliveira (2000).

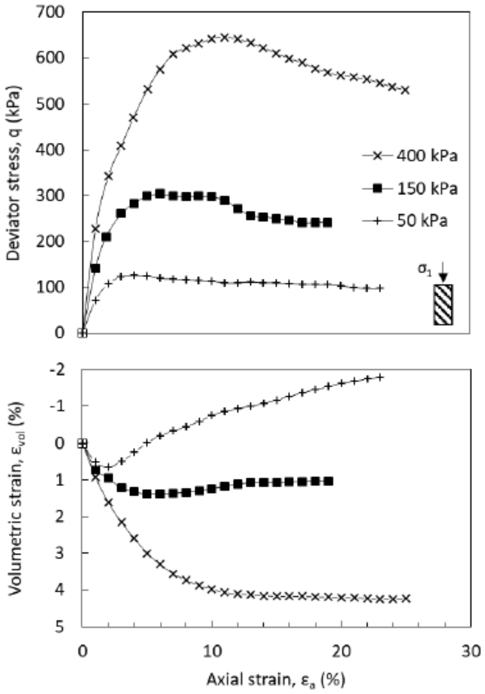

Figure 4. Drained triaxial compression test on young residual soil from gneiss with bands oriented as in the field. Adapted from Reis (2004).

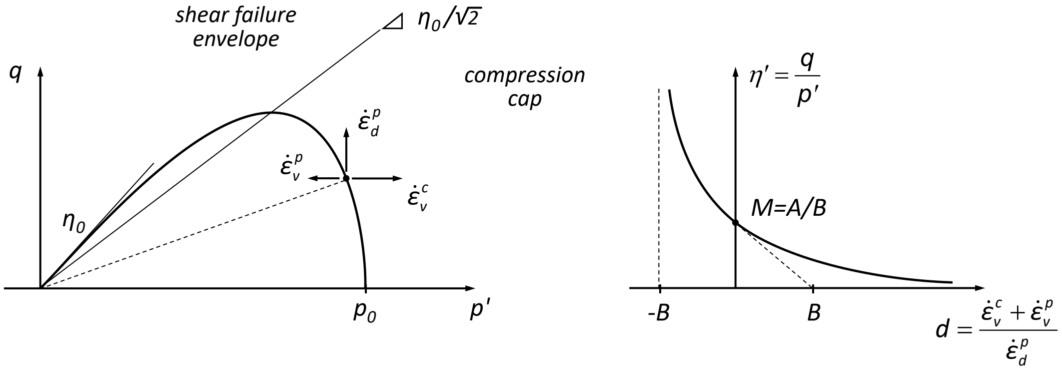

Figure 5. Yield surface, flow vectors and stress-dilatancy relationship.

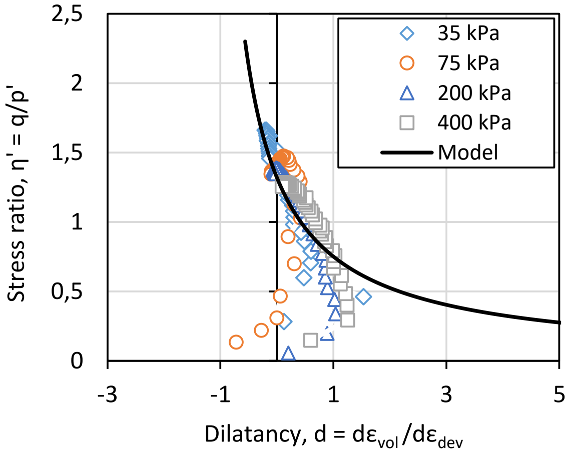

Figure 6. Determination of model parameters A = 1.74 and B = 1.32 from the stress-dilatancy relationship of Ouro Preto residual soil.

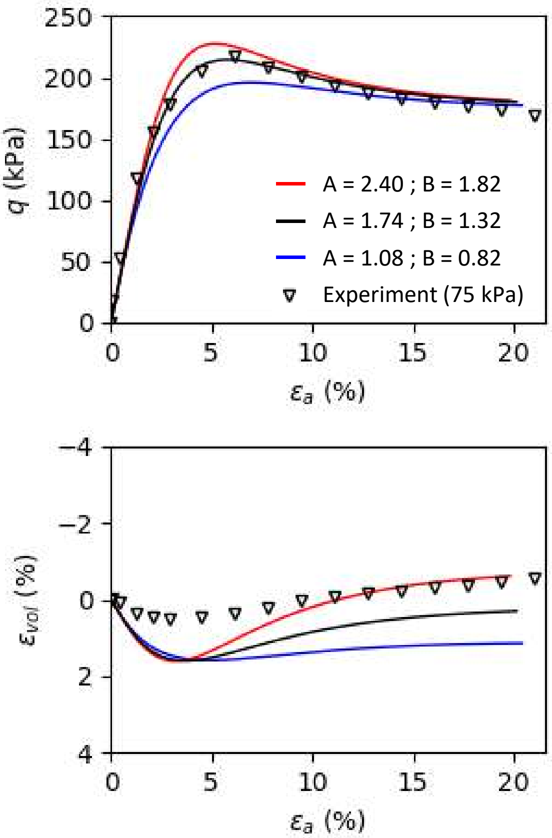

Figure 7. Effect of parametric variation on comparison of model simulations and experimental results for drained triaxial compression under 75 kPa of confining pressure.

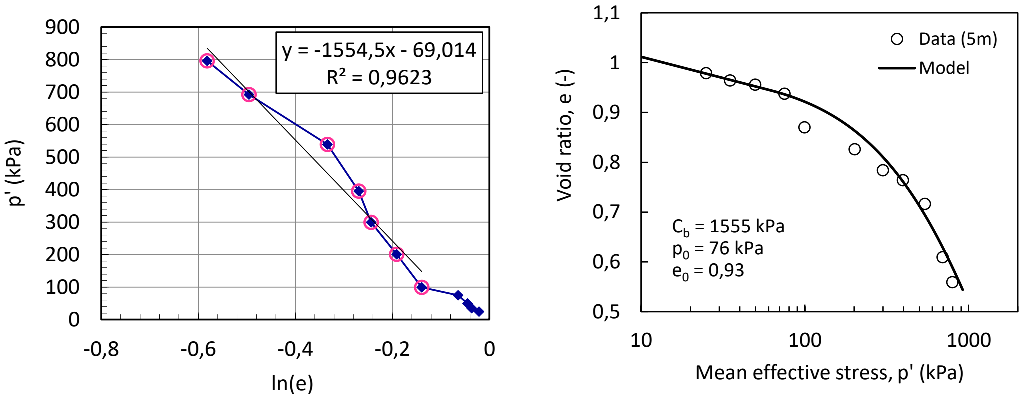

Figure 8. Calibration of compression modulus and comparison with experimental results for Ouro Preto residual soil. Data points are taken from triaxial experiments at the end of isotropic consolidation stage.

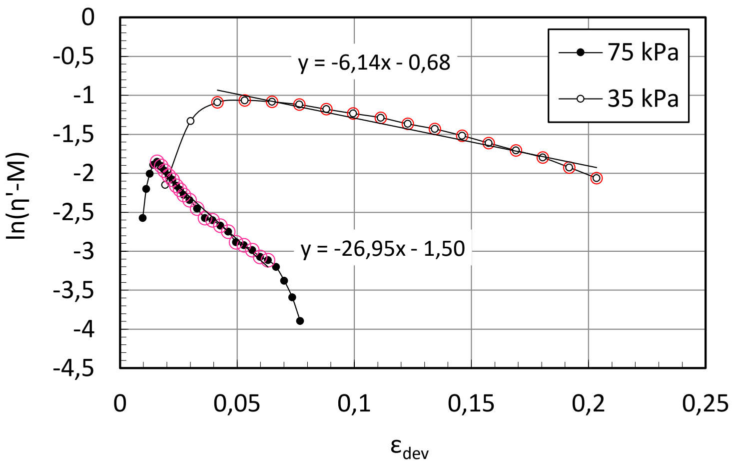

Figure 9. Calibration of softening rule with post-peak reponses from drained triaxial tests conducted at low confining pressures.

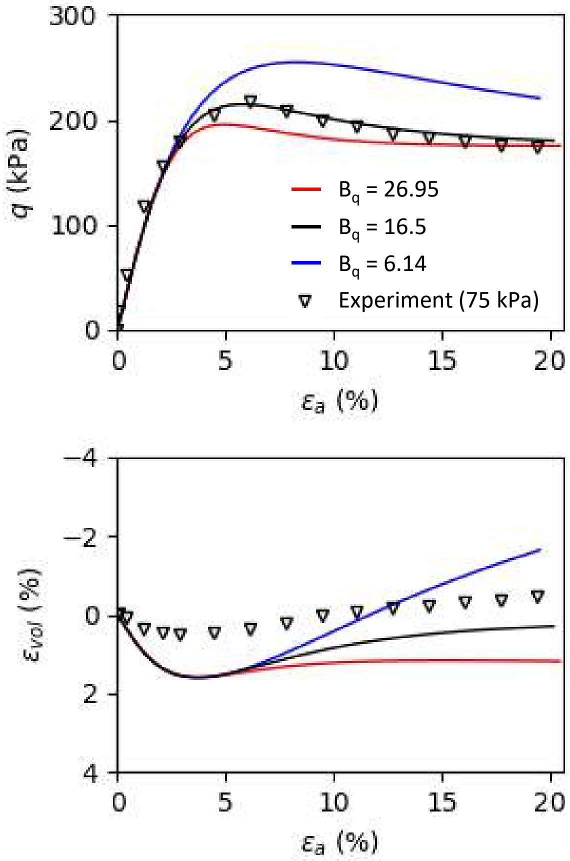

Figure 10. Effect of parametric variation on comparison of model simulations and experimental results for drained triaxial compression under 75 kPa of confining pressure.

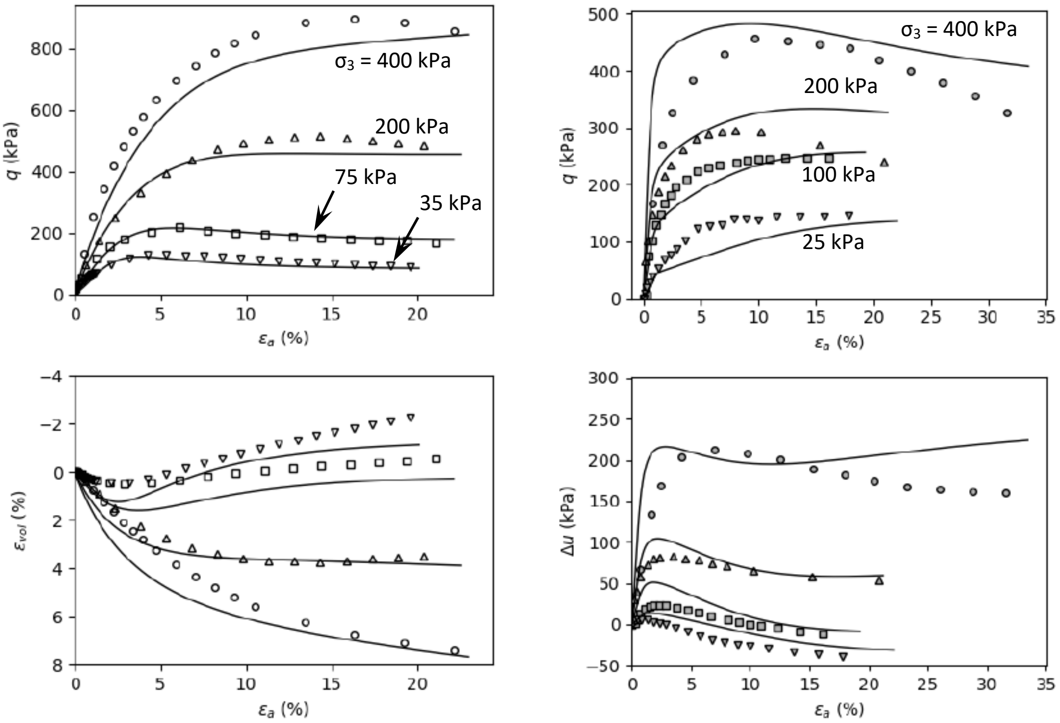

(a) (b)

Figure 11. Comparison between experimental data from Futai et al. (2004) and model simulations for Ouro Preto residual soil. (a) Consolidated drained triaxial compression tests. (b) Consolidated undrained triaxial compression tests.

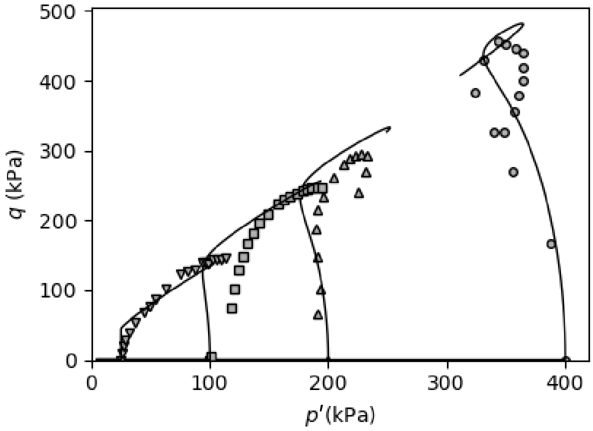

Figure 12. Comparison of measured and predicted effective stress paths for consolidated undrained triaxial compression tests on Ouro Preto residual soil.

Table 1. Summary of parameter values for Ouro Preto residual soil.

Model component	Parameters
Elastic behavior	$\kappa' = 0.018$ $\nu' = 0.15$
Hardening parameters	$p_0 = 61$ kPa $\eta_0 = 1.9$
Inelastic flow	$A = 1.74$ $B = 1.32$
Hardening/softening law	C_b,= 1555 kPa $e_0 = 0.947$ $B_q = 16.5$

7.2
Compression models from elementary incremental laws

Compression models from elementary incremental laws

Alessandro Cirone[1,*] and Eurípedes Vargas Jr[1]

[1] Department of Civil and Environmental Engineering, Pontifical Catholic University of Rio de Janeiro
Rua Marquês de São Vicente 225, 22451-900, Rio de Janeiro (Brazil)
*a.cirone@aluno.puc-rio.br

Abstract Five compression laws were formulated using simple incremental relationships involving fundamental index properties of porous media such as porosity and void ratio. Models are presented in terms of void ratio-effective stress relationship and porosity-depth trends. All theoretical expressions were derived by assuming suitable incremental compression laws. Comparison with experimental data indicates that the models can describe a number of features of the behavior of sand and sedimentary rocks.

Keywords: compressibility, porosity, constitutive relations

1 Introduction

Under the assumption that solid particles are incompressible, a porous material compresses if the volume of its pores reduces. Volumetric strains occurring in such a way result in a change of porosity or, equivalently, change of void ratio. Sometimes some simplification results from working in terms of the void ratio rather than the porosity, yet both index properties quantify the same soil phase, i.e. the volume of voids, and the use of one respect to another is indifferent. The final goal of the proposed approach is to derive a new class of compression models based on simple index properties suitable for porous materials.

2 Some remarks on the relationship between void ratio and effective stress

2.1 Definitions

Experimental data are usually presented in terms of void ratio (or strain) versus effective stress, using the logarithmic scale for the stress. The gradient of the compression curve in the $e - \ln \sigma$ plot is:

$$\lambda = -\frac{de}{d\ln\sigma} = -\sigma\frac{de}{d\sigma} \tag{1}$$

that depends on the current effective stress and on the derivative of the void ratio-effective stress relation.

The compressibility is defined as the change in bulk volume resulting from the effective pressure applied to the soil with respect to its bulk volume, that is:

$$\beta = -\frac{1}{V}\frac{dV}{dp} = \frac{d\varepsilon_v}{dp} \tag{2}$$

where the sign convention adopts strains and stresses as positive in compression. The minus sign is introduced because an increase in effective pressure results in a reduction of the entire bulk volume of the soil. The compressibility, in general, is not constant and decreases as the effective stress increases.

2.2 Compression models from literature

The most used relation to describe the results of oedometer tests on normally consolidated soils is:

$$e = e_0 - C_c \log_{10}\frac{\sigma}{\sigma_0} = e_0 - \lambda \ln\frac{p}{p_0} \tag{3}$$

the slope $C_c = \Delta e / \Delta \log_{10}\sigma$ is the compression index and $\lambda \cong C_c / 2.3$ is the slope of the normal compression line when natural logarithm is assumed for the effective stress. It is well established that a relation of this type adequately describes the behavior of most clays. However, over a wide range of values of pressures, the e – log σ compression curve is non-linear, and C_c (or λ) decreases continuously with increasing the consolidation pressure (Terzaghi et al., 1996). Butterfield (1979) and Hashiguchi (1995) pointed the limitations of Equation (3). The major shortcoming is that the void ratio becomes negative for effective stresses greater than $\sigma_0 \exp(e_0 / \lambda)$.

Based on empirical evidence, Butterfield (1979) showed that this problem can be partially overcome by using a bilogarithmic expression between the specific volume, $v = 1 + e$, and the effective stress:

$$\ln v = \ln v_0 - \lambda \ln(p / p_0) \tag{4}$$

although the linearity between ln(*1+e*) and ln *p* does not generate negative specific volumes for large values of pressures, Equation (3) still forecasts negative void ratios beyond $\sigma_0\, e_0^{1/\lambda}$.

Following the same rationale, Pestana and Whittle (1995) and Sheng et al. (2008) proposed an isotropic compression model based on a double logarithmic relationship between the void ratio and the mean stress, ensuring that the void ratio never becomes negative at high stresses. Actually, there exist a number of different empirical-based formulations in literature. They are listed in Table 1, which provides an overview of the available effective stress-void ratio relationships to model the compression behavior of clays, sands and mine tailings.

Table 1 Void ratio-effective stress relationships from literature.

Type	Equation	Slope $^{(a)}$	Reference
e – ln p	$e = N - \lambda \ln p$	λ	Schofield and Wroth (1964)
ln v – ln p	$\ln\left(\frac{v}{v_0}\right) = -\lambda \ln\left(\frac{p}{p_0}\right)$	λv	Butterfield (1979)
ln e – ln p	$\ln e = \ln N - \lambda \ln(p + p_r)$	λe	Sheng et al. (2008)
e – exp(-σ)	$e = (e_0 - e_\infty)\exp(-\lambda\sigma) + e_\infty$	$\lambda(e - e_\infty)\sigma$	Gibson et al. (1981)
power law (1)	$e = A\sigma^{-B}$	Be	Carrier et al. (1983)
power law (2)	$e = A(\sigma + Z)^{-B}$	$Be\frac{\sigma}{\sigma + Z}$	Liu and Znidarcic (1991)
e – exp(-p^n)	$e = e_0 \exp[-(3p_s / h_s)^n]$	N/A	Bauer (1996)

(a) Gradient of the plot of void ratio against natural logarithm of effective stress.

3 Incremental laws to derive a new class of relationships

The first compression law is derived by assuming that the reduction in void ratio, – *de*, due to the application of an infinitesimal increase in mean effective stress, *dp*, is proportional to current value of the void ratio itself, *e*. The incremental law is then written as follows:

$$-de = \frac{e}{K_b}dp \tag{5}$$

where a constant of proportionality has been introduced, K_b, with the dimension of a stress. According to Equation (1), the corresponding gradient of the compression curve in the e – ln p plot is $\lambda = e\,p/K_b$. Dividing both sides of Equation (5) by $1+e$ and recalling that $d\varepsilon_v = -\,de/(1+e)$, the expression for the compressibility is obtained:

$$\beta = \frac{d\varepsilon_v}{dp} = \frac{\phi}{K_b} \tag{6}$$

which states that the compressibility, $\beta = d\varepsilon_v /dp$, as defined in Equation (2), is proportional to the current porosity, $\phi = e/(1+e)$. This is equivalent to say that a porous material with a denser granular pack is stiffer. Equation (5) can be easily integrated together with the initial condition $e(p_0) = e_0$, to obtain the equation for the normal compression line:

$$e = e_0 \exp\left(-\frac{p - p_0}{K_b}\right) \tag{7}$$

This void ratio-effective stress relationship is of exponential type, resembles those proposed by Gibson et al. (1981) and Bauer (1996) and arises from the simple assumption that the compressibility of a porous material is proportional to its porosity. Equation (7) predicts a linear relationship between the mean effective stress and the logarithm of void ratio. The value of modulus K_b coincides with the slope of the straight line obtained from isotropic compression test if ln e is plotted against p. This experimental procedure can be applied to intact or reconstituted soil samples for geotechnical analyses purpose.

The model can be also calibrated from measured porosity-depth trends of normally consolidated sediments. To derive an expression relating the depth of burial to the porosity, consider the vertical indefinite equilibrium of a submerged material in which the vertical stress acts as principal stress:

$$\frac{d\sigma_z}{dz} = \gamma' = (\gamma_s - \gamma_w)(1 - \phi) = \frac{\gamma_s - \gamma_w}{1 + e} \tag{8}$$

the effective stress change is equal to the change of the lithostatic minus the hydrostatic pressure. Equations (5) and (8) may be combined and easily integrated if the coefficient of earth pressure at rest, K_0, is assumed constant along the normal compression line. For sake of clarity, the step-by-step calculations are herein presented. From Equations (5) and (8), the following identity holds:

$$\frac{de}{e} = -\frac{dp}{K_b} = -\frac{1 + 2K_0}{3}\frac{d\sigma_z}{K_b} = -\frac{1 + 2K_0}{3}\frac{\gamma_s - \gamma_w}{K_b}\frac{dz}{1 + e}$$

and introducing

$$b = \frac{1 + 2K_0}{3} \cdot \frac{\gamma_s - \gamma_w}{K_b}$$

the integral

$$\int_{e_0}^{e} \frac{1 + e}{e} de = -b\int_0^z dz$$

results in the following:

$$e - e_0 + \ln\left(\frac{e}{e_0}\right) = -b\, z \tag{9}$$

The analytical expression for the void ratio-depth relation is very advantageous to determine the compression laws parameters when log or well data are available in terms of porosity versus depth rather than for porosity versus effective stress.

Analogously, the expressions listed in Table 2 were derived according to the same theoretical framework by assuming an incremental law as starting point for all the mathematical derivations. Remarkable results are:

- analytical expressions consist of a family of functions suitable to describe the behavior of porous materials in hydrostatic compression (Figure 1 shows that they have similar shape);
- as shown previously, the Model 1 predicts a void ratio-effective stress relationship of exponential type similar to those proposed by Gibson et al. (1981) and Bauer (1996);
- Model 3 results in simple exponential expressions for the normal compression line and depth profile. The porosity–effective stress function is similar to that proposed by Smith (1971);
- Model 4 predicts a simple exponential decrease of porosity with depth as stated by Athy's law (Athy, 1930).

Table 2. Summary of derived compression models.

No.	Compression law	Compressibility	Normal compression line	Depth profile
1	$de = -\frac{e}{K_b} dp$	$\beta = \frac{\phi}{K_b}$	$e = e_0 \exp\left(-\frac{p - p_0}{K_b} \right)$	$e - e_0 + \ln\left(\frac{e}{e_0} \right) = -bz$
2	$de = -\frac{\phi}{K_b} dp$	$\beta = \frac{\phi}{(1+e) K_b}$	$e - e_0 + \ln\left(\frac{e}{e_0} \right) = -\frac{p - p_0}{K_b}$	N/A
3	$d\phi = -\frac{\phi}{K_b} dp$	$\beta = \frac{e}{K_b}$	$\phi = \phi_0 \exp\left(-\frac{p - p_0}{K_b} \right)$	$e = e_0 \exp(-bz)$
4	$d\phi = -\frac{e}{K_b} dp$	$\beta = \frac{e}{(1-\phi) K_b}$	$\phi_0 - \phi + \ln\left(\frac{\phi}{\phi_0} \right) = -\frac{p - p_0}{K_b}$	$\phi = \phi_0 \exp(-bz)$
5	$d\phi = -\frac{e}{1-\phi} \frac{dp}{K_b}$	$\beta = \frac{e}{(1-\phi)^2 K_b}$	N/A	$\phi_0 - \phi + \ln\left(\frac{\phi}{\phi_0} \right) = -bz$

4 Comparison with experimental data

Due to their simplicity, Models 1 and 3, which are presented in Table 2, are compared and validated against experimental data to show their flexibility in capturing the observed experimental behavior. The void ratio-effective stress relationship predicted by Model 3 is compared with a series of hydrostatic compression tests on Sacramento River sand carried out by Lee and Seed (1967). The soil was tested under four different initial relative densities. For each of them, calibration consisted in applying a simple linear regression ($y = mx + q$) to the straight portion of the experimental curve in the ln $\phi - p$ plot, as shown in Figure 2(a). The modulus K_b coincides with the slope of the straight line, while the initial porosity is simply calculated as $\phi_0 = \exp(-q/m)$. Figure 2(b) shows that the predictions are in very good agreement with the measured data.

A comparison between compressibility data on limestones from Vajdova et al. (2004) and predictions according to Model 1 and Model 3 is shown in Figure 3. It can be seen that the overall trend for compressibility to increase with increasing porosity is well predicted. Model No. 1 gives a linear approximation, while Model No. 3 gives a non-linear trend.

Figure 4 shows a theoretical porosity-depth trend according to Model 3 compared with observed porosities (data points from Ramm, 1991) in near hydrostatically pressured muddy sandstones from the Norwegian continental shelf. It is shown that the predictions are again in relatively good agreement with the measured data.

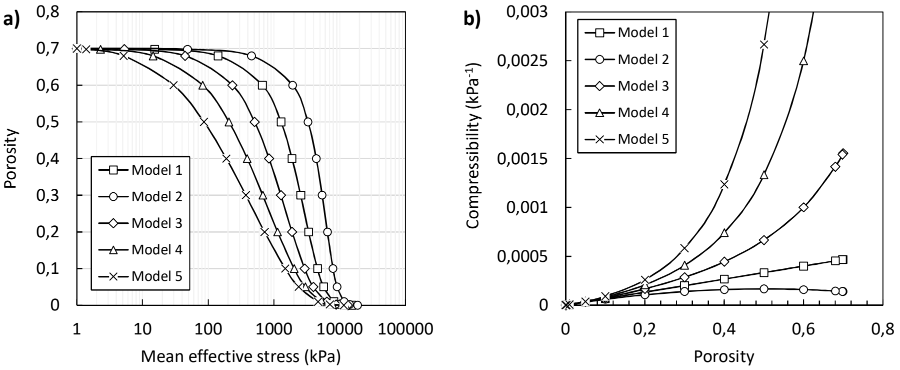

Fig. 1 Comparison of compression models from present work. (a) Normal compaction curves and (b) compressibility curves with the following parameters: $\phi_0 = 0.7$, $p_0 = 1$ kPa, $K_b = 1500$ kPa, $\gamma_s = 26$ kN/m^3, $\gamma_w = 10$ kN/m^3, $K_0 = 0.7$.

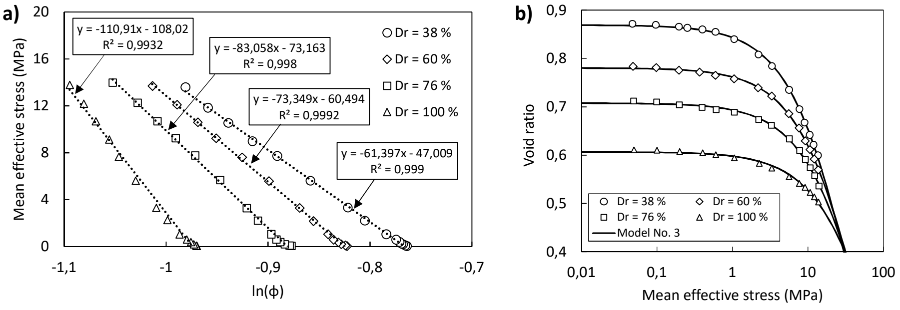

Fig. 2 Behavior of Sacramento River sand in hydrostatic compression (data from Lee and Seed, 1967). (a) Calibration of Model No.3. (b) Comparison between observed and predicted behavior.

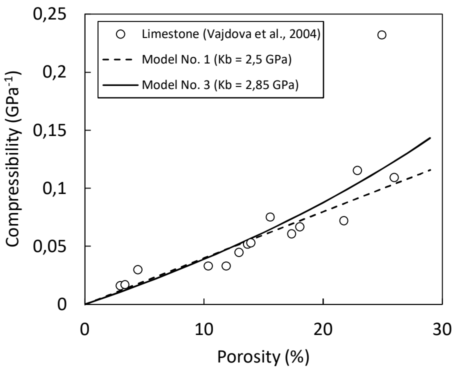

Fig. 3 Compressibility of limestones as function of porosity. Data from Vajdova et al. (2004) are compared with predictions based on Model No. 1 and Model No. 3.

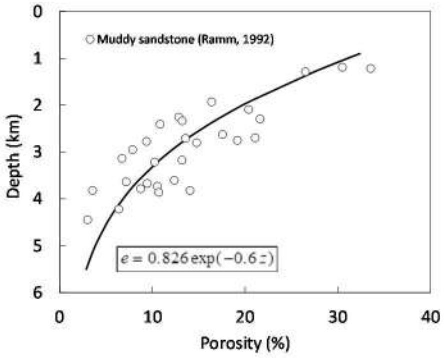

Fig. 4 Predicted and measured porosity-depth curve for muddy sandstones from the Norwegian continental shelf. The data points included (from Ramm, 1991) are 75 percentile porosity versus mean depth.

5 Conclusion

A family of compression curves were proposed for modeling the hydrostatic compression of porous materials. The elementary compression laws have been formulated in terms of fundamental index properties such as porosity and void ratio. The determination of the model parameters can be made by means of a hydrostatic compression test or from measured porosity-depth trends. In particular, calibration is trivial for Model 1 and Model 3. From comparison presented in the paper, it appears that the proposed models are suitable for the description of volume behavior of sands and sedimentary rocks, capturing the observed interrelationships between compressibility, porosity and depth of burial. Extension and further elaboration of the proposed model may be achieved by rejecting the assumption of incompressible solid grains, especially for modeling the volume behavior under high stress levels.

References

Athy, L. F. (1930). Density, porosity, and compaction of sedimentary rocks. Aapg Bulletin, 14(1), 1-24.

Bauer, E. (1996). Calibration of a comprehensive hypoplastic model for granular materials. Soils and foundations, 36(1), 13-26.

Butterfield, R. (1979). A natural compression law for soils (an advance on e-log p'). Géotechnique, 29(4).

Carrier III, W. D., Bromwell, L. G., & Somogyi, F. (1983). Design capacity of slurried mineral waste ponds. Journal of Geotechnical Engineering, 109(5), 699-716.

Gibson, R. E., Schiffman, R. L., & Cargill, K. W. (1981). The theory of one-dimensional consolidation of saturated clays. II. Finite nonlinear consolidation of thick homogeneous layers. Canadian geotechnical journal, 18(2), 280-293.

Hashiguchi, K. (1995). On the linear relations of v–ln p and ln v–ln p for isotropic consolidation of soils. International journal for numerical and analytical methods in geomechanics, 19(5), 367-376.

Lee, K. L., & Seed, H. B. (1967). Drained strength characteristics of sands. Journal of Soil Mechanics & Foundations Div.

Liu, J. C., & Znidarčić, D. (1991). Modeling one-dimensional compression characteristics of soils. Journal of Geotechnical Engineering, 117(1), 162-169.

Pestana, J. M., & Whittle, A. J. (1995). Compression model for cohesionless soils. Géotechnique, 45(4), 611-631.

Ramm, M. (1992). Porosity-depth trends in reservoir sandstones: theoretical models related to Jurassic sandstones offshore Norway. Marine and Petroleum Geology, 9(5), 553-567.

Schofield, A., & Wroth, P. (1968). Critical state soil mechanics (Vol. 310). London: McGraw-Hill.

Sheng, D., Yao, Y., & Carter, J. P. (2008). A volume–stress model for sands under isotropic and critical stress states. Canadian Geotechnical Journal, 45(11), 1639-1645.

Smith, J. E. (1971). The dynamics of shale compaction and evolution of pore-fluid pressures. Journal of the International Association for Mathematical Geology, 3(3), 239-263.

Terzaghi, K., Peck, R. B., & Mesri, G. (1996). Soil mechanics in engineering practice. John Wiley & Sons.

Vajdova, V., Baud, P., & Wong, T. F. (2004). Compaction, dilatancy, and failure in porous carbonate rocks. Journal of Geophysical Research: Solid Earth, 109(B5).

8
Conclusion

The work described in this thesis had the main purpose of developing constitutive models specific for regional soils and soft rocks encountered in Brazil. In doing so, four main topics were addressed. Firstly, the fundamentals of large deformation analysis were critically reviewed; secondly, the work focused on modeling the structure degradation according to the bonded soil model; thirdly, viscoplasticity theory was explored to account for creep behavior of soft clay and, lastly, a comprehensive finite element implementation was formulated to perform pertinent numerical analyses. The main results obtained during this doctoral research are summarized in the following, along with final remarks and recommendations for future works.

The review of large deformation theory included in this thesis is far from complete or even comprehensive, but rather is intended to be representative of the areas of agreement between several existing schools of plasticity. At first, an important difference with regard to the infinitesimal theory is the introduction of the deformation gradient for the description of a deforming body, along with the distinction between the undeformed and deformed configurations. In this manner, the notion of the unstressed intermediate configuration to represent the permanent (plastic) deformation gained popularity and became well established in terms of the multiplicative decomposition of the deformation gradient. Issues regarding the nonuniqueness of the multiplicative decomposition have been discussed. This approach to finite strain elastoplasticity does not prevent the additivity of strains, provided that all strains – the total, the elastic and plastic parts – are measured with respect to the same configuration. Moreover, some basic ingredients in the presence of finite elastoplastic deformation were addressed – such as the exponential integration of the flow rule – and existing computational formulations that preserve the small strain format were summarized. In the light of these remarks, a constitutive model developed in the framework of the infinitesimal strain theory can be extended to include finite strains by the choice of an appropriate kinematic description of motion, specific hardening laws and suitable strain measures conjugate to the operating stresses.

Concerning the constitutive modeling of geomaterials, a review of mathematical expressions from literature has shown that, at a first approximation, the yield surface has the shape of a teardrop and the plastic potential is non-associated and well represented by Rowe's stress-dilatancy relation. Two general expressions for the yield function and plastic potential were proposed by the author. They are reported in Eqs. 3-8 and 3-24. Destructuration, i.e. the disintegration of interparticle bonds, was included according to the fundamental concepts introduced by Gens and Nova (1993). This led to the formulation of the R-Soil model as a constitutive model for both soils and rock. The model has a number of features such as non-associated behavior, intermediate stress influence and structure degradation. The R-Soil model was validated against experimental data from laboratory tests conducted on Vila Velha sandstone. The determination of model parameters was illustrated step-by-step. However, to distinguish the deformations arising from particle rearrangement from those resulting from bonds degradation and particle breakdown, two flow rules were introduced and inelastic strains were decomposed accordingly. This approach was used to model the behavior of Ouro Preto residual soil in triaxial compression resulting in appreciable predictions as displayed in the results section of the attached paper. Shear strength degradation was modeled by means of a softening law associated to plastic deviatoric strains in the shear failure envelope. Behavior in hydrostatic compression was modeled with a novel hardening law associated solely to collapse strains resulting from yielding of soil structure.

An elasto-viscoplastic constitutive model based on Modified Cam Clay and Perzyna's viscoplasticity theory was adopted to simulate the laboratory behavior of Sarapuí soft clay. Perzyna's approach was chosen because it predicts all distinctive features deriving from the pronounced viscous behavior of the soft clay, i.e. stress relaxation, creep and rate-dependent behavior in both drained and undrained compression. A novel closed form solution for the theoretical interpretation of the Undrained Hydrostatic Relaxation Test was developed. This provided a better insight into the creep characteristics of Sarapuí clay and allowed a clear examination of the viscous nucleus down to very low viscoplastic strain rates. Analysis of the experimental data suggested a viscous nucleus of the exponential type. The results of the numerical simulations indicated that the proposed constitutive model is capable of reproducing pratically all the characteristics of the experimental curves, requiring only two additional parameters compared to ordinary Modified Cam Clay. It should be noted that the model does not provide reliable prediction for highly overconsolidated states.

Emphasis was placed on the algorithms for the integration of constitutive equations. After a detailed study of the various return mapping schemes proposed in the literature, forward and backward Euler integration schemes were formulated in order to account for nonlinear elastic behavior, bond degradation and viscoplastic behavior. Numerical integration in the presence of a nonlinear elastic predictor was performed by means of the secant elastic material stiffness matrix. Specific integration schemes were developed for the integration of viscoplastic strains. Implicit and explicit integration scheme have been addressed under the usual strain-driven problem. To simulate laboratory experiments without the aid of finite elements, integration under mixed control was also addressed. The work culminated with the implementation of the aforementioned constitutive models in the commercial finite elements software PLAXIS.

8.1
Recommendations for future work

The studies conducted in this thesis dealt with the idealization, formulation, implementation and verification of constitutive models. A number of features were modeled and implemented, some of which have come from existing constitutive models, others have been originated from author's research. Further improvements are still possible to produce very general constitutive models, for both soft clay and residual soil. These include, for example, the extension to unsaturated state, the implementation of intrinsic and structural anisotopy and the elastic stiffness degradation due to mechanical damage. Moreover, a viscoplastic structured soil model could have been developed joining together Perzyna's and Nova's approaches. Because in this thesis only laboratory test data were used, future research could be directed towards the application of these constitutive models to large scale geotechnical problems, validating numerical predictions against field monitoring data. In the context of the stability analysis of mine tailings, it is interesting to note that metastable soils could have been modeled with the R-Soil model.

Bibliography

ADACHI, T.; OKA, F.. **Constitutive equations for normally consolidated clay based on elasto-viscoplasticity**. Soils and Foundations, 22(4):57–70, 1982.

AGUIAR, V. N.. **Contribuição ao estudo das relações tensão-deformação-resistência-tempo das argilas moles**. PhD thesis, COPPE/UFRJ, Rio de Janeiro, 2014.

ALAWAJI, H.; RUNESSON, K.; STURE, S. ; AXELSSON, K.. **Implicit integration in soil plasticity under mixed control for drained and undrained response**. International journal for numerical and analytical methods in geomechanics, 16(10):737–756, 1992.

ALMEIDA, M. S. S.. **The undrained behaviour of the rio de janeiro clay in the ligth of critical state theories**. Solos e Rochas, 5:3–24, 1982.

ALMEIDA, M. S. S.. **Propriedades geotécnicas da argila mole do Rio de Janeiro à luz de estados críticos e correlações empríricas**. In ABMS, editor, **VII COBRAMSEF**, pages 15–24, Porto Alegre, RS, 1986. ABMS.

ALMEIDA, M. S. S.; CARVALHO, S. R. L. ; MARTINS, I. S.. **Constant rate of strain consolidation on very soft clays**. In **Int. Symposium on Compression and Consolidation of Clayey Soils**, pages 09–14, 1992.

ALMEIDA, M. S. S.; FERREIRA, C. A. M.. **Field, in situ and laboratory consolidation parameters of a very soft clay**. In **Predictive soil mechanics: Proceedings of the Wroth Memorial Symposium held at St Catherine's College, Oxford, 27-29 July 1992**, pages 73–93. Thomas Telford Publishing, 1992.

ALMEIDA, M. S. S.; MARQUES, M. E. S.. **The behaviour of sarapuí soft clay**. Characterization and engineering properties of natural soils. Edited by TS Tan, KK Phoon, DW Hight, and S. Leroueil. Swets & Zeitlinger, Lisse, the Netherlands, pages 477–504, 2003.

ASARO, R. J.. **Crystal Plasticity**. Journal of Applied Mechanics, 50(4b):921–934, 12 1983.

BARROSO, E. V.. **Avaliação de um modelo elastoplástico para estudos de produção de areia em rochas produtoras de petróleo**. PhD thesis, Pontifícia Universidade Católica do Rio de Janeiro, 2002.

BATHE, K.. **Finite Element Procedures**. Prentice Hall, 2006.

BATHE, K.-J.; RAMM, E. ; WILSON, E. L.. **Finite element formulations for large deformation dynamic analysis**. International Journal for Numerical Methods in Engineering, 9(2):353–386, 1975.

BELYTSCHKO, T.; LIU, W.; MORAN, B. ; ELKHODARY, K.. **Nonlinear Finite Elements for Continua and Structures**. Wiley, 2013.

BORJA, R.; KAVAZANJIAN, E.. **A constitutive model for the stress–strain–time behaviour of 'wet'clays**. Geotechnique, 35(3):283–298, 1985.

BORJA, R. I.. **Cam-clay plasticity, part ii: Implicit integration of constitutive equation based on a nonlinear elastic stress predictor**. Computer Methods in Applied Mechanics and Engineering, 88(2):225–240, 1991.

BORJA, R. I.. **Generalized creep and stress relaxation model for clays**. Journal of Geotechnical Engineering, 118(11):1765–1786, 1992.

BORJA, R. I.; LEE, S. R.. **Cam-clay plasticity, part 1: implicit integration of elasto-plastic constitutive relations**. Computer Methods in Applied Mechanics and Engineering, 78(1):49–72, 1990.

BRINKGREVE, R.; KUMARSWAMY, S.; SWOLFS, W.; WATERMAN, D.; CHESARU, A.; BONNIER, P. ; . **Plaxis 2016 - user manual**. PLAXIS bv, the Netherlands, 2016.

BRUHNS, O.; XIAO, H. ; MEYERS, A.. **Self-consistent eulerian rate type elasto-plasticity models based upon the logarithmic stress rate**. International Journal of Plasticity, 15(5):479–520, 1999.

BRUHNS, O. T.; MEYERS, A. ; XIAO, H.. **On non–corotational rates of oldroyd's type and relevant issues in rate constitutive formulations**. Proceedings of the Royal Society of London. Series A: Mathematical, Physical and Engineering Sciences, 460(2043):909–928, 2004.

CARVALHO, S. R. L.. **Ensaios de adensamento edométrico com taxa constante de deformação específica relacionada ao tempo na argila do sapuí**. Master's thesis, COPPE/UFRJ, Rio de Janeiro, 1989.

CASTELLANZA, R.; NOVA, R.. **Oedometric tests on artificially weathered carbonatic soft rocks**. Journal of geotechnical and geoenvironmental engineering, 130(7):728–739, 2004.

CHANG, C.; ZOBACK, M. D.. **Viscous creep in room-dried unconsolidated gulf of mexico shale (ii): Development of a viscoplasticity model**. Journal of Petroleum Science and Engineering, 72(1):50 – 55, 2010.

CIANTIA, M. O.; CASTELLANZA, R. ; FERNANDEZ-MERODO, J. A.. **A 3d numerical approach to assess the temporal evolution of settlement damage to buildings on cavities subject to weathering**. Rock Mechanics and Rock Engineering, 51(9):2839–2862, 2018.

COLLINS, I.; HOULSBY, G.. **Application of thermomechanical principles to the modelling of geotechnical materials**. Proceedings of the Royal Society of London. Series A: Mathematical, Physical and Engineering Sciences, 453(1964):1975–2001, 1997.

COLLINS, I.; MUHUNTHAN, B.. **On the relationship between stress–dilatancy, anisotropy, and plastic dissipation for granular materials**. Geotechnique, 53(7):611–618, 2003.

CRISFIELD, M. A.. **Non-linear finite element analysis of solids and structures**. John Wiley & Sons, Inc., 1991.

CRISFIELD, M. A.. **Non-linear finite element analysis of solids and structures: Advanced Topics**. John Wiley & Sons, Inc., 1997.

CUITINO, A.; ORTIZ, M.. **A material-independent method for extending stress update algorithms from small-strain plasticity to finite plasticity with multiplicative kinematics**. Engineering computations, 9:437–437, 1992.

DE BORST, R.; CRISFIELD, M. A.; REMMERS, J. J. C. ; VERHOOSEL, C. V.. **Non-linear finite element analysis of solids and structures**. John Wiley and Sons Inc., 2012.

DE SOUZA NETO, E.; PERIĆ, D.. **A computational framework for a class of fully coupled models for elastoplastic damage at finite strains with reference to the linearization aspects**. Computer Methods in Applied Mechanics and Engineering, 130(1-2):179–193, 1996.

DE SOUZA NETO, E. A.; PERIC, D. ; OWENS, D.. **Computational methods for plasticity : theory and applications**. Wiley, 2009.

DESAI, C.; ZHANG, D.. **Viscoplastic model for geologic materials with generalized flow rule**. International Journal for Numerical and Analytical Methods in Geomechanics, 11(6):603–620, 1987.

DESAI, C. S.; SIRIWARDANE, H. J.. **Constitutive laws for engineering materials with emphasis on geologic materials**. Prentice-Hall, 1984.

DI PRISCO, C.; IMPOSIMATO, S.. **Time dependent mechanical behaviour of loose sands**. Mechanics of Cohesive-frictional Materials, 1(1):45–73, 1996.

DIENES, J. K.. **On the analysis of rotation and stress rate in deforming bodies**. Acta mechanica, 32(4):217–232, 1979.

DUVAUT, G.; LIONS, J.-L.. **Inéquations en thermoélasticité et magnétohydrodynamique**. Archive for Rational Mechanics and Analysis, 46(4):241–279, 1972.

ETEROVIC, A. L.; BATHE, K.-J.. **A hyperelastic-based large strain elastoplastic constitutive formulation with combined isotropic-kinematic hardening using the logarithmic stress and strain measures**. International Journal for Numerical Methods in Engineering, 30(6):1099–1114, 1990.

FEIJÓ, R. L.. **Relação entre a compressão secundária, razão de sobreadensamento e coeficiente de empuxo no repouso**. Master's thesis, COPPE/UFRJ, Rio de Janeiro, 1991.

FODIL, A.; ALOULOU, W. ; HICHER, P.. **Viscoplastic behaviour of soft clay**. Géotechnique, 47(3):581–591, 1997.

FUNG, Y.; TONG, P.. **Classical and Computational Solid Mechanics**. Advanced series in engineering science. World Scientific, 2001.

GARCIA, S. G. F.. **Relação entre o adensamento secundário e a relaxação de tensões de uma argila mole submetida à compressão edométrica**. Master's thesis, COPPE/UFRJ, Rio de Janeiro, 1996.

GENS, A.; NOVA, R.. **Conceptual bases for a constitutive model for bonded soils and weak rocks**. In **Geotechnical Engineering of Hard Soils - Soft Rocks**, pages 485–494. Balkema, 1993.

GUIMARÃES, R. B.. **Contribuições para estudo do estágio de fluência terciária em solos**. PhD thesis, COPPE/UFRJ, Rio de Janeiro, 2000.

HAUPT, P.. **Continuum Mechanics and Theory of Materials**. Advanced Texts in Physics. Springer Berlin Heidelberg, 2000.

HICKMAN, R.; GUTIERREZ, M.; DE GENNARO, V. ; DELAGE, P.. **A model for pore-fluid-sensitive rock behavior using a weathering state parameter**. International journal for numerical and analytical methods in geomechanics, 32(16):1927–1953, 2008.

HICKMAN, R. J.; GUTIERREZ, M. S.. **Formulation of a three-dimensional rate-dependent constitutive model for chalk and porous rocks**. International Journal for Numerical and Analytical Methods in Geomechanics, 31(4):583–605, 2007.

HILL, R.. **Some basic principles in the mechanics of solids without a natural time**. Journal of the Mechanics and Physics of Solids, 7(3):209–225, 1959.

HINCHBERGER, S. D.; ROWE, R. K.. **Evaluation of the predictive ability of two elastic-viscoplastic constitutive models**. Canadian Geotechnical Journal, 42(6):1675–1694, 2005.

HOGER, A.. **The stress conjugate to logarithmic strain**. International Journal of Solids and Structures, 23(12):1645–1656, 1987.

HOULSBY, G.; PUZRIN, A.. **A thermomechanical framework for constitutive models for rate-independent dissipative materials**. International journal of Plasticity, 16(9):1017–1047, 2000a.

HOULSBY, G. T.; PUZRIN, A. M.. **An approach to plasticity based on generalised thermodynamics**, pages 319–331. Springer Berlin Heidelberg, Berlin, Heidelberg, 2000b.

JOHNSON, G. C.; BAMMANN, D. J.. **A discussion of stress rates in finite deformation problems**. International Journal of Solids and Structures, 20(8):725–737, 1984.

KAHN, J. S.. **The analysis and distribution of the properties of packing in sand-size sediments: 1. on the measurement of packing in sandstones**. The Journal of Geology, 64(4):385–395, 1956.

KATONA, M. G.. **Evaluation of viscoplastic cap model**. Journal of Geotechnical Engineering, 110(8):1106–1125, 1984.

KIM, M. K.; LADE, P. V.. **Single hardening constitutive model for frictional materials: I. plastic potential function**. Computers and Geotechnics, 5(4):307–324, 1988.

KOJIC, M.; BATHE, K.-J.. **Inelastic analysis of solids and structures**, volume 2. Springer, 2005.

KOLIJI, A.; VULLIET, L. ; LALOUI, L.. **New basis for the constitutive modelling of aggregated soils**. Acta Geotechnica, 3(1):61, 2008.

KULHAWY, F. H.; MAYNE, P. W.. **Manual on estimating soil properties for foundation design**. Technical report, Electric Power Research Inst., Palo Alto, CA (USA); Cornell Univ., Ithaca . . . , 1990.

KUTTER, B.; SATHIALINGAM, N.. **Elastic-viscoplastic modelling of the rate-dependent behaviour of clays**. Géotechnique, 42(3):427–441, 1992.

LACERDA, W.; COSTA FILHO, L. M.; COUTINHO, R. Q. ; DUARTE, E. R.. **Consolidation characteristics of Rio de Janeiro soft clays**. In **Proc. Cong. on Geotechnical Aspects of Soft Clays**, pages 231–244, Bangkok, 1977.

LACERDA, W. A.; HOUSTON, W. N.. **Stress relaxation in soils**. In **Proceedings of the Eighth International Conference on Soil Mechanics and Foundations Engineering**, pages 221–227. Moscow, Vol. 1/34, 1973.

LADE, P.; KIM, M.. **Single hardening constitutive model for frictional materials ii. yield critirion and plastic work contours**. Computers and geotechnics, 6(1):13–29, 1988.

LADE, P. V.. **Single-hardening model with application to nc clay**. Journal of geotechnical engineering, 116(3):394–414, 1990.

LAGIOIA, R.; NOVA, R.. **An experimental and theoretical study of the behaviour of a calcarenite in triaxial compression**. Géotechnique, 45(4):633–648, 1995.

LAGIOIA, R.; PUZRIN, A. ; POTTS, D.. **A new versatile expression for yield and plastic potential surfaces**. Computers and Geotechnics, 19(3):171–191, 1996.

LEE, E.; LIU, D.. **Finite-strain elastic—plastic theory with application to plane-wave analysis**. Journal of applied physics, 38(1):19–27, 1967.

LEE, E. H.. **Elastic-Plastic Deformation at Finite Strains**. Journal of Applied Mechanics, 36(1):1–6, 03 1969.

LEONARDS, G. A.; GIRAULT, P.. **A study of the one-dimensional consolidation test**. In **Proceedings of the Fifth International Conference on Soil Mechanics and Foundations Engineering**, pages 213–218. Paris, 1961.

LEONI, M.; KARSTUNEN, M. ; VERMEER, P.. **Anisotropic creep model for soft soils**. Géotechnique, 58(3):215–226, 2008.

LEROUEIL, S.; KABBAJ, M.; TAVENAS, F. ; BOUCHARD, R.. **Stress–strain–strain rate relation for the compressibility of sensitive natural clays**. Géotechnique, 35(2):159–180, 1985.

LEROUEIL, S.; VAUGHAN, P.. **The general and congruent effects of structure in natural soils and weak rocks**. Géotechnique, 40(3):467–488, 1990.

LIANG, R. Y.; MA, F.. **A unified elasto-viscoplasticity model for clays, part i: Theory**. Computers and Geotechnics, 13(2):71–87, 1992.

LIMA, G. D. P.. **Estudo de uma teoria não-linear para o adensamento unidimensional**. Master's thesis, COPPE/UFRJ, Rio de Janeiro, 1993.

LUBARDA, V.. **Elastoplasticity Theory**. Mechanical and Aerospace Engineering Series. CRC Press, 2001.

LUBLINER, J.. **Plasticity Theory**. Dover books on engineering. Dover Publications, 2008.

MCMEEKING, R.; RICE, J.. **Finite-element formulations for problems of large elastic-plastic deformation**. International Journal of Solids and Structures, 11:601–616, 1975.

NAKAI, T.; HINOKIO, M.. **A simple elastoplastic model for normally and over consolidated soils with unified material parameters**. Soils and foundations, 44(2):53–70, 2004.

NAVARRO, V.; ALONSO, J.; CALVO, B. ; SÁNCHEZ, J.. **A constitutive model for porous rock including effects of bond strength degradation and partial saturation**. International Journal of Rock Mechanics and Mining Sciences, 47(8):1330–1338, 2010.

NAYLOR, D. J.; PANDE, G. N.. **Finite elements in geotechnical engineering**. Pineridge press, 1981.

NEMAT-NASSER, S.. **Plasticity: a treatise on finite deformation of heterogeneous inelastic materials**. Dept. of Mechanical and Aerospace Engineering, University of California, San Diego, 2003.

NOVA, R.. **Modelling weathering effects on the mechanical behaviour of granite**. In **Constitutive modelling of granular materials**, pages 397–411. Springer, 2000.

NOVA, R.. **A simple elastoplastic model for soils and soft rocks**. In **Soil Constitutive Models: Evaluation, Selection, and Calibration**, pages 380–399. 2005.

NOVA, R.. **Soil mechanics**. Wiley Online Library, 2010.

NOVA, R.; CASTELLANZA, R. ; TAMAGNINI, C.. **A constitutive model for bonded geomaterials subject to mechanical and/or chemical degradation**. International Journal for Numerical and Analytical Methods in Geomechanics, 27(9):705–732, 2003.

NOVA, R.; WOOD, D. M.. **An experimental programme to define the yield function for sand**. Soils and Foundations, 18(4):77–86, 1978.

NOVA, R.; WOOD, D. M.. **A constitutive model for sand in triaxial compression**. International Journal for Numerical and Analytical Methods in Geomechanics, 3(3):255–278, 1979.

ORTIZ, M.; POPOV, E. P.. **Accuracy and stability of integration algorithms for elastoplastic constitutive relations**. International journal for numerical methods in engineering, 21(9):1561–1576, 1985.

ORTIZ, M.; SIMO, J.. **An analysis of a new class of integration algorithms for elastoplastic constitutive relations**. International Journal for Numerical Methods in Engineering, 23(3):353–366, 1986.

OWEN, D.; HINTON, E.. **Finite elements in plasticity**. Pineridge press, 1980.

PASTOR, M.; STICKLE, M. M.; DUTTO, P.; MIRA, P.; MERODO, J. F.; BLANC, T.; SANCHO, S. ; BENÍTEZ, A.. **A viscoplastic approach to the behaviour of fluidized geomaterials with application to fast landslides**. Continuum Mechanics and Thermodynamics, 27(1-2):21–47, 2015.

PERIĆ, D.. **On consistent stress rates in solid mechanics: computational implications**. International journal for numerical methods in engineering, 33(4):799–817, 1992.

PERIĆ, D.. **On a class of constitutive equations in viscoplasticity: formulation and computational issues**. International journal for numerical methods in engineering, 36(8):1365–1393, 1993.

PERZYNA, P.. **The constitutive equations for rate sensitive plastic materials**. Quarterly of applied mathematics, 20(4):321–332, 1963.

PERZYNA, P.. **Fundamental problems in viscoplasticity**. In **Advances in applied mechanics**, volume 9, pages 243–377. Elsevier, 1966.

PIPKIN, A. C.. **Large deformations with small strains**. In **Lectures on Viscoelasticity Theory**, pages 114–130. Springer US, New York, NY, 1972.

PLAXIS. **Material models manual**, 2019.

POTTS, D. M.; ZDRAVKOVIC, L.. **Finite element analysis in geotechnical engineering: Theory**. Thomas Telford Publishing, 1999.

PRAGER, W.. **Introduction to Mechanics of Continua**. Dover Publications, 2004.

REINHARDT, W.; DUBEY, R.. **Coordinate-independent representation of spins in continuum mechanics**. Journal of elasticity, 42(2):133–144, 1996.

RIOS, S.; CIANTIA, M.; GONZALEZ, N.; ARROYO, M. ; DA FONSECA, A. V.. **Simplifying calibration of bonded elasto-plastic models**. Computers and Geotechnics, 73:100–108, 2016.

ROWE, R. K.; HINCHBERGER, S. D.. **The significance of rate effects in modelling the sackville test embankment**. Canadian Geotechnical Journal, 35(3):500–516, 1998.

SCHOFIELD, A.; WROTH, P.. **Critical state soil mechanics**, volume 310. McGraw-Hill London, 1968.

SIMO, J. C.; HUGHES, T. J. R.. **Computational inelasticity**. Springer-Verlag, 1998.

SLOAN, S. W.. **Substepping schemes for the numerical integration of elastoplastic stress–strain relations**. International journal for numerical methods in engineering, 24(5):893–911, 1987.

SLOAN, S. W.; ABBO, A. J. ; SHENG, D.. **Refined explicit integration of elastoplastic models with automatic error control**. Engineering Computations, 18(1/2):121–194, 2001.

SUEBSUK, J.; HORPIBULSUK, S. ; LIU, M. D.. **Modified structured cam clay: A generalised critical state model for destructured, naturally structured and artificially structured clays**. Computers and Geotechnics, 37(7-8):956–968, 2010.

TAMAGNINI, C.; CASTELLANZA, R. ; NOVA, R.. **A generalized backward euler algorithm for the numerical integration of an isotropic hardening elastoplastic model for mechanical and chemical degradation of bonded geomaterials**. International Journal for Numerical and Analytical Methods in Geomechanics, 26(10):963–1004, 2002a.

TAMAGNINI, C.; CASTELLANZA, R. ; NOVA, R.. **Implicit integration of constitutive equations in computational plasticity**. Revue française de génie civil, 6(6):1051–1067, 2002b.

TERZAGHI, K.. **Theoretical Soil Mechanics**. John Wiley & Sons, Inc., 1943.

TRUESDELL, C.. **The Elements of Continuum Mechanics**. Springer-Verlag, New York, 1966.

TRUESDELL, C.; NOLL, W.. **The Non-Linear Field Theories of Mechanics, 3rd ed**. Springer, Berlin, Heidelberg, 2004.

VAN EEKELEN, H.. **Isotropic yield surfaces in three dimensions for use in soil mechanics**. International Journal for Numerical and Analytical Methods in Geomechanics, 4(1):89–101, 1980.

VIEIRA, L. O. M.. **Contribuição ao estudo do adensamento secundário**. Master's thesis, COPPE/UFRJ, Rio de Janeiro, 1988.

WANG, C.-C.; TRUESDELL, C.. **Introduction to Rational Elasticity**. Noordhoff International Publishing, Leyden, The Netherlands, 1973.

WANG, W.; SLUYS, L. ; DE BORST, R.. **Viscoplasticity for instabilities due to strain softening and strain-rate softening**. International Journal for Numerical Methods in Engineering, 40(20):3839–3864, 1997.

WEBER, G.; ANAND, L.. **Finite deformation constitutive equations and a time integration procedure for isotropic, hyperelastic-viscoplastic solids**. Computer Methods in Applied Mechanics and Engineering, 79(2):173 – 202, 1990.

WOOD, D. M.. **Soil behaviour and critical state soil mechanics**. Cambridge university press, 1990.

YIN, J.-H.; GRAHAM, J.. **Elastic viscoplastic modelling of the time-dependent stress-strain behaviour of soils**. Canadian Geotechnical Journal, 36(4):736–745, 1999.

YIN, Z.-Y.; KARSTUNEN, M. ; HICHER, P.-Y.. **Evaluation of the influence of elasto-viscoplastic scaling functions on modelling time-dependent behaviour of natural clays**. Soils and Foundations, 50(2):203–214, 2010.

YU, H.-S.. **Casm: A unified state parameter model for clay and sand**. International journal for numerical and analytical methods in geomechanics, 22(8):621–653, 1998.

YU, H. S.; TAN, S. M. ; SCHNAID, F.. **A critical state framework for modelling bonded geomaterials**. Geomechanics and Geoengineering, 2(1):61–74, 2007.

ZIEGLER, H.; WEHRLI, C.. **The derivation of constitutive relations from the free energy and the dissipation function**. volume 25 of **Advances in Applied Mechanics**, pages 183 – 238. Elsevier, 1987.

ZIENKIEWICZ, O.; CORMEAU, I.. **Visco-plasticity—plasticity and creep in elastic solids—a unified numerical solution approach**. International Journal for Numerical Methods in Engineering, 8(4):821–845, 1974.